

Winter 2012

# Nonideality in high concentration solutions

Ronald Toth

*University of New Hampshire, Durham*

Follow this and additional works at: <https://scholars.unh.edu/dissertation>

---

## Recommended Citation

Toth, Ronald, "Nonideality in high concentration solutions" (2012). *Doctoral Dissertations*. 705.  
<https://scholars.unh.edu/dissertation/705>

This Dissertation is brought to you for free and open access by the Student Scholarship at University of New Hampshire Scholars' Repository. It has been accepted for inclusion in Doctoral Dissertations by an authorized administrator of University of New Hampshire Scholars' Repository. For more information, please contact [nicole.hentz@unh.edu](mailto:nicole.hentz@unh.edu).

**NONIDEALITY IN HIGH CONCENTRATION SOLUTIONS**

**BY**

**RONALD TOTH**

**BS Biotechnology, Rutgers University, 2007**

**BS Biomathematics, Rutgers University, 2007**

**DISSERTATION**

**Submitted to the University of New Hampshire**

**in Partial Fulfillment of**

**the Requirements for the Degree of**

**Doctor of Philosophy**

**in**

**Biochemistry**

**December, 2012**

UMI Number: 3537827

All rights reserved

INFORMATION TO ALL USERS

The quality of this reproduction is dependent upon the quality of the copy submitted.

In the unlikely event that the author did not send a complete manuscript and there are missing pages, these will be noted. Also, if material had to be removed, a note will indicate the deletion.



UMI 3537827

Published by ProQuest LLC 2013. Copyright in the Dissertation held by the Author.

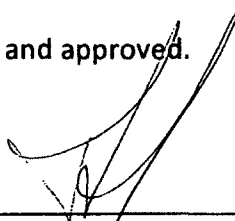
Microform Edition © ProQuest LLC.

All rights reserved. This work is protected against unauthorized copying under Title 17, United States Code.



ProQuest LLC  
789 East Eisenhower Parkway  
P.O. Box 1346  
Ann Arbor, MI 48106-1346

This dissertation has been examined and approved.



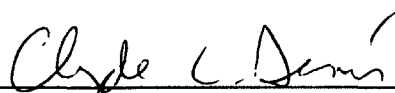
---

Dissertation Director, Thomas Laue, Professor  
(Biochemistry)



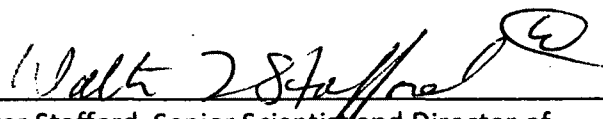
---

Rick Cote, Professor (Biochemistry)



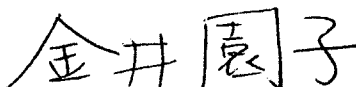
---

Clyde Denis, Professor (Biochemistry)



---

Walter Stafford, Senior Scientist and Director of  
Computer Sciences, Boston Biomedical Research  
Institute



---

Sonoko Kanai, Senior Scientist, Hoffmann-La Roche

---

Date

## ACKNOWLEDGMENTS

This project would not have been possible without the support of many people.

Many Thanks to my advisor, Dr. Thomas Laue, who read countless drafts and offered guidance. Thank you also to my committee members, Dr. Rick Cote, Dr. Clyde Denis, Dr. Walter Stafford, and Dr. Sonoko Kanai. Thanks to the late Susan Chase for training and guidance. Countless thanks to Susan Lucius for support and lab mother duties. Thanks to Dr. Dana Filoti for assisting with numerous experiments and for performing several towards the end of the project. Thanks to the University of New Hampshire Graduate School for two years of graduate assistantship awards. Thanks to Hoffman-La Roche and the Biomolecular Interaction Technologies Center for funding years of support on a research assistantship.

## TABLE OF CONTENTS

ACKNOWLEDGEMENTS .....	iii
LIST OF TABLES .....	vii
LIST OF FIGURES .....	viii
ABSTRACT .....	xiii
<b><u>CHAPTER</u></b> .....	<b><u>PAGE</u></b>
INTRODUCTION .....	1
Effective Hard Particle Model .....	2
Proximity Energy Framework.....	4
The Fluorescence Detection System .....	7
Description of Background Molecules.....	8
Analytical Ultracentrifugation .....	12
Calculating Expected Effects of Excluded Volume and Charge.....	18
Experimental Hypotheses .....	20
I. AU-FDS SEDIMENTATION EQUILIBRIUM OF BACKGROUND MOLECULES AND OF GFPIN HIGH CONCENTRATIONS OF BACKGROUNDS.....	21
Materials and Methods .....	21
Results.....	24
II. SEDIMENTATION VELOCITY OF GFP IN HIGH CONCENTRATIONS OF BACKGROUND MOLECULES.....	32
Materials and Methods .....	32

Results.....	33
III. USE OF EXCIPIENTS TO IDENTIFY THE CAUSE OF THE FASTER GFP FORMS .....	40
Materials and Methods .....	40
Results.....	40
IV. SEDIMENTATION VELOCITY OF GFP AND ANTI-GFP ANTIBODY IN HIGH CONCENTRATIONS OF BACKGROUND MOLECULES .....	45
Materials and Methods .....	45
Results.....	45
V. SEDIMENTATION VELOCITY OF GFP AND LABELED SERUM COMPONENTS IN SERUM .....	53
Materials and Methods .....	53
Results.....	54
VI. SEDIMENTATION OF LABELED MAB 1, MAB 2, and MAB 3 IN HIGH CONCENTRATIONS OF THEMSELVES.....	70
Materials and Methods .....	70
Results.....	73
VII. DISCUSSION.....	102
Hypothesis I: The FDS Will Enable the Tracking of a Single Component in a Complex Mixture .....	102
Hypothesis II: The Nonideality of the Tracer Will Differ From the Nonideality of the Background .....	103
Hypothesis III: Sedimentation Velocity is as Effective as Sedimentation Equilibrium in the Analysis of Complex Solutions.....	104
Hypothesis IV: The Proximity Energy Framework, When Applied to a New System Involving the Molecules mAb 1, mAb 2, and mAb 3, Can Adequately Account for Experimental Data .....	105

REFERENCES .....	108
APPENDIX A. DERIVATION OF $M/M_{APP}$ .....	114
APPENDIX B. SEDIMENTATION VELOCITY OF GFP IN HIGH CONCENTRATIONS OF BACKGROUND MOLECULES .....	118
APPENDIX C. SEDIMENTATION VELOCITY OF GFP AND ANTI-GFP IN HIGH CONCENTRATIONS OF BACKGROUND MOLECULES .....	125
APPENDIX D. SEDIMENTATION VELOCITY OF FIFTY PERCENT SERUM.....	132



## LIST OF TABLES

<u>TABLE</u>	<u>PAGE</u>
Table 1. Proximity energies between molecules in solution.....	5
Table 2. Charges of mAb 1, 2, and 3.....	75

## LIST OF FIGURES

<u>FIGURE</u>	<u>PAGE</u>
Figure 1. Electrostatic surface potential map of Soybean trypsin inhibitor.....	9
Figure 2. Electrostatic surface potential map of Hen egg white lysozyme.....	10
Figure 3. Electrostatic surface potential map of green fluorescent protein.....	11
Figure 4. 4 $\mu$ M GFP in PBS. ....	12
Figure 5. Example $M/M_{app}$ plots for a repulsively nonideal, attractively nonideal, and ideal molecule.....	16
Figure 6. Calculated values of $M/M_{app}$ for dextran, soybean trypsin inhibitor, and hen egg-white lysozyme.....	19
Figure 7. Calculated $M/M_{app}$ for GFP in dextran, soybean trypsin inhibitor, and hen egg-white lysozyme.....	19
Figure 8. Activity graph for dextran. ....	25
Figure 9. Activity graph for dextran and for GFP in dextran. ....	27
Figure 10. Activity graph for STI and for GFP in STI. ....	29
Figure 11. Activity graph for HEL and for GFP in HEL.....	31
Figure 12. 40 nM GFP in 20 g/L dextran.....	35
Figure 13. 40 nM GFP in 20 g/L HEL. ....	37
Figure 14. 40 nM GFP in 20 g/L STI. ....	37
Figure 15. Amount of faster material present in a solution of GFP and dextran upon addition of excipients.....	41
Figure 16. Amount of faster material present with and without addition of 2 M NaCl.....	42

Figure 17. 40 nM GFP, 40 nM anti-GFP in PBS.....	46
Figure 18. 40 nM GFP, 40 nM anti-GFP in HEL. ....	47
Figure 19. 40 nM GFP, 40 nM anti-GFP in Dextran.....	49
Figure 20. 40 nM GFP, 40 nM anti-GFP in STI.....	50
Figure 21. 40 nM GFP, 40 nM anti-GFP in 20 g/L HEL and 2 M NaCl. ....	52
Figure 22. 40 nM Alexa-HSA in PBS.....	55
Figure 23. 40 nM Alexa-IgG in PBS.....	55
Figure 24. Autofluorescence of serum.....	56
Figure 25. 40 nM Alexa-HSA in 25% serum. ....	57
Figure 26. 40 nM Alexa-IgG in 25% serum. ....	58
Figure 27. 40 nM GFP in 25% serum. ....	58
Figure 28. 40 nM Alexa-HSA in 50% serum. ....	60
Figure 29. 40 nM Alexa-IgG in 50% serum. ....	61
Figure 30. 40 nM GFP in 50% serum. ....	61
Figure 31. 40 nM Alexa-HSA in 75% serum. ....	63
Figure 32. 40 nM Alexa-IgG in 75% serum. ....	63
Figure 33. 40 nM GFP in 75% serum. ....	64
Figure 34 40 nM Alexa-HSA in 100% serum. ....	65
Figure 35. 40 nM Alexa-IgG in 100% serum. ....	65
Figure 36. 40 nM GFP in 100% serum. ....	66
Figure 37. Results of sedimentation velocity experiments of labeled IgG and HSA in serum.....	67
Figure 38. 40 nM GFP in serum.....	68

Figure 39. 40 nM GFP in 100% serum raw data.....	69
Figure 40. Densities of mAb 1, 2, and 3 as a function of concentration. ....	74
Figure 41. Viscosities of mAb 1, 2 and 3 as a function of concentration. ....	74
Figure 42. 120 nM Alexa-mAb 1 in 100 mM NaCl, 10 mM MES. ....	76
Figure 43. 120 nM Alexa- mAb 1 in 0.5 g/L mAb 1. ....	76
Figure 44. 120 nM Alexa- mAb 1 in 5 g/L mAb 1. ....	77
Figure 45. 120 nM Alexa- mAb 1 in 20 g/L mAb 1. ....	77
Figure 46. 120 nM Alexa- mAb 1 in 35 g/L mAb 1. ....	78
Figure 47. 120 nM Alexa- mAb 1 in 72 g/L mAb 1. ....	78
Figure 48. 120 nM Alexa-mAb1 in mAb 1.....	79
Figure 49. Results of sedimentation velocity experiments of labeled mAb 1.....	79
Figure 50. Examples of the raw data from a sedimentation experiment of mAb 1. ...	80
Figure 51. 120 nM Alexa-mAb 2 in 100 mM NaCl, 10 mM MES. ....	81
Figure 52. 120 nM Alexa-mAb 2 in 0.5 g/L mAb 2. ....	82
Figure 53. 120 nM Alexa-mAb 2 in 5 g/L mAb 2. ....	82
Figure 54. 120 nM Alexa-mAb 2 in 25 g/L mAb 2. ....	83
Figure 55. 120 nM Alexa-mAb 2 in 60 g/L mAb 2. ....	84
Figure 56. 120 nM Alexa-mAb 2 in 80 g/L mAb 2. ....	85
Figure 57. 120 nM Alexa-mAb2 in mAb 2.....	85
Figure 58. Results of sedimentation velocity experiments of labeled mAb 2.....	86
Figure 59. 120 nM Alexa-MAb 3 in 100 mM NaCl, 10 mM MES.....	87
Figure 60. 120 nM Alexa-mAb 3 in 0.5 g/L mAb 3. ....	87

Figure 61. 120 nM Alexa-mAb 3 in 6 g/L mAb 3. ....	88
Figure 62. 120 nM Alexa-mAb 3 in 30 g/L mAb 3. ....	88
Figure 63. 120 nM Alexa-mAb 3 in 60 g/L mAb 3. ....	89
Figure 64. 120 nM Alexa-mAb 3 in in 100 g/L mAb 3.....	90
Figure 65. 120 nM Alexa-mAb3 in mAb 3.....	91
Figure 66. Results of sedimentation velocity experiments of labeled mAb 3.....	91
Figure 67. M/M(app) of labeled mAbs in high concentrations of themselves.....	92
Figure 68. Nature of mAb 1, 2, and 3 self-association. ....	93
Figure 69. M/M(app) of labeled mAbs in high concentrations of themselves in low salt (10 mM). ....	94
Figure 70. Nature of mAb 1, 2, and 3 self-association in low salt (10 mM). ....	95
Figure 71. 120 nM Alexa-mAb 1 in 25% serum.....	97
Figure 72. 120 nM Alexa-mAb 1 in 50% serum.....	97
Figure 73. 120 nM Alexa-mAb 1 in 100% serum.....	98
Figure 74. 120 nM Alexa-mAb 2 in 25% serum.....	98
Figure 75. 120 nM Alexa-mAb 2 in 50% serum.....	99
Figure 76. 120 nM Alexa-mAb 2 in 100% serum.....	99
Figure 77. 120 nM Alexa-mAb 3 in 25% serum.....	100
Figure 78. 120 nM Alexa-mAb 3 in 50% serum.....	100
Figure 79. 120 nM Alexa-mAb 3 in 100% serum.....	101
Figure 80. 40 nM GFP in 0.1 g/L dextran. ....	118
Figure 81. 40 nM GFP in 1 g/L dextran.....	119
Figure 82. 40 nM GFP in 5 g/L dextran.....	119

Figure 83. 40 nM GFP in 20 g/L dextran.....	120
Figure 84. 40 nM GFP in 0.1 g/L HEL.....	120
Figure 85. 40 nM GFP in 1 g/L HEL.....	121
Figure 86. 40 nM GFP in 5 g/L HEL.....	121
Figure 87. 40 nM GFP in 20 g/L HEL.....	122
Figure 88. 40 nM GFP in 0.1 g/L STI.....	122
Figure 89. 40 nM GFP in 1 g/L STI.....	123
Figure 90. 40 nM GFP in 5 g/L STI.....	123
Figure 91. 40 nM GFP in 5 g/L STI.....	124
Figure 92. 40 nM GFP, 40 nM anti-GFP in 0.1 g/L HEL.....	125
Figure 93. 40 nM GFP, 40 nM anti-GFP in 1 g/L HEL.....	126
Figure 94. 40 nM GFP, 40 nM anti-GFP in 5 g/L HEL.....	126
Figure 95. 40 nM GFP, 40 nM anti-GFP in 20 g/L HEL.....	127
Figure 96. 40 nM GFP, 40 nM anti-GFP in 0.1 g/L dextran.....	127
Figure 97. 40 nM GFP, 40 nM anti-GFP in 1 g/L dextran.....	128
Figure 98. 40 nM GFP, 40 nM anti-GFP in 5 g/L dextran.....	128
Figure 99. 40 nM GFP, 40 nM anti-GFP in 20 g/L dextran.....	129
Figure 100. 40 nM GFP, 40 nM anti-GFP in 0.1 g/L STI.....	129
Figure 101. 40 nM GFP, 40 nM anti-GFP in 1 g/L STI.....	130
Figure 102. 40 nM GFP, 40 nM anti-GFP in 5 g/L STI.....	130
Figure 103. 40 nM GFP, 40 nM anti-GFP in 20 g/L STI.....	131
Figure 104. Autofluorescence of 50% serum.....	132

## GLOSSARY OF TERMS

GFP – green fluorescent protein

HEL – hen egg white lysozyme

STI – soybean trypsin inhibitor

AU-FDS – analytical ultracentrifugation fluorescence detection system

PBS – phosphate buffered saline, comprising 137 mM NaCl, 2.7 mM KCl, 10 mM Na<sub>2</sub>HPO<sub>4</sub>•2H<sub>2</sub>O, 2 mM KH<sub>2</sub>PO<sub>4</sub>, pH 7.4.

GFP:anti-GFP – refers to the complex resulting from the binding of GFP to anti-GFP

J-O effect – Johnston-Ogston effect

mAb – monoclonal antibody

MES – 2-(N-morpholino)ethanesulfonic acid

MCE – membrane confined electrophoresis

SDS-PAGE – sodium dodecyl sulfate polyacrylamide gel electrophoresis

## ABSTRACT

### NONIDEALITY IN HIGH CONCENTRATION SOLUTIONS

By

Ronald Toth

University of New Hampshire, December, 2012

Our current understanding of molecular interactions, the kinetics, equilibria, and thermodynamics of biochemical reactions, is based mostly on research conducted in dilute solutions. Recent interest in the implications of true physiological concentrations has led to the development of new tools and techniques. *In vivo* biological systems differ so significantly from dilute solutions that a model is required to conceptualize them. The excluded volume theory is one such model. In this framework macromolecules are regarded as hard spherical volumes, holding only the property of size, and not those of shape or charge. Alternatively, the proximity energy framework considers molecules as having a complex web of various properties, including charge, that extend into the solution.

The experimental hypothesis tested in this dissertation was whether the proximity energy framework was sufficient to explain analytical ultracentrifugation data gathered in complex biological solutions. Additional hypotheses tested were as follows: The Fluorescence Detection System for the Analytical Ultracentrifuge will enable the tracking of a single component in a complex mixture; The nonideality of a molecule present in a trace amount in a crowded solution will differ from the nonideality of the background



solution; Sedimentation velocity can be used in place of sedimentation equilibrium and provide similar insights into interactions in complex solutions.

The proximity energy framework was found to account for analytical ultracentrifugation data gathered in both model solutions and biologically relevant solutions such as serum. Tracking a single component in a complex solution with the fluorescence detection system proved challenging and did not work in all cases. The nonideality of a molecule present in a trace amount in a crowded solution was found to differ significantly from the nonideality of the background solution. Finally, it was found that sedimentation velocity is best used in conjunction with sedimentation equilibrium, as, while there is some overlap, both methods provide unique information about complex solutions and molecular interactions therein.

## INTRODUCTION

Our current understanding of the kinetics, equilibria, and thermodynamics of molecular interactions is based mostly on research conducted in dilute solutions. This restriction is due in part to the scientific method's historical trend towards reductionism, and due in part to technological limitations caused by the lack of tools to look at complex concentrated systems. However, recent interest in the implications of true physiological concentrations on reaction rates and equilibria (Special Issue: EMBO Workshop, 2003) on the part of pharmaceutical corporations, coupled with the rise of the field of systems biology (Sauer, 2007), in which researchers consider entire biological systems, striving towards holism, has led to the development of new tools and techniques.

True *in vivo* conditions can differ widely from the dilute conditions usually used in biochemical research (Hall and Minton, 2003). In the blood stream macromolecular concentrations can reach in excess of 70 grams per liter (Adkins et. al., 2002). In the cytoplasm of a cell it can be even higher, around 300 grams per liter (van Beekvelt et. al., 2001). If a potential drug molecule is formulated and studied at a low concentration it is not always easy to predict how it will behave once injected into this volume-occupied environment.

Conversely, because a single injection of a drug is far more convenient and less costly than subjecting a patient to an IV drip for hours, it is often advantageous to formulate a

drug at hundreds of grams per liter and to allow it to become dilute upon injection into the bloodstream or, alternatively, dilute the drug in an IV bag prior to injection.

However, producing high concentration formulations of a drug is often problematic (Shire et. al., 2004) (Dani et. al., 2007). Will the molecule hold up to the shear forces when ejected from a syringe at such high concentrations (Martonen et. al., 2005)? Does it self-associate at higher concentrations (Vázquez-Rey and Lang, 2011)? If so, is the self-association reversible (Cromwell et. al., 2006)? Will any aggregates disassociate to monomer fast enough once injected or will residual aggregates generate an immune response (Rosenberg, 2006);(Purohit,2006)? Questions such as these make it vital to understand how molecules behave in high concentration solutions.

In order to interpret physical phenomena associated with high concentration solutions, a physical framework is required. Two useful models are outlined below.

### **Effective Hard Particle Model**

In biological media macromolecules can occupy up to twenty to thirty percent of the total volume of the solution and the solution is said to be “volume-occupied” or “crowded.” One of the more useful frameworks that has been developed to attempt to quantitatively describe such environments is the effective excluded volume theory (Minton, 1997).

The excluded volume theory defines any macromolecule in solution as a hard spherical volume (Ellis, 2001). The hard spherical volume conceptualization of macromolecules in a volume-occupied solution has several interesting implications. The

most apparent of these is that the volume accessible to a molecule in a crowded solution is less than the total volume of the solution (Minton, 2001). The reduced volume decreases the number of ways to add new molecules into the solution, resulting in lower entropy. Because the entropy term is subtracted in the free energy equation ( $\Delta G = \Delta H - T\Delta S$ ) the reduced entropy will tend to increase the reaction rates in a crowded solution due to a rise in the baseline Gibbs free energy of the solution (Minton, 2001). This effect has been shown to increase reaction rates in crowded solutions by a factor of two to three (Minton, 2011).

Yet another effect of the scarcity of free volume in crowded solutions is that crowding tends to favor the formation of complexes. Complex formation will be favored if the volume taken up by the complex is less than the sum of the volume taken up by the reacting molecules individually. In other words, the complex formation results in increased entropy due to the increased free volume. Thus, by forming complexes the system reaches a lower free energy state. This favoring of complexes helps to explain some phenomena, such as the formation of protein aggregates called inclusion bodies in cells (Cruts et. al., 2006) and the ability of some proteins to fold spontaneously in crowded solutions without molecular chaperones, even though they do not fold properly in dilute solutions (van der Berg et. al., 1999).

While the excluded volume theory has been very successful in some areas, such as explaining the aforementioned phenomena, it also has several problems. These problems stem from the fact that the excluded volume model takes into account the size and shape of molecules and approximates their electrostatic properties by

incorporating them into an “effective volume” fitting parameter (Minton, 2007). As a result of this approximation, any enthalpies of interaction between molecules are assumed to be identical. However, using the effective volume approximation disallows consideration of a molecule capable of interacting with multiple different types of molecules, where a separate effective volume parameter would be needed for each type of interaction. That is, the excluded volume model assumes identical between molecules, which is unlikely to be the case in a complex mixture of molecules.

While there have been other attempts to add electrostatic interactions to the excluded volume model, such as adding a “Donnan term” to the excluded volume equations to account for the charge of molecules (Tanford, 1961), the Donnan term correction considers steric effects first, and treats electrostatics secondarily.

### **Proximity Energy Framework**

In the proximity energy framework (Laue, 2012), electrostatics are a primary concern when considering molecular interactions in crowded solutions. Laue argues that when the average distance between molecules approaches the order of the diameter of the molecules themselves, it is the proximity energies that tend to dominate. There are eight forms of proximity energies (Table 1) between molecules, all described by the common equation  $U = \frac{X_1 X_2}{D r^n}$ , where  $X_1$  and  $X_2$  are the magnitude of the properties,  $D$  is the dielectric constant,  $r$  is the edge to edge distance between a pair of molecules, and  $n$  is the distance dependence. A problem enters in that this framework becomes hard to

apply when any molecule in the solution is capable of having any one of these interactions with any other molecule at any time. In the case of a mixture of molecules, the pairwise interaction equation becomes  $U = \sum \frac{X_i X_j}{D r_{ij}^n}$ , the pairwise interaction summed over all molecules and interactions in the solution. While there have been successful attempts to use this detailed approach (Wills and Winzor, 2001), the explicit solutions of this summation are too complex to apply to real systems. An attractive solution to this problem would be to restrict consideration of the proximity energies to a single species in the solution and analyze its overall interactions with other solution components.

Type	$X_1$	$X_2$	$n$	Dependence
Charge-charge	Q	Q	1	$\Gamma$
Charge-dipole	Q	$\mu$	2	$\Gamma, \Theta$
Dipole-dipole	$\mu$	$\mu$	3	$\Gamma, \Theta$
Charge-induced dipole	Q	$\alpha$	4	$\Theta$
H-bond	E	E	4	$\Theta$
Dipole-induced dipole	$\mu$	$\alpha$	5	$\Theta$
Dispersion	$\alpha$	$\alpha$	6	Not D
Van der Waals	-	-	12	Not D

Table 1. Proximity energies between molecules in solution. In the dependence column,  $\Gamma$  indicates that the strength of the interaction is dependent on the ionic strength of the solution,  $\Theta$  indicates that the strength of the interaction is dependent on the orientation of the interacting molecules, and "not D" indicates that the strength of the interaction is not dependent on the dielectric constant of the solution.

In a sedimentation equilibrium experiment of a single solute, the quantity  $1 + C \frac{\partial \ln \gamma}{\partial C}$  (where C is the molar concentration of the solute, and  $\gamma$  is the activity coefficient of the solute) is assessed by measuring the apparent molar mass of a molecule at several different concentrations (see analytical ultracentrifugation section below). The quantity  $\frac{\partial \ln \gamma}{\partial C}$  is a measure of the change in the activity coefficient of a solute with respect to concentration. This quantity being multiplied by the concentration of that solute ensures that  $1 + C \frac{\partial \ln \gamma}{\partial C}$  does not become significantly different from 1 unless the solute is present in sufficient concentration. That is, if the activity coefficient of a solute changes strongly with concentration, but is dilute, there will be no significant effect on  $1 + C \frac{\partial \ln \gamma}{\partial C}$ . Thus,  $1 + C \frac{\partial \ln \gamma}{\partial C}$  is simply a measure of how the activity coefficient of a solute changes with concentration, given that the solute is present in sufficient quantity. The activity coefficient of a molecule changes with concentration due to the proximity energies and the excluded volume effect discussed previously. The proximity energies are enthalpic, whereas excluded volume effects are entropic.

In the case of a multi-component solution,  $M_{app} = M / \left( 1 + C \frac{\partial \ln \gamma}{\partial C} \right)$  becomes  $M_{i,app} = M_i - \sum_j M_{j,app} C_j \frac{\partial \ln \gamma_i}{\partial C_j}$  (Rivas et. al., 1999). What this equation indicates is that, somewhat similarly to the case with a single solute, for any species j to have a significant impact on the apparent molecular weight of species i, both the change in activity coefficient of i with respect to concentration of j and the concentration of species j must be significantly different from zero.

## The Fluorescence Detection System

One experimental approach that abrogates much of this complexity is the Fluorescence Detection System (AU-FDS) by Aviv Biomedical. By constructing experiments in such a way that a molecule of interest is the only species that fluoresces, one is able to track a single species in a complex crowded solution for the entirety of a biophysical experiment. Also helpful is that if the fluorescent solute is present only in trace amounts, the quantity  $C_i \frac{\partial \ln \gamma_i}{\partial C_i}$ , where  $i$  is fluorescent solute, will not be significantly different from zero, allowing it to be omitted from

$M_{i,app} = M_i - \sum_j M_{j,app} C_j \frac{\partial \ln \gamma_i}{\partial C_j}$ , reducing to  $M_{i,app} = M_i - M_{i,app} C_j \frac{\partial \ln \gamma_i}{\partial C_j}$ . This allows

the quantity  $1 + \frac{M_{j,app}}{M_{i,app}} C_0 \frac{\partial \ln \gamma_i}{\partial C_j}$  to be assessed by measuring the apparent molar mass of the fluorescent solute at several concentrations of the non-fluorescent solute, similar to the case with a single solute.

The technique of using a fluorescent solute in trace quantity will be employed in some experiments presented in this study. The AU-FDS will be used to monitor the biophysical properties of a fluorescent tracer molecule, green fluorescent protein (GFP) that has been added at low concentration into a variety of volume-occupied solutions prior to analytical ultracentrifugation experiments. To construct these volume occupied solutions, three different molecules were used; hen egg white lysozyme (HEL) to serve as a model of a small cationic protein, soybean trypsin inhibitor (STI) to serve as a model of a small anionic protein, and dextran (DEX) to serve as a model of a small neutral molecule. The data from these experiments were analyzed to determine whether



enthalpic or entropic forces dominate the interactions. The proximity energy framework was then applied in an attempt to better understand the influence of the crowder (j) on the activity coefficient of GFP (i).

### **Description of Background Molecules**

#### **Dextran**

Dextran is a complex sugar, a highly branched glycan. The main backbone consists of  $\alpha$ -1,6 glycosidic bonds, while the branches emanate from  $\alpha$ -1,3 bonds (Rong, 2006). The main backbone chain is of various lengths. In this study, the dextran molecules used were between 9 kDa and 11 kDa. Dextran is used in the medical, veterinary, food science, and pharmaceutical industries for a wide variety of purposes, such as adjuvant, emulsifier, carrier, and stabilizer (Bhavani and Nisha, 2010). However, there has been very little work done on dextran's biophysical interactions with protein molecules, apart from one report indicating that solutions of only dextran may separate spontaneously into immiscible phases (Long et. al., 2005). Thus if two interacting proteins were to be added to this solution, the separate phases would tend to influence protein interactions based on the chemical potential of the two reactants in each phase, as well as that of the complex. The interaction between two proteins would be either favored or disfavored if both had a lower standard free energy state the same phase or each had lower standard free energy in a different phase, respectively. Apart from the difference in free energies in the case of immiscible phases, information on the interactions of

proteins with polysaccharides in general must be considered. As dextran does not carry a charge, the only modes of interaction available are nonspecific interactions that are either attractive, such as London dispersion forces, hydrogen bonding, or charge-induced dipole interactions, which would cause the formation of protein-dextran complexes, or repulsive, such as steric repulsion (Damodaran and Paraf, 1997).

The sedimentation coefficient,  $s(20,w)$ , of the dextran used in this study is 1.5 s.

### **Soybean Trypsin Inhibitor**

Trypsin inhibitors are proteins made by many plants as a defense mechanism against consumption by animals (Habib and Fazili, 2007). In soybeans, the protein is monomeric and consist of a single polypeptide chain of 181 residues, cross-linked by two disulfide bridges and containing several  $\beta$ -strands (Kim et. al., 1985)(Steiner, 1965)(Koide and Ikenaka, 1973). The molar mass of STI is 16960 Da. An electrostatic surface potential map of soybean trypsin inhibitor is presented in Figure 1. The charge on STI is -8.6 in 100 mM KCl, 10 mM TRIS pH 7.5, and the sedimentation coefficient  $s(20,w)$  in PBS is 2.1.



Figure 1. Electrostatic surface potential map of Soybean trypsin inhibitor. Regions of positive electrostatic potential are shown in blue, negative in red (Songa and Suth, 1998).

## Hen Egg White Lysozyme

Lysozyme is a protein made in many organisms to protect against bacterial infection by catalyzing the hydrolysis of the bacterial cell wall (Fleming, 1922). In chicken egg white the protein is monomeric and consists of a single polypeptide chain 129 residues long, cross-linked by four disulfide bridges and containing  $\alpha$ -helices and a small antiparallel beta sheet (Johnson and Phillips, 1965). The molar mass of HEL is 14313 Da. An electrostatic surface potential map of hen egg white lysozyme can be seen in Figure 2. The charge is 6.1 in 100 mM KCl, 10 mM TRIS pH 7.5, and the sedimentation coefficient  $s(20,w)$  in PBS is 1.8.

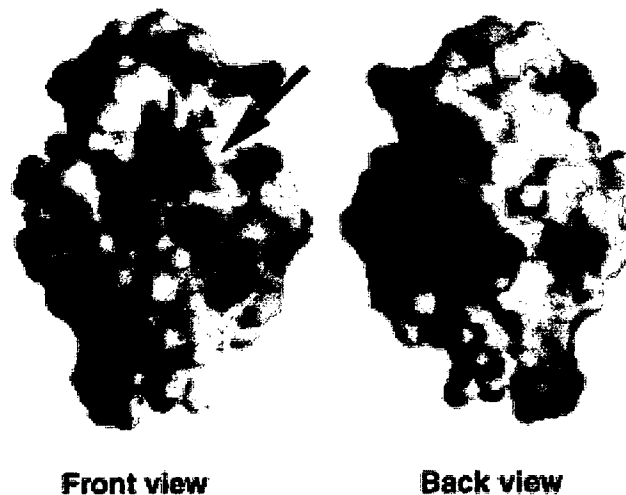


Figure 2. Electrostatic surface potential map of Hen egg white lysozyme. Regions of positive electrostatic potential are shown in blue, negative in red (Jain et. al., 2001).

## Green Fluorescent Protein

Green fluorescent protein (GFP) is made by many marine animals (Prendergast and Mann, 1978). It is a monomeric protein consisting of a single polypeptide chain of 238

residues, containing one  $\beta$ -sheet in a barrel conformation, and several  $\alpha$ -helices, two of which stabilize the chromophore at the center (Tsien, 1998)(Ormö et. al., 1996)(Yang et. al., 1996). The molar mass of GFP is 30838 Da. An electrostatic surface potential map of GFP can be seen in Figure 3. The GFP molecule seen in Figure 3 is different from the one used in this study, and it is likely that the red shifted GFP used here has a different electrostatic surface potential map. The charge on GFP is -6.7 in 100 mM KCl, 10 mM TRIS pH 7.5, and the sedimentation coefficient  $s(20,w)$  in PBS is 2.7.

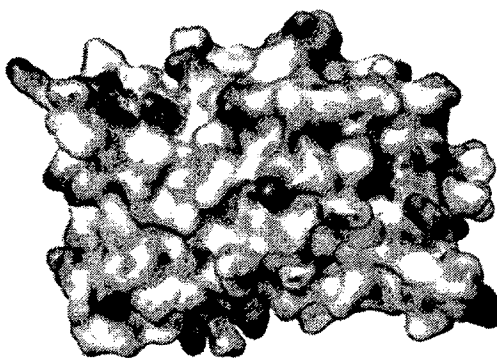


Figure 3. Electrostatic surface potential map of green fluorescent protein. Regions of positive electrostatic potential are shown in blue, negative in red (McNaughton et. al., 2009).

Sedimentation velocity (described below) was conducted on GFP at 4  $\mu$ M in PBS and fit to a single peak (Figure 4), demonstrating that the GFP used in these studies does not self-associate at concentrations up to 4  $\mu$ M.

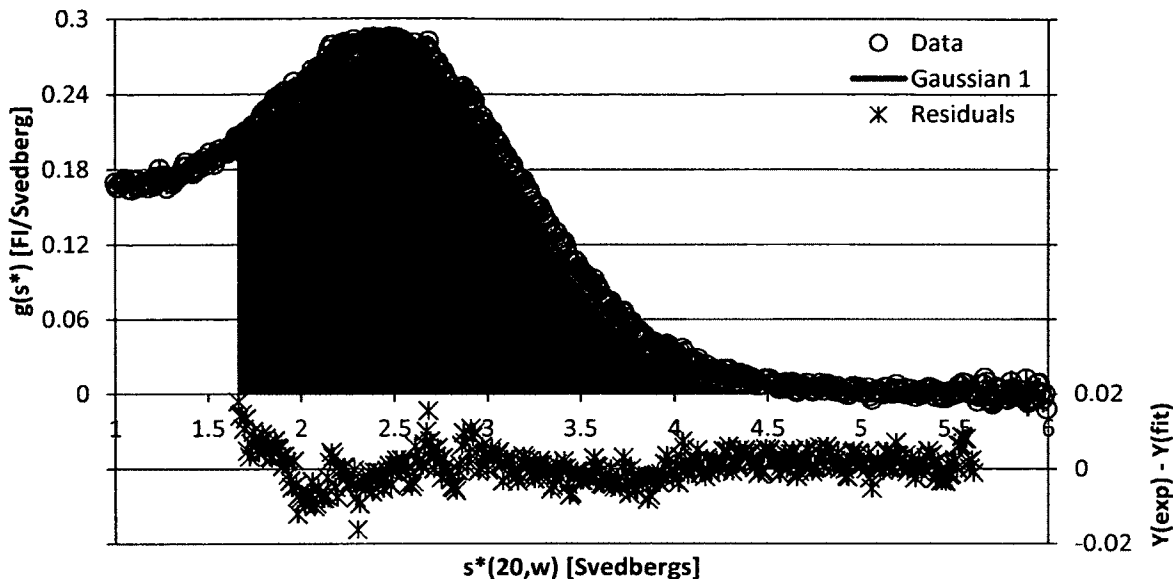


Figure 4. **4  $\mu\text{M}$  GFP in PBS.** A  $g(s)$  plot from a sedimentation velocity experiment. On the primary axis is plotted the experimental data (Data), and a putative plot for the Gaussian that represents the proposed fit to the data, with the area under the curve colored to indicate which portions of the total signal it can account for. Residuals are plotted on the secondary axis. Data was acquired with the fluorescence detection system.

### Analytical Ultracentrifugation

In sedimentation velocity experiments, the sedimentation and diffusion of a solute such as GFP can be analyzed by software such as DCDT+. The program takes in a set of sequential scans, divides them into two groups, those taken earlier in the run and those taken later. The program then subtracts the later group of scans from the earlier group (Stafford, 2003). This results in time derivative plots corrected for time-invariant noise, with the change in concentration with respect to time,  $\frac{\Delta c}{\Delta t}$ , on the y-axis and radial position on the x-axis. The plots are averaged, and the radial axis is then transformed to  $s^*$  by the relation  $s^* = \frac{1}{\omega^2 t} \ln\left(\frac{r}{r_m}\right)$ , where  $\omega$  is the angular velocity of the rotor,  $t$  is the sedimentation time, and  $r_m$  is the radial position of the meniscus. This transformation

changes the spatial reference frame to the sedimentation coefficient reference frame. The final step is to transform the y-axis such that the area under each peak becomes equal to its plateau concentration. These two transforms create the  $g(s^*)$  vs.  $s^*$  plot. In the case of an ideal molecule and solution, the concentration profile will be an error function, the derivative of which is a Gaussian distribution. Therefore, for a mixture of ideal solutes, the  $g(s^*)$  plot may be fit to a sum of Gaussian peaks, with each sedimenting species generating a single Gaussian peak resulting from a Faxén approximation (Schuck and Rossmanith, 2000) of the Lamm equation (Lamm, 1929). However, experimental data often does not resemble an ideal case, and unsymmetrical, non-Gaussian peaks result. For DCDT+ these cases are fit to the sum of Gaussians. However, the interpretation of the data loses quantitative meaning and must be viewed as qualitative. The residuals of the fit are a measure of how well the proposed fit accounts for the data.

Because the diffusion coefficient of a species,  $D$ , is related to the width of the Gaussian peak, the molar mass,  $M$ , can be determined using the quantity  $\frac{sRT}{D(1-\bar{v}\rho_0)}$ , where  $s$  is the  $s^*$  position of the peak (Philo, 2000). However, these approximations are only valid for dilute solutions of non-interacting components. Therefore, when applied to a concentrated solution of components capable of interacting, each Gaussian peak does not necessarily correspond to a sedimenting species.

The x-axis of the  $g(s^*)$  plot may be transformed from  $s$  to  $s_{20,w}$  using the equation  $S_{20,w} = s^* \frac{(1-\bar{v}\rho)_{20,w}\eta_{T,b}}{(1-\bar{v}\rho)_{T,b}\eta_{20,w}}$ , where  $T$  refers to the experimental temperature,  $b$  refers to the experimental buffer conditions, and  $20, w$  refers  $20^\circ$  C in water (Cole et. al., 2008).

This transform serves to shift the experimental data to where it would have been theoretically had the experiment been conducted in water at 20° C. In this way  $s$  values obtained in buffers with different densities and viscosities may be compared. This transformation was applied for all data presented in this thesis and when the term  $s$  is used it will be assumed to be  $s_{20, w}$ .

In a sedimentation equilibrium experiment, the solution is allowed to sediment until each molecule of the solute has reached equilibrium between the centrifugal force pushing it down the cell and the buoyancy force and gradient in chemical potential causing the solute to diffuse up the cell. A series of scans are taken to verify that the solution is at equilibrium, as shown by a time invariant concentration distribution, and a single scan is chosen for further analysis. The concentration profile from the selected scan is fit to an exponential function, the curvature of which can be described by the mathematical parameter  $\sigma$ , which is a Boltzmann term. The term  $\sigma$  is equal to  $\frac{M_b \omega^2}{RT}$ , where the numerator is the gravitational potential energy and the denominator is the average kinetic energy. For a single ideal solute,  $\sigma$  can be used to determine the apparent molar mass of the solute using the relation  $M_{app} = \frac{\sigma RT}{\omega^2(1-\bar{v}\rho)}$  (Cole, 2004). By measuring the apparent molar mass at several concentrations, a plot with concentration on the x axis and  $1 + C \frac{\partial \ln \gamma}{\partial C}$  on the y axis may be constructed using the relation  $M/M_{app} = 1 + C \frac{\partial \ln \gamma}{\partial C}$  (Tanford, 1961). A derivation of this relation can be found in Appendix A.

The value of  $M/M_{app}$  provides a measure of the solution nonideality. Nonideality reflects the energy needed to introduce a solute molecule into a solution that already contains solute molecules. If a new molecule were to be placed into a solution of molecules experiencing repulsive nonideality, the energy required for its insertion would be greater than if it were to be placed into an ideal dilute solution. Here an ideal solution is defined as having solutes that are points and have no radius, and the enthalpic interactions of the solute with itself and with the solvent are identical. That is to say, the  $\Delta H$  is identical for all solution components. The increased energy increment when placing new molecules into a repulsively nonideal solution would cause solutes in the solution to have an activity coefficient greater than one. In such a case the increase in the activity coefficient would be reflected in an increase in  $\frac{\partial \ln \gamma}{\partial c}$  and, consequently, an increase in  $1 + C \frac{\partial \ln \gamma}{\partial c}$ .

Similarly, in a solution whose solutes are experiencing attractive nonideality, less energy would be required to place a new molecule into the solution than in an ideal solution, causing a lower energy increment compared to adding the molecule into an ideal solution. A lower energy increment would result in a lower activity coefficient, and the activity coefficient would decrease with concentration, resulting in a decrease of  $1 + C \frac{\partial \ln \gamma}{\partial c}$  with concentration.

Finally, an ideal molecule would have no change in activity coefficient with concentration. The activity coefficient would be one, and therefore  $\ln \gamma$  would be 0 and  $M/M_{app}$  would remain constant and equal to one. In summary, what this all means is



that the apparent molecular weight of a molecule is inversely proportional to  $1 + C \frac{\partial \ln \gamma}{\partial C}$  and therefore related to the activity coefficient of the molecule as a function of concentration. Consequently, if the activity coefficient of a molecule increases with concentration, the apparent molecular weight of the molecule will decrease with concentration, and the  $M/M_{app}$  of the molecule will increase with concentration. Conversely, if the activity coefficient of a molecule decreases with concentration, the apparent molecular weight of the molecule will increase with concentration, and the  $M/M_{app}$  of the molecule will decrease with concentration. Examples of the relation between  $M/M_{app}$  and nonideality for an attractively nonideal, repulsively nonideal, and ideal molecule are shown in Figure 5.

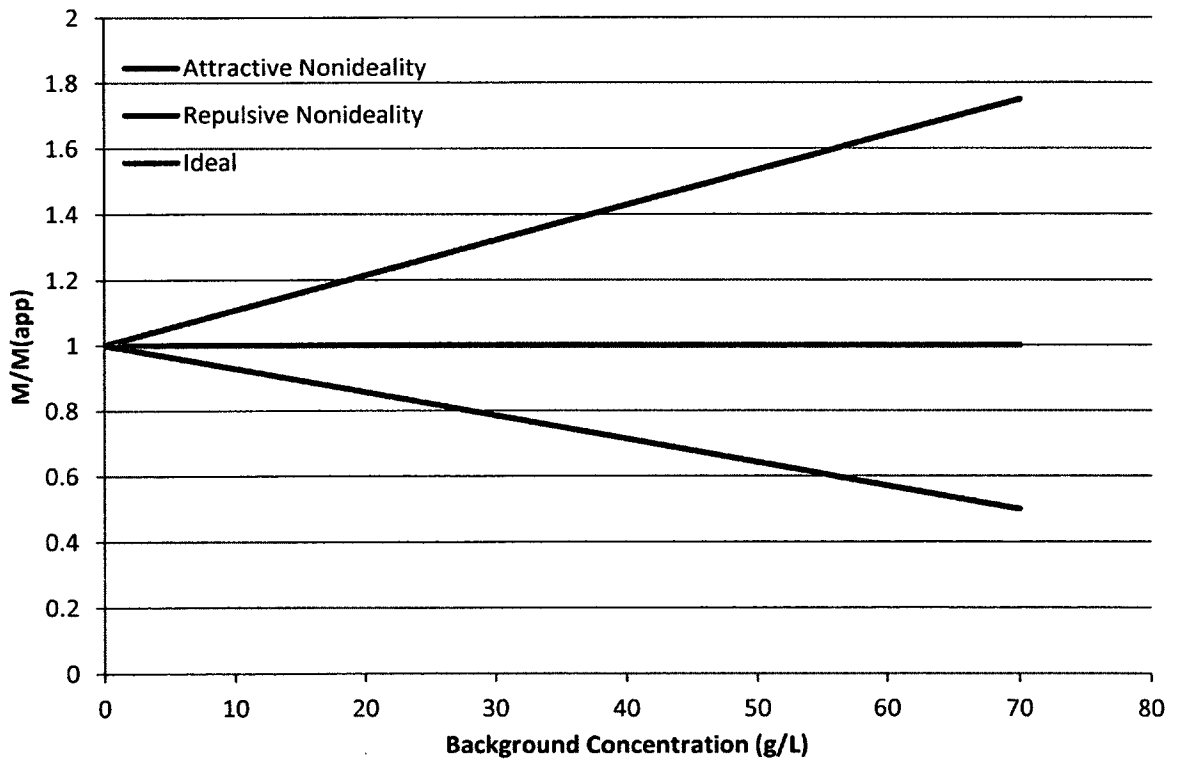


Figure 5. Example  $M/M_{app}$  plots for a repulsively nonideal, attractively nonideal, and ideal molecule. The slope of the lines is equal to  $2B_2M$ . In the case of attractive nonideality,  $2B_2M$  is greater than zero, and in the case of repulsive nonideality  $2B_2M$  is less than zero. In the ideal case  $2B_2M$  is equal to zero.

As discussed previously, in the case of a two component solution with component  $i$  being present in trace quantity  $1 + \frac{M_{j,app}}{M_{i,app}} C_j \frac{\partial \ln \gamma_i}{\partial C_j}$  is considered instead of  $1 + C \frac{\partial \ln \gamma}{\partial C}$  (Rivas et. al., 1999). However, all of the above conclusions regarding the relationship between  $M/M_{app}$  and activity coefficient still hold.

If the chemical activity ( $a$ ) is considered in place of the activity coefficient ( $\gamma$ ), and  $\frac{a}{C}$  is substituted for  $\gamma$  in these equations, in the case of a single solute this equation reduces to  $\frac{M_i}{M_{i,app}} = 1 + C_i \left( \frac{\partial \ln a_i}{\partial C_i} - \frac{\partial \ln C_i}{\partial C_i} \right)$ . This equation indicates that the apparent molecular weight of a molecule is related to the activity of that molecule as a function of concentration, in a manner similar to the relation between apparent molecular weight and the activity coefficient, albeit as a slightly weaker function. This means that if the activity of a molecule were to increase with concentration, its apparent molecular weight would decrease, and vice versa.

Similarly, in the case of a two component system with component  $i$  being present in trace quantities, upon substitution of  $\frac{a}{C}$  for  $\gamma$  this equation reduces to  $1 + \frac{M_{j,app}}{M_{i,app}} C_j \left( \frac{\partial \ln a_i}{\partial C_j} - \frac{\partial \ln C_i}{\partial C_j} \right)$ . Because in most experiments of this nature the concentration of  $i$  is a constant,  $\ln C_i$  may be viewed as a constant, and all of the above conclusions regarding the apparent molecular weight increasing with the activity coefficient of component  $i$  are also true of the activity of the molecule. This equivalence between activity and the activity coefficient means that for the purposes of this discussion, the terms chemical activity and activity coefficient will be used interchangeably.

### Calculating Expected Effects of Excluded Volume and Charge

As established previously,  $M/M_{app}$  is equal to  $1 + C \frac{\partial \ln \gamma}{\partial C}$ . This definition of  $M_{app}$  also requires  $M/M_{app}$  to be equal to  $1 + 2B_2MC$  (see Figure 5), where  $B_2$  is the second virial coefficient (Tanford, 1961). The second virial coefficient is a measure of the nonideality of the solution. Here the second virial coefficient is considered to be formed by two contributions, electrostatic (enthalpic) and excluded volume (entropic). It must be noted that for a solution containing a single macromolecule, both of these contributions will be unfavorable (i. e. the activity coefficient will be greater than one). For the electrostatic contribution, in a single macromolecule solution,  $B_2$  is  $\frac{Z^2 v_1}{4m_3 M_2^2}$ , where  $Z_2$  is the protonic charge of the solute,  $v_1$  is the specific volume of the solvent,  $m_3$  is the molality of salt in the solvent, and  $M_2$  is the molar mass of the solute (Tanford, 1961).

For a pairwise interaction between two different species,  $B_{23}$  is  $\frac{Z_2 Z_3 \bar{v}_1}{4m_4 M_2 M_3}$ , where components 2 and 3 are the interacting macromolecules. The effect of the excluded volume of a hard sphere on the second virial coefficient is  $\frac{4\bar{v}_2}{M_2}$ , where  $\bar{v}_2$  and  $M_2$  are the partial specific volume and molecular weight, respectively, of the solute. For a random coil such as dextran, the contribution due to excluded volume is  $\frac{32}{3} \pi (0.8R_G)^3$ , where  $R_G$  is the radius of gyration of the solute (Tanford, 1961). The contributions from both enthalpic interactions and excluded volume will add to result in the overall nonideality.

The equations for enthalpic and entropic contributions to  $B_2$  allow for the calculation of theoretical values for  $M/M_{app}$  for the three background molecules alone as well as for

GFP in high concentrations of the background molecules, which are presented in Figures 6 and 7 respectively.

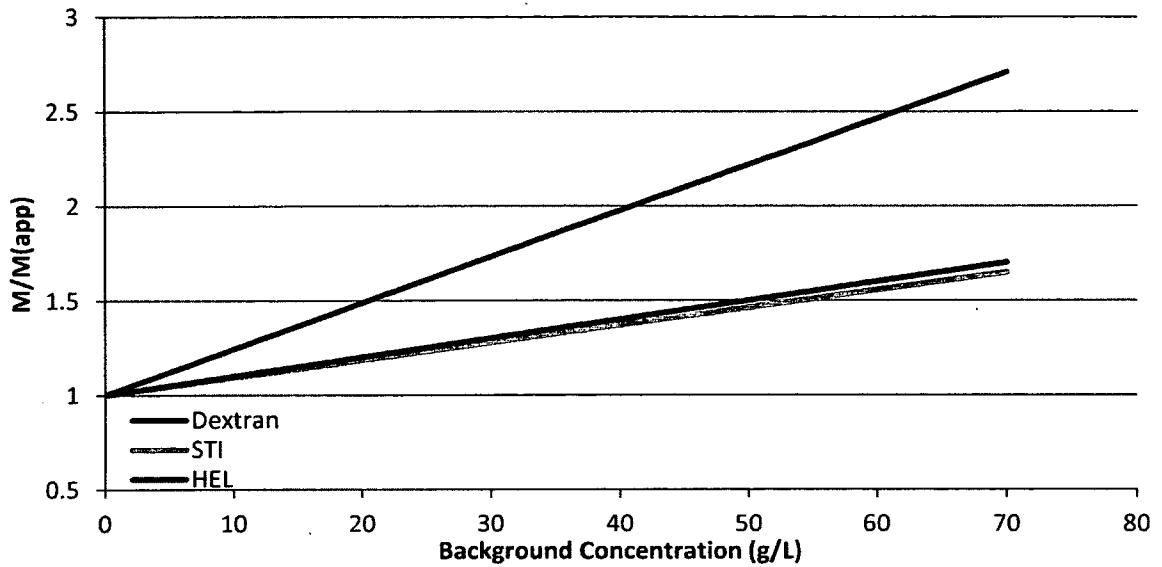


Figure 6. Calculated values of  $M/M_{app}$  for dextran, soybean trypsin inhibitor, and hen egg-white lysozyme based on the contribution of excluded volume and charge to the second virial coefficient for spheres from (Tanford, 1969). A partial specific volume of 0.703 ml/g was used for HEL and 0.735 ml/g was used for STI. A radius of gyration of 28 angstroms was used to calculate the excluded volume of the dextran random coil, based on (Tanford, 1969). A charge of 6.1 was used for HEL, and a charge of -8.6 was used for STI.

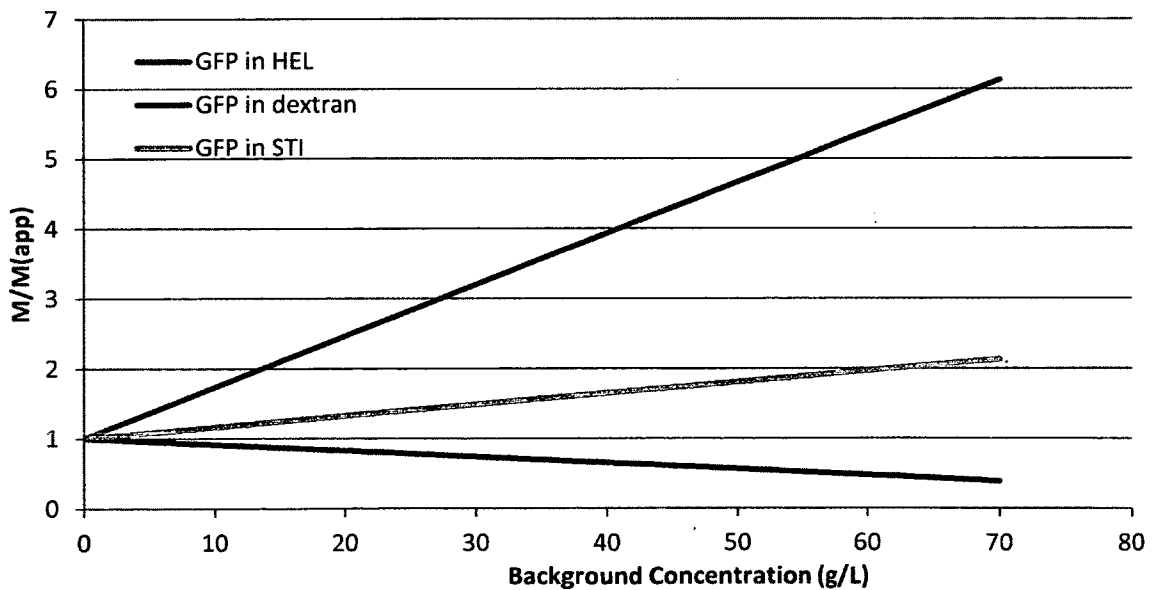


Figure 7. Calculated  $M/M_{app}$  for GFP in dextran, soybean trypsin inhibitor, and hen egg-white lysozyme. Calculations used are as described in previous figure. Additionally, pairwise charge-charge interaction equations were used (Tanford, 1969).

It may seem odd at first that the  $M/M_{app}$  for dextran increases so much more sharply with concentration than the other theoretical curves. However, it must be considered that dextran differs from both HEL and STI in that HEL and STI have compact globular structures in solution, whereas dextran is a highly branched glycan, more like a random coil, and it is expected that the occupied volume in solution of dextran will significantly higher than the proteins.

### **Experimental Hypotheses**

The hypotheses that these studies will test are the following:

1. The FDS will enable the tracking of a single component in a complex mixture. Because the signal molecule is the only visible species, the complexity of the solution will become irrelevant and it will be possible to assess the biophysical characteristics of GFP in any solution.
2. The nonideality of the tracer (GFP) will differ from the nonideality of the background molecule used (HEL, STI, dextran).
3. Sedimentation velocity can be used in place of sedimentation equilibrium and provide similar insights into interactions in complex solutions.
4. The proximity energy framework, when applied to a new system involving the molecules mAb 1, mAb 2, and mAb 3, can adequately account for the experimental data.

## CHAPTER I

### AU-FDS SEDIMENTATION EQUILIBRIUM OF BACKGROUND MOLECULES AND OF GFP IN HIGH CONCENTRATIONS OF BACKGROUNDS

#### Materials and Methods

##### Materials

Sodium chloride (S-9623, lot 47H0205) and dibasic sodium phosphate (S-0876, lot 29H0002) were purchased from Sigma. Potassium chloride (3040-01, lot B28363) was purchased from J.T.Baker. Monobasic potassium phosphate (P-285, lot 784276) was purchased from Fisher Scientific.

Dextran (D9260, lot 1382459 32908126, M= 9,000 – 11,000 Da) was purchased from Sigma.

Hen egg white lysozyme (L-6876, lot 13F-8211, E280 37,470 cm M-1, M= 14,313 Da), and soybean trypsin inhibitor (T9003, lot 010M7352V, E280 16,960 cm M-1, M= 20,095 Da).

The GFP clone was given to the lab by Dr. Eric Schaller of Dartmouth, and is GenBank Accession number U70496. The protein has an N-terminal hexa-HIS tag for purification followed by a thrombin cleavage site, and the calculated molecular weight is 30,838 Da (Davis and Vierstra, 1998). The origin sequence is shown below.

1 ggatccaagg agatataaca atgagtaaag gagaagaact tttcactgga gttgtcccaa  
61 ttcttgttga attagatggt gatgtaatg ggcacaaatt ttctgtcagt ggagagggtg  
121 aaggatgatgc aacatacggg aaacttacc ttaaatttat ttgcactact ggaaaactac  
181 ctgttccatg gccaacactt gtcactactt tcacttatgg tgttcaatgc tttcaagat  
241 accgatgatca tatgaagcgg cacgacttct tcaagagcgc catgcctgag ggatacgtgc  
301 aggagaggac catctctttc aaggacgacg ggaactacaa gacacgtgct gaagtcaagt  
361 ttgagggaga caccctcgtc aacaggatcg agcttaaggg aatcgatttc aaggaggacg  
421 gaaacatcct cggccacaag ttggaataca actacaactc ccacaacgta tacatcacgg  
481 cagacaaaca aaagaatgga atcaaagcta actcaaaaat tagacacaac attgaagatg  
541 gaagcgttca actagcagac cattatcaac aaaatactcc aattggcgat ggcctgtcc  
601 ttttaccaga caaccattac ctgtccacac aatctgcctt ttcgaaagat cccaacgaaa  
661 agagagacca catggtcctt cttgagtttg taacagctgc tgggattaca catggcatgg  
721 atgaactata caaataagag ctc

The translation is as follows:

MSKGEELFTGVVPIVVELDGDVNGHKFSVSGEGEGDATYGLKTLKFICTTGKLPVPWPTLVTTFTYGV  
QCFSRYPDHMKRHDFFKSAMPEGYVQERTISFKDDGNYKTRAEVKFEGDTLVNRIELKGIDFKEDG  
NILGHKLEYNVNSHNVIYITADKQKNGIKANFKIRHNIEDGSVQLADHYQQNTPIGDGPVLLPDNHYL  
STQSALS KDPNEKRDHMLLEFVTAAGITHGMDELYK

The clone was inserted into a Novagen pET-28a vector. The plasmid was transfected into an E. coli DH5 alpha strain and isolated as described previously (Kroe, 2005). The end result was a stock solution of 17  $\mu$ M GFP in PBS with greater than ninety five percent purity as measured by SDS-PAGE.

The clone contains a hexa-his tag for purification, and this tag was not removed from the GFP used in this study. The his tag is assumed to have minimal effects on the properties of the molecule, as this has been the case with some other molecules studied (Lin et. al., 2011).

## **Methods**

AU-FDS Sedimentation Equilibrium of GFP in High Concentrations of Background Molecules. Sedimentation equilibrium experiments were performed at 20°C in phosphate buffered saline (PBS), comprising 137 mM NaCl, 2.7 mM KCl, 10 mM Na<sub>2</sub>HPO<sub>4</sub>•2H<sub>2</sub>O, 2 mM KH<sub>2</sub>PO<sub>4</sub>, pH 7.4. Data were collected at rotor speeds of 20,000, 25,000, and 30,000 RPM in 4-sector Spin Analytical centerpieces with either quartz or sapphire windows and in an An60 Ti 4-hole rotor. Experiments were conducted by adding 0.94 µL of the 17 µM GFP stock solution to 400 µL of a concentration series (from 0 to 70 g/L) of each background molecule, resulting in a final GFP concentration of 40 nM. All stock solutions were dialyzed (1:100) against PBS changing the buffer two times at a 4 hour interval and once before dialyzing overnight.

Data were analyzed using the HeteroAnalysis software version 1.1.44 ( James L. Cole, Jeffrey W. Lary). The single ideal species model was used, with a partial specific volume of 0.738 mL/g and the densities of solutions reported previously (Kroe, 2005). The apparent molecular weight reported by the software for each background concentration was averaged over the 3 rotor speeds, and the GFP monomer molecular weight of 30,838 g/mol was divided by this value to yield values of M/M<sub>app</sub> used in the graphs.

Sedimentation equilibrium of high concentration backgrounds (dextran, STi, and HEL) with interference detection. Sedimentation equilibrium experiments were performed at 20°C in PBS. Data were collected at rotor speeds of 20,000, 25,000, and 30,000 RPM in a two sector charcoal-filled epon centerpiece, either Spin Analytical SEDVEL60K or Beckman, with sapphire windows and in an An60 Ti 4-hole rotor. All stock solutions



were dialyzed exhaustively as described above against PBS before dilutions were made using the dialysate.

The data were analyzed using the HeteroAnalysis software version 1.1.44. The single ideal species model was used, with a partial specific volume of 0.703 mL/g for HEL (Rhodes et. al., 1962), 0.735 mL/g for STI (Rackis et. al., 1962), and 0.611 mL/g for dextran (Granath, 1958). The solution densities and viscosities used were those measured previously by (Kroe, 2005). The apparent molecular weight reported by the software for each background concentration was averaged over the 3 rotor speeds, and the known monomer molecular weight (14,313 Da for HEL, 20,095 Da for STI, and 10,000 Da for dextran) was divided by this value to arrive at the values for  $M/M_{app}$ .

## Results

In order to gather information about the nonideality of the three background molecules alone, a series of sedimentation equilibrium experiments were performed using interference detection on a concentration series of dextran, soybean trypsin inhibitor, and hen egg white lysozyme. Also, sedimentation equilibrium experiments were performed using fluorescence detection, with GFP as a tracer in a concentration series of the three background molecules. The results from these experiments for each molecule are presented separately, and described below.

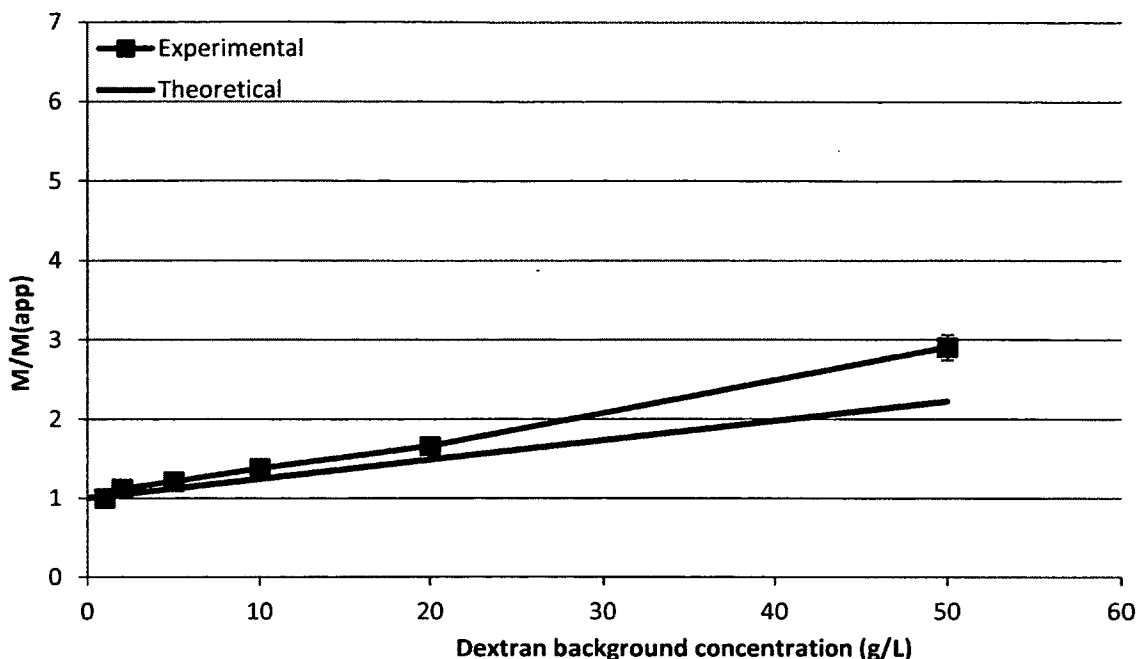


Figure 8. **Activity graph for dextran.** This graph summarizes a series of interference sedimentation equilibrium experiments of high concentrations of Dextran. The Y value of each data point in the experimental series is an average of one experiment conducted at rotor speeds, 20K rpm, 25k rpm, and 30K rpm. The black line represents the theoretical activity of dextran modeled as a random coil as discussed in the theory section.

Figure 8 displays the results of the sedimentation equilibrium experiment performed on dextran alone along with the theoretical  $M/M_{app}$  for dextran modeled as a random coil. Figure 9 presents these same results along with the results of the AU-FDS experiment of GFP in dextran, and also the theoretical  $M/M_{app}$  for GFP in dextran.

As can be seen in Figure 8,  $M/M_{app}$  increases with concentration more than is anticipated from the theoretical contribution of excluded volume to B2. The difference between the experimental and theoretical  $M/M_{app}$  can be explained in a number of ways, First, the  $0.8RG$  term used to calculate the theoretical  $M/M_{app}$  is an estimate and will change from lot to lot for dextran. Second, the estimate does not take into account preferential solvation of random coil chains, which will tend to increase the effective

volume (Tanford, 1961). Third, the slight upwards curve of the data could be evidence that the third virial coefficient is greater than zero, which would yield an increasing slope with concentration. Finally, the dextran sample used is a mixture of molecular weights which may influence  $M/M_{app}$ , i. e. for dextran  $M/M_{app}$  is an average value.

Assuming the nonideality shown by dextran in Figure 8 is solely a result of excluded volume, the effective volume of dextran would need to be 4.69 mL/g to account for the data, which corresponds to a radius of 26.5 Å. The solution radius when calculated from the partial specific volume of a compact sphere is 13.4 Å. The radius of a 10 kDa dextran molecule is 28.7 Å when measured via light scattering in solution (Fundueanu et. al., 1999), although this measurement was done on a different lot of dextran than that used in this study. As the radius back-calculated from the activity shown in Figure 8 is close to the radius measured experimentally, it would seem that excluded volume alone can account for the high activity of dextran.

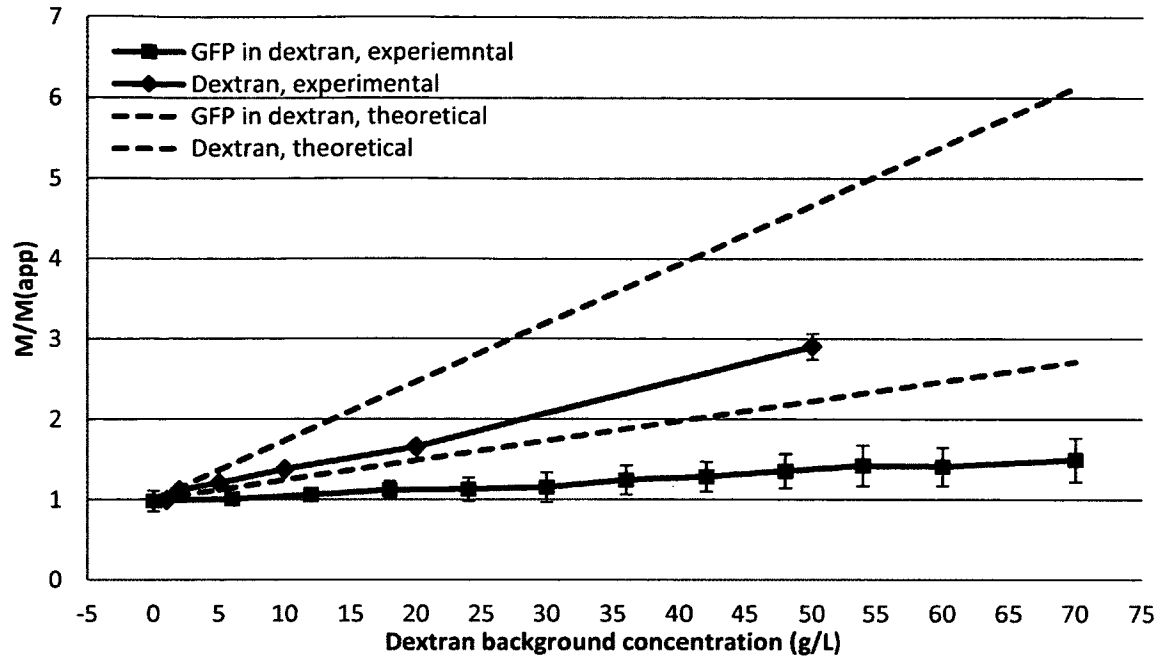


Figure 9. Activity graph for dextran and for GFP in dextran. This graph summarizes a series of interference and FDS sedimentation equilibrium experiments of high concentrations of Dextran and of GFP in high concentrations of dextran. The Y value of each data point in the experimental series is an average of one experiment conducted at rotor speeds, 20K rpm, 25k rpm, and 30K rpm. The dashed lines represent the theoretical activity of dextran and of GFP in dextran seen in Figures 6 and 7.

When the  $M/M_{app}$  of GFP in dextran in Figure 9 is compared to the theoretical  $M/M_{app}$  for GFP in dextran, it can be seen that the experimental  $M/M_{app}$  is significantly lower than the calculated value. This difference can again be explained by an assumption of the model. The quantity  $1 + M_{(j,app)}/M_{(i,app)} C_j (\partial \ln \gamma_i) / (\partial C_j)$  uses a ratio of apparent molar masses to account for the difference in size between  $i$  and  $j$ . When comparing the sizes of a protein and a sugar, the use of molar masses can be misleading. While the ideal molar mass of dextran is 9 – 11 kDa and the ideal molar mass of GFP is 30.8 kDa, dextran has a far larger effective volume in solution than does GFP.

When the  $M/M_{app}$  of a trace quantity of GFP in dextran in Figure 9 is compared to the activity of dextran alone, it can be seen that the GFP activity is about half that of dextran. There are at least three possible explanations for this difference between the  $M/M_{app}$  for dextran alone and GFP in dextran. First, the difference could be an entropic effect in that dextran is so much larger than GFP in solution, it would be less costly energetically to fit a molecule of GFP into a solution with a high concentration of dextran than it would be to add a molecule of dextran to a solution containing a high concentration of dextran. Second, the difference between the calculated and experimental activity could be explained by weak attraction between GFP and dextran that is not available in dextran-dextran interactions. A third possibility is that GFP is able to penetrate portions of the effective volume of dextran that dextran itself cannot. While a search of the literature yielded no evidence that dextran is a non-reentrant random coil, if this is the case, there would be more volume available to GFP in a solution of dextran than would be available to a molecule of dextran, and thus the expected activity of GFP in a solution of dextran would be lower than the activity of the dextran alone in solution. This third possible cause is similar to the first in that both result in more volume being available to GFP, but in the latter case some of the volume is inside of the dextran coils, whereas in the first case only the volume between molecules is considered accessible.

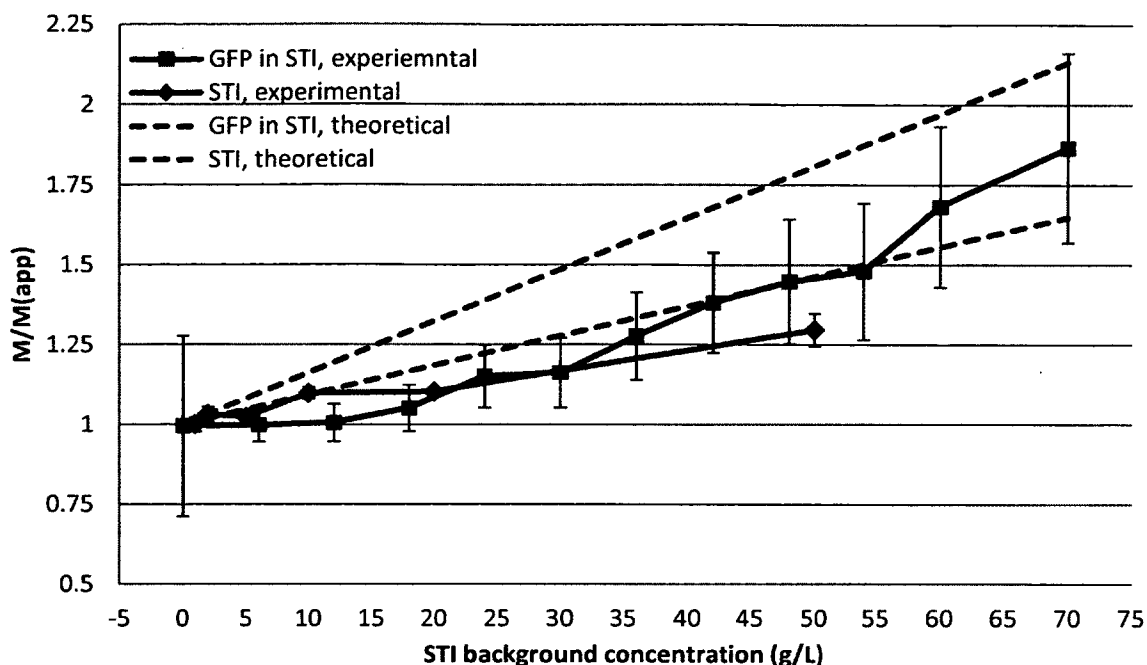


Figure 10. Activity graph for STI and for GFP in STI. This graph summarizes a series of interference and FDS sedimentation equilibrium experiments of high concentrations of STI and of GFP in high concentrations of STI. The Y value of each data point in the experimental series is an average of one experiment conducted at rotor speeds, 20K rpm, 25k rpm, and 30K rpm. The dashed lines represent the theoretical activity of STI and of GFP in STI calculated in the theory section.

Figure 10 displays the theoretical and experimental  $M/M_{app}$  for both STI alone and GFP in STI. The plot representing the ratio of  $M$  to  $M_{app}$  for STI alone falls significantly below the theoretical  $M/M_{app}$  for STI alone. This result is unexpected, as STI is anionic and, thus should be subject to charge-charge repulsion, which would tend to increase  $M/M_{app}$  more strongly with concentration compared to a solution of similarly sized neutral molecules. Results in Figure 10 suggest that STI may exhibit some self-attractive interactions not being accounted for in the calculations.

When the  $M/M_{app}$  for GFP in STI is compared to the theoretical  $M/M_{app}$  for GFP in STI (Figure 10), it can be seen that most points in the experimental data fall significantly below what is calculated based solely on excluded volume and charge. This difference in

M/M<sub>app</sub> could be due to an effect similar to that seen when comparing the experimental and theoretical M/M<sub>app</sub> for STI alone, i.e. that there are some attractive interactions between GFP and STI.

When comparing the experimental M/M<sub>app</sub> for STI alone and GFP in STI (Figure 10), the differences between the activity of STI by itself and that of GFP in STI are not significant, which is expected as GFP and STI are both anionic and have a similar charge magnitude. The difference in size between GFP and STI would tend to increase the M/M<sub>app</sub> of GFP in STI by about 0.3 at 70 g/L when compared to the activity of STI alone, which is within experimental error.

The theoretical and experimental M/M<sub>app</sub> for both HEL alone and GFP in HEL is shown in Figure 11. The observed nonideality seen in Figure 11 leads to the conclusion that HEL experiences slight attractive nonideality, as M/M<sub>app</sub> hovers slightly below one over the full range of concentration. Theory suggests that HEL should exhibit repulsive nonideality due to its net charge of 6.1. The difference between the theoretical and experimental data is likely due to the large area of positive charge that can be seen in the electrostatic surface potential map of the molecule (Figure 2) which indicates that HEL has a dipole moment. This dipole moment will result in attractive proximity energies such as charge-dipole, dipole-dipole, or dipole-induced dipole. A search of the literature confirms that at neutral pH HEL is prone to self-association (Behlke, 1999), but the mechanism of association is uncertain. Proposed mechanisms include the introduction of a tryptophan indole from HEL into an uncharged region of an adjacent

HEL (Banerjee et. al., 1975) and the interaction of a histidine residue on HEL with negative residues of an adjacent HEL (Shindo et. al., 1977).

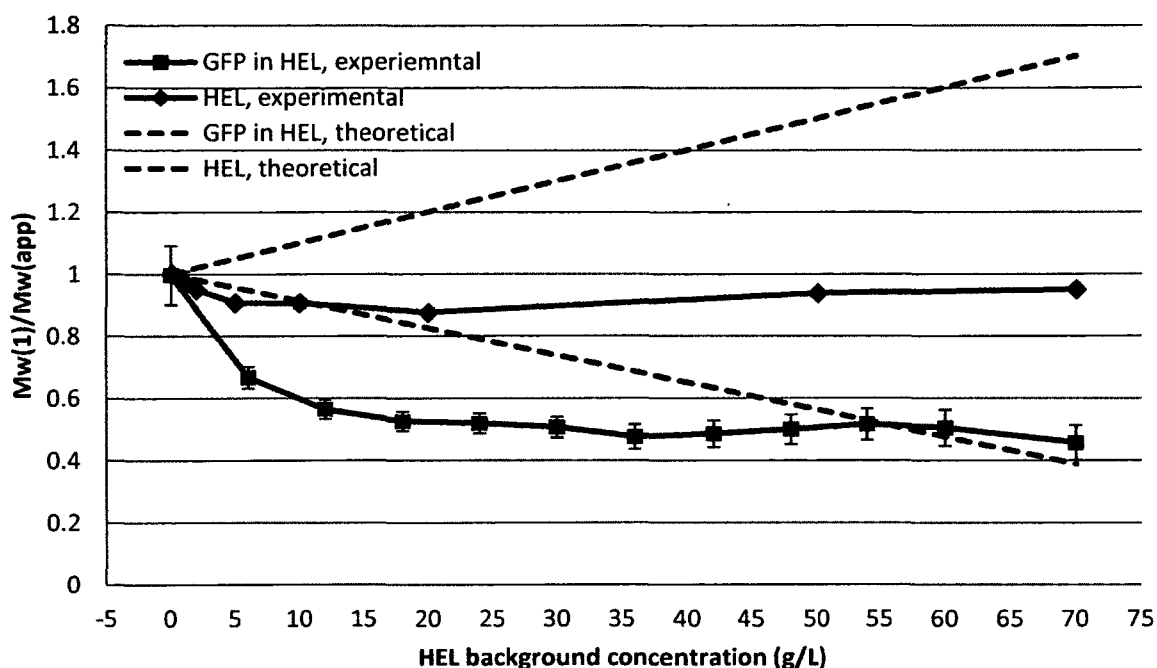


Figure 11. **Activity graph for HEL and for GFP in HEL.** This graph summarizes a series of interference and FDS sedimentation equilibrium experiments of high concentrations of HEL and of GFP in high concentrations of HEL. The Y value of each data point in the experimental series is an average of one experiment conducted at rotor speeds, 20K rpm, 25k rpm, and 30K rpm. The dashed lines represent the theoretical activity of HEL and of GFP in HEL calculated in the theory section.

The chemical activity of GFP in high concentrations of HEL is significantly lower than that of HEL by itself. The low activity of GFP in HEL is consistent with there being more favorable electrostatic interactions between GFP and HEL than HEL has with itself.



## CHAPTER II

### SEDIMENTATION VELOCITY OF GFP IN HIGH CONCENTRATIONS OF BACKGROUND MOLECULES

#### **Materials and Methods**

##### **Materials**

Materials used were as described in previous chapter.

##### **Methods**

Sedimentation velocity experiments were performed at 20°C in PBS. Data were collected at a rotor speed of 45, 000 RPM in two sector charcoal-filled epon centerpieces, either Spin Analytical SEDVEL60K or Beckman, with either quartz or sapphire windows and in an An60 Ti 4-hole rotor. Experiments were conducted by adding 0.94  $\mu\text{L}$  of a 17  $\mu\text{M}$  GFP stock solution to 400  $\mu\text{L}$  samples of a concentration series (from 0 to 20 g/L) of each background molecule. All molecules were dialyzed against PBS in a ratio of 1:100 changing buffer two times at a 4 hour interval and once before dialyzing overnight.

The data were analyzed using the DCDT+ software version 2.3.2 (John S. Philo). A partial specific volume of 0.738 mL/g was used for GFP (Bean, 2004). The solution densities and viscosities used were measured previously (Kroe, 2005).

## Results

In order to obtain more information about the interactions of GFP with these three background molecules, the sedimentation velocity (described in introduction) method was used. While sedimentation equilibrium excels at giving thermodynamic insights into the activity and interactions of GFP in a solution, sedimentation velocity provides some solution fractionation, hence more detailed information is available regarding the species size distribution. The size distribution can provide insights into what components GFP may be interacting with, the homogeneity of the interaction, and sometimes the stoichiometry of interactions may be revealed (Cole et. al., 2008). However, the higher resolution information from velocity analysis may be complicated by hydrodynamic nonideality. If sedimentation velocity analysis can provide the same insights into the thermodynamic nonideality of solutions as sedimentation equilibrium analysis, albeit qualitatively, then sedimentation velocity experiments will be preferred for future work because they are far more convenient and less time consuming to conduct than sedimentation equilibrium experiments.

As GFP is present in trace amounts (40 nM) in these experiments, and because GFP is larger than the three background molecules, GFP will sediment in the plateau concentration of the background molecule for the duration of the experiment.

Sedimentation velocity was performed on GFP up to 4  $\mu\text{M}$  and no self-association was observed (see Figure 4). As shall be seen, the activity coefficients of GFP in these studies are not large enough to drive the effective concentration of GFP above 4  $\mu\text{M}$ , therefore any forms of GFP other than monomer (2.7s) will be assumed to result from GFP interacting with the background molecule.

Sedimentation velocity experiments were performed on 40 nM GFP in the three background molecules at 0.1 g/L, 1 g/L, 5 g/L, and 20 g/L. All of the analyses of the data may be found in appendix B. Presented here are the data for 40 nM GFP in 20 g/L of dextran, HEL, and STI in Figures 12, 13, and 14 respectively.

Present in all these Figures are other GFP forms. These other forms were fit by a second Gaussian (Gaussian 2) by DCDT+. The percent of the signal that this faster moving material accounts for in all experimental conditions is displayed as blue bars in Figure 16.

Care must be taken when sedimentation velocity is applied to concentrated solutions. As discussed in the Introduction, the underlying assumption of a dilute solution used to interpret the  $g(s^*)$  curve does not hold in highly concentrated solutions of interacting components. Because most of the data in this thesis violate this assumption, a Gaussian peak resulting from a fit to the data does not necessarily correspond to a sedimenting species.

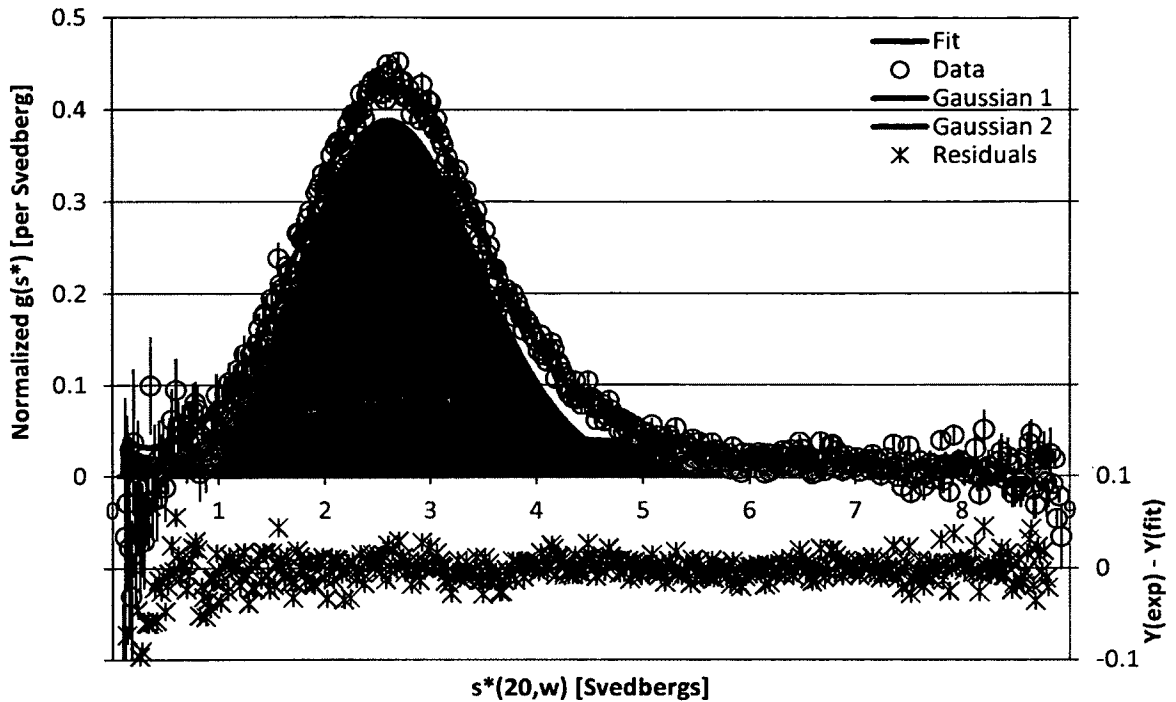


Figure 12. **40 nM GFP in 20 g/L dextran.** Sedimentation velocity data were acquired with the fluorescence detection system. On the primary axis is plotted the  $g(s^*)$  distributionw (Data), and Gaussians 1 and 2 with the area under the curve colored to indicate which portions of the total signal they can account for. Also on the primary axis is the proposed fit to the data, which represents the sum of the Gaussian curves. Residuals are plotted on the secondary axis.

The sedimentation velocity experiment of 40 nM GFP as a tracer in 20 g/L dextran, seen in Figure 12, shows a main peak at about 2.7 s, fitting to a molecular weight of 30.80 kDa, which is the molar mass expected for GFP. Curiously, there is also an extremely broad peak centered at about 4 s. This faster moving material is evidence of larger forms of GFP, and provides evidence for weak attractive interactions between GFP and dextran. This loose interaction could be between GFP and any number of dextran molecules, resulting in a broad distribution of GFP forms, all of which would sediment faster than 2.7 s. Alternatively, if GFP is able to penetrate the interior volume

of dextran as discussed earlier, this larger GFP form could be evidence for GFP being entrained in the dextran.

Another possibility is that the data fit by the second Gaussian may be an instrumental artifact. For example, because the density and viscosity of the solution in the plateau region decreases with time due to radial dilution, the  $s$  of GFP will increase over the course of the experiment. It could be that this broad Gaussian has been added to account for this effect. However, the results from the next section, where adding an excipient was able to eliminate the need for a second Gaussian to fit the data, argue against this hypothesis.

The GFP tracer in the other background molecules routinely had a second broad peak sedimenting at sedimentation coefficients greater than 2.7  $s$  similar to that seen in Figure 12 (see Figures 13 and 14). The one exception to this observation GFP in 0.1 g/L HEL (Figure 16). Under the hypothesis that the amount of signal under this second peak can be viewed as a measure of the degree of non-specific interaction between the tracer and the background, one would expect the GFP in HEL conditions to have among the highest concentrations of this second Gaussian, as the charge-charge attraction between GFP and HEL should be among the strongest non-specific interactions present in these experiments. This high level of nonspecific interaction is indeed what is seen, with GFP in 20 g/L HEL having among the highest concentrations of the faster material, and with the concentration of the higher  $s$  material increasing with increasing concentrations of HEL (Figure 16).

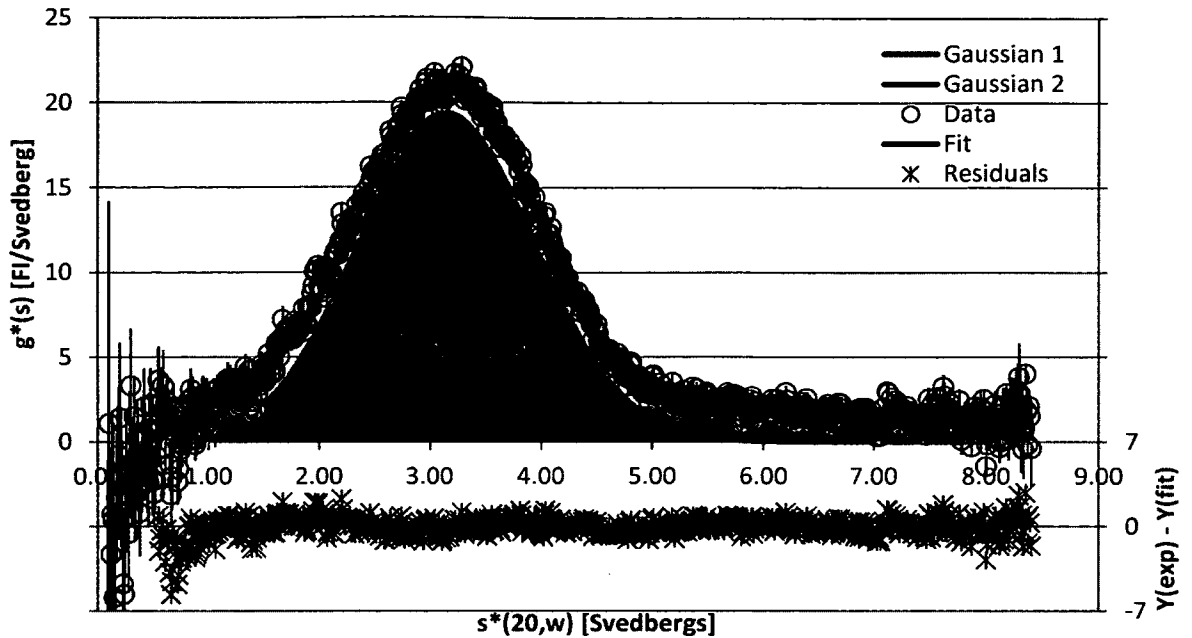


Figure 13. **40 nM GFP in 20 g/L HEL.** Sedimentation velocity data were acquired with the fluorescence detection system. On the primary axis is plotted the experimental data (Data), and Gaussians 1 and 2 with the area under the curve colored to indicate which portions of the total signal they can account for. Also on the primary axis is the proposed fit to the data, which represents the sum of the Gaussian curves. Residuals are plotted on the secondary axis.

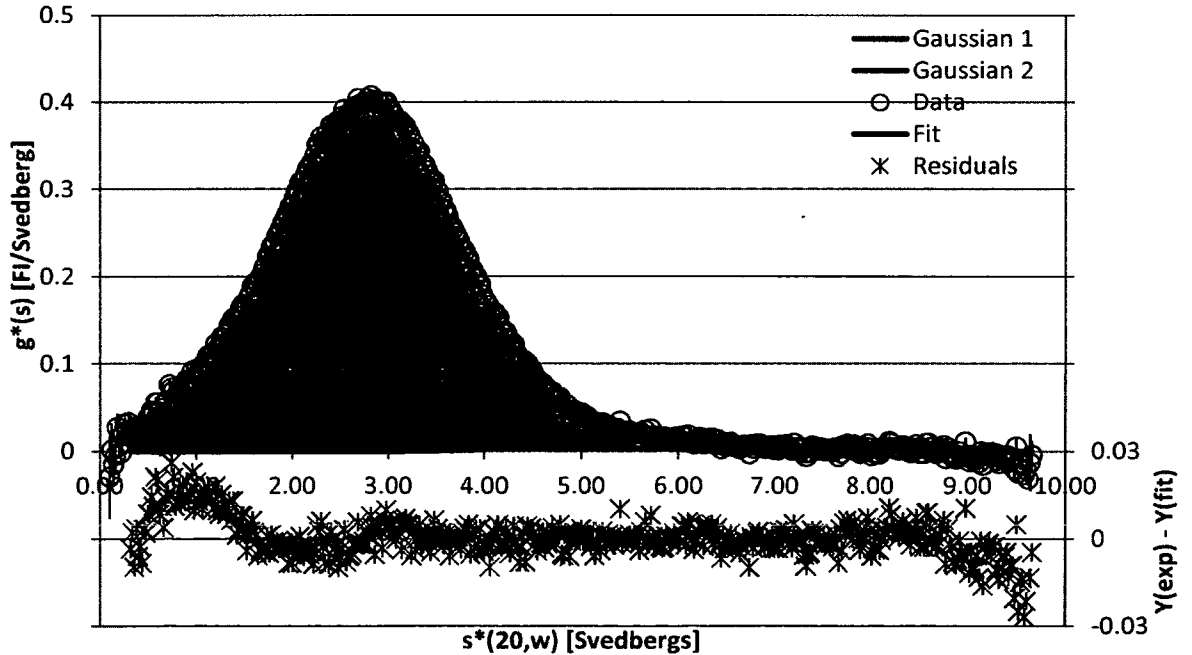


Figure 14. **40 nM GFP in 20 g/L STI.** Sedimentation velocity data were acquired with the fluorescence detection system. On the primary axis is plotted the experimental data (Data), and Gaussians 1 and 2 with the area under the curve colored to indicate which portions of the total signal they can account for. Also on the primary axis is the proposed fit to the data, which represents the sum of the Gaussian curves. Residuals are plotted on the secondary axis.

Similarly, on the basis of charge-charge repulsion, one would expect the GFP in STI conditions to have among the lowest concentrations of this faster material, as charge-charge repulsion should overpower weaker attractive interactions. Mostly, this low level of nonspecific interaction is what is seen. At any given concentration of STI, the amount of the faster material is less than that at an equivalent concentration of the other two background molecules. The only exception to this observation is at 0.1 g/L STI where the faster material accounted for a 9.5 percent of the signal, as there was a lower concentration of faster material in the 0.1 g/L HEL condition at 1.3 percent of signal (Figure 16).

The amount of nonspecific interaction appears to decrease with increasing concentrations of STI. If STI were slightly self-attractive, it would be consistent both with the lower than expected activity of STI seen in Figure 10 and with these data in Figure 16. Essentially STI:STI interactions would be out competing STI:GFP interactions at higher concentrations. It should be noted that any interaction between GFP and STI was unexpected, and warrants further study, perhaps by conducting similar experiments with GFP in high concentrations of other small anionic crowding molecules.

As the interactions between GFP and dextran are subject to neither charge-charge repulsion nor charge-charge attraction, one might expect that the degree of nonspecific binding present between GFP and a background composed of dextran molecules would be midway between that of HEL and STI, since electrostatics would suggest attractive interactions will be greatest between GFP and HEL and least between GFP and STI. However, Figure 16 reveals a level of non-specific interaction between GFP and dextran

similar to that of HEL, with no obvious trend in the amount of larger GFP forms with concentration of dextran. This indicates that GFP may have a similar degree of nonspecific interaction with both dextran and HEL, though the nature of the interactions may be different.



## CHAPTER III

### USE OF EXCIPIENTS TO IDENTIFY THE CAUSE OF THE FASTER GFP FORMS

#### **Materials and Methods**

##### **Materials**

Materials used were as described in Chapter I.

##### **Methods**

Methods used included the sedimentation velocity method, described in Chapter II.

##### **Results**

The degree of nonspecific interaction between GFP and dextran was unexpected. To investigate what manner of interaction could lead to the formation of these larger GFP forms, a single condition where the faster material was present was chosen, 40 nM GFP in 20 g/L dextran, and sedimentation velocity analysis was repeated for a few concentrations of various excipients known to prevent or reduce specific kinds of molecular interactions. The excipients used were urea, known to reduce hydrophobic interactions (Zangi et. al., 2008), sorbitol, known to reduce aggregation by stabilizing the

secondary structure of proteins (An, 2003), glycine, known to increase the dielectric constant of a solution and thereby reduce electrostatic interactions (Pattanaboonmee et. al., 2011), and NaCl, known to reduce electrostatic interactions (Parsegian and Gingell, 1972). The effect of each excipient is summarized in Figure 15. Two molar NaCl was the sole condition seen to eliminate the need for a 2<sup>nd</sup> Gaussian to fit the data. This excipient is known to reduce both electrostatic interactions (Parsegian and Gingell, 1972) and hydrogen bonding (Belnikovich et. al., 1989). This result prompted the examination of the effect of 2 M NaCl on the interaction between GFP and the other background molecules, STI and HEL. The results are shown in Figure 16 as green bars.

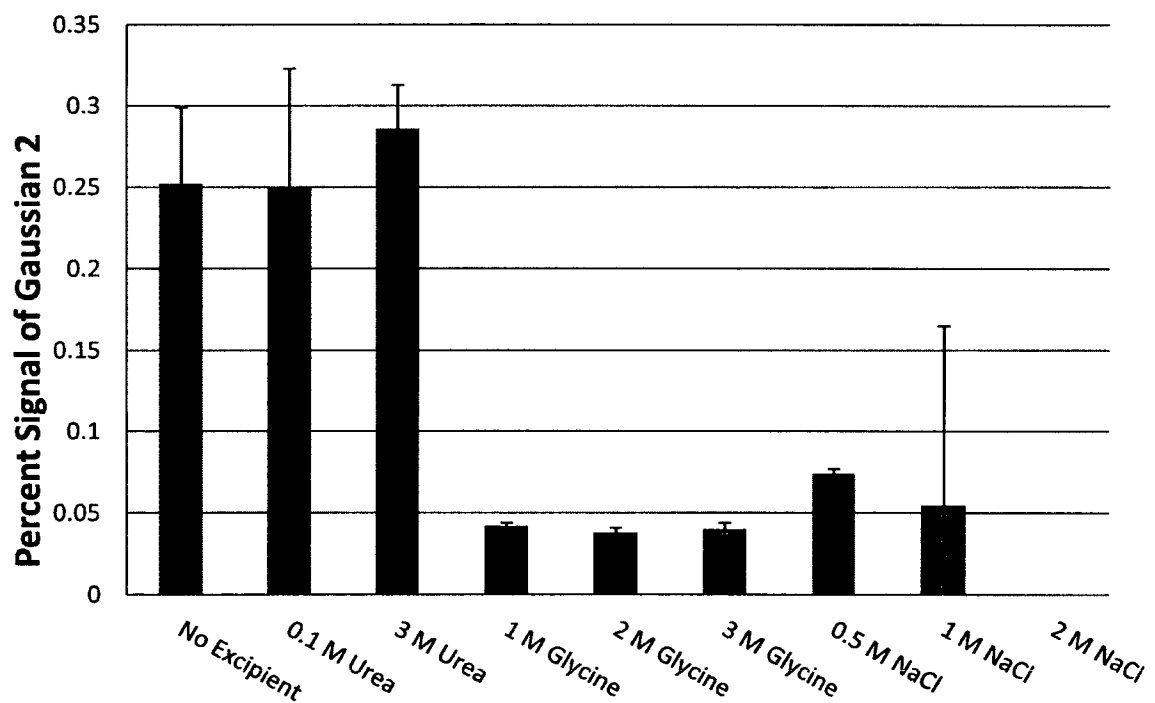


Figure 15. Amount of faster material present in a solution of GFP and dextran upon addition of excipients. A summary of the fits to  $g(s^*)$  plots from sedimentation velocity experiments of 40 nM GFP in 20 g/L dextran in several short concentration series of the excipients urea, sorbitol, glycine, and NaCl. No data being available for the parameters corresponding to Gaussian 2 indicates that the signal can be accounted for by a single Gaussian (no improvement in RMS deviation when fit to a multiple species model).

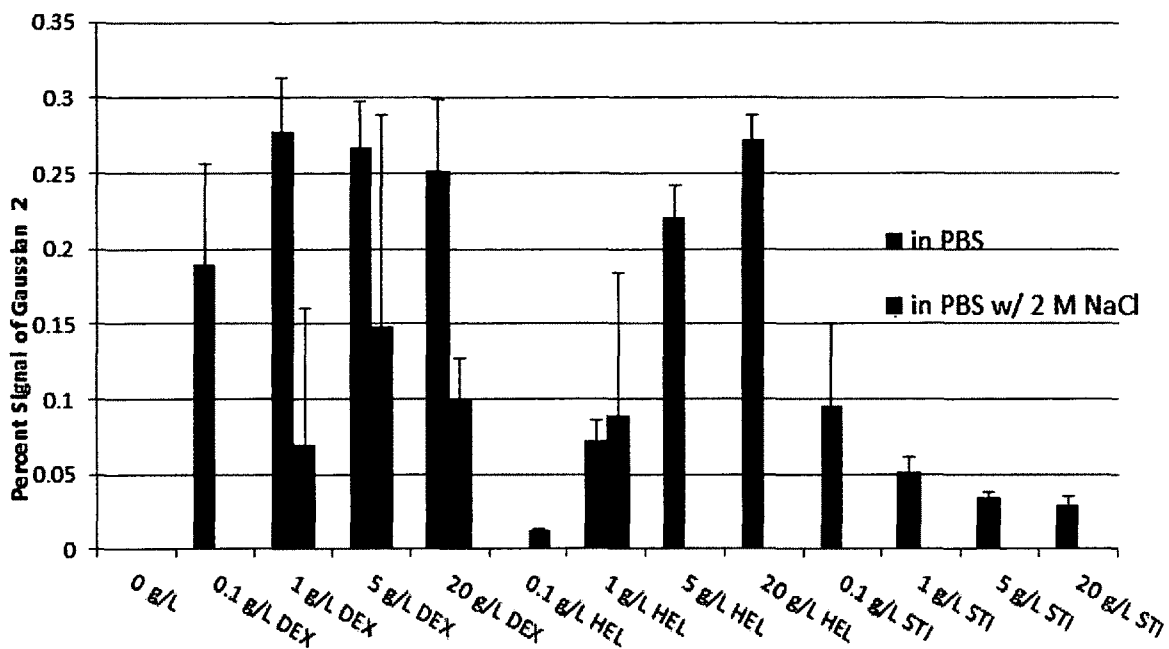


Figure 16. Amount of faster material present with and without addition of 2 M NaCl. A summary of the fits to  $g(s^*)$  plots from sedimentation velocity experiments of 40 nM GFP in three concentration series of the molecules dextran, hen egg-white lysozyme, and soybean trypsin inhibitor, with and without addition of 2 M NaCl. No data being available for the parameters corresponding to Gaussian 2 indicates that the signal can be accounted for by a single Gaussian (no improvement in RMS deviation when fit to a multiple species model).

Upon addition of 2 M NaCl (Figure 16), the concentration of larger GFP forms in the GFP in HEL experimental conditions was eliminated almost entirely. This result is in accordance with the hypothesis that the larger GFP forms (indicated by the blue bars in Figure 16) resulted primarily from attractive electrostatic interactions.

Somewhat more surprising is that 2 M NaCl appears to have had a similar effect on GFP when STI is the crowding molecule. This result is unexpected in that STI should not have favorable charge-charge interactions with GFP since STI and GFP are both anionic. Possible explanations include a structural change in either GFP or STI in 2 M salt or a reduction of any favorable electrostatic interactions that exceed the shielding of the charge-charge repulsion.

Also unexpected is that the addition of 2 M salt eliminated the high molecular weight GFP forms present with dextran as the background molecule, with the exception of the 20 g/L dextran condition in Figure 16, where the level of large GFP forms was not eliminated, but reduced significantly. These results indicate that while charge-charge interactions between GFP and dextran can account for most of the higher GFP forms seen in Figure 16, electrostatic interactions cannot account for all of the interactions.

The results in two molar NaCl seem to point towards two unintuitive conclusions. One is that under conditions of high concentrations of crowding molecules, GFP can have attractive electrostatic interactions with a molecule of the same signed charge, as evidenced by the reduction of large GFP forms upon addition of salt in all of the STI conditions in Figure 16.

The other surprising conclusion is that GFP can have favorable electrostatic interactions with dextran, a purported neutral, inert molecule. While this finding seems odd, both the sedimentation velocity results, and the sedimentation equilibrium results are consistent with there being favorable GFP:dextran electrostatic interactions. Although salt has also been seen to weaken hydrogen bonding between polymers (Belnikovich et. al., 1989), urea, when used as an excipient, also reduces hydrogen bonding (Usha and Ramasami, 2002), and urea was seen to have no effect on the interaction between dextran and GFP (Figure 15). However, the fact that 2 M NaCl was unable to completely eliminate high molecular weight GFP forms of GFP in 20 g/L dextran (Figure 16) indicates that the larger GFP forms cannot be accounted for solely by electrostatic interactions. Perhaps some manner of favorable entropic interaction

also is at work. One attractive hypothesis is that GFP is, in fact, becoming entrained in the dextran coils.

## CHAPTER IV

### SEDIMENTATION VELOCITY OF GFP AND ANTI-GFP ANTIBODY IN HIGH CONCENTRATIONS OF BACKGROUND MOLECULES

#### Materials and Methods

##### Materials

Materials used were as described in Chapter I.

##### Methods

Methods used included the sedimentation velocity method, described in Chapter II.

#### Results

In order to examine the effects of crowding on a multi-component interacting system, sedimentation velocity experiments were performed with the AU-FDS on 40 nM GFP and 40 nM anti-GFP in varying concentrations of the three background molecules. The interaction between GFP and anti-GFP has been characterized previously (Kroe, 2005) and was found to form a 1:1 complex with a 1 nM Kd. In this set of experiments, the anti-GFP antibody is unlabeled, so the only species visible to the FDS are free GFP

and the GFP, anti-GFP complexes. Additionally, since the antibody has such a high affinity for GFP, one would expect to see, in these experimental conditions, only a single peak representing the GFP:anti-GFP complex, and possibly an additional peak representing GFP<sub>2</sub>:anti-GFP complex. As shall be seen, there is no experimental evidence for the GFP<sub>2</sub>:anti-GFP complex.

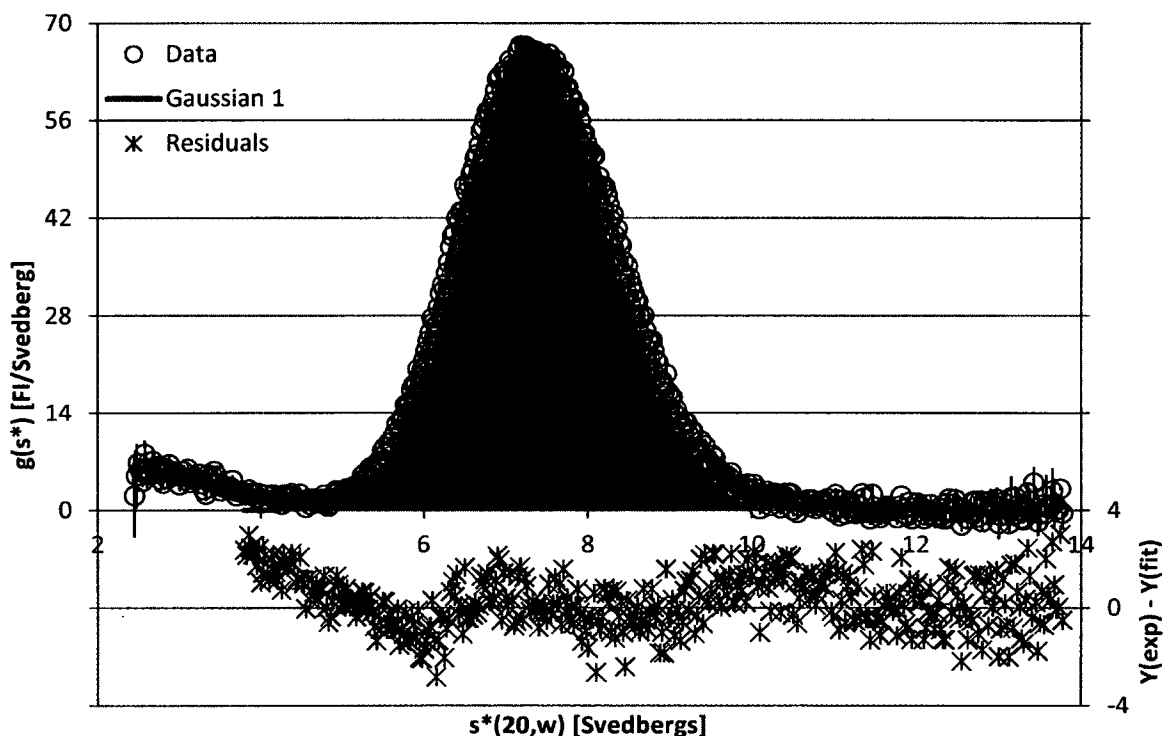


Figure 17. **40 nM GFP, 40 nM anti-GFP in PBS.** A  $g(s)$  plot from a sedimentation velocity experiment. On the primary axis is plotted the experimental data (Data), and a putative plot for the Gaussian that represents the proposed fit to the data, with the area under the curve colored to indicate which portions of the total signal it can account for. Residuals are plotted on the secondary axis. Data were acquired with the fluorescence detection system.

Figure 17 show the results of a sedimentation velocity experiment of 40 nM GFP and 40 nM anti-GFP in the absence of any crowding molecule. The Figure shows a single Gaussian peak at 7.1 s, consistent with a 1:1 complex of a 30,838 Da GFP and 150,000

Da IgG. This single peak indicates that anti-GFP is monovalent, and the absence of a Gaussian around 2.7 s (GFP) indicates that anti-GFP has a high affinity for GFP.

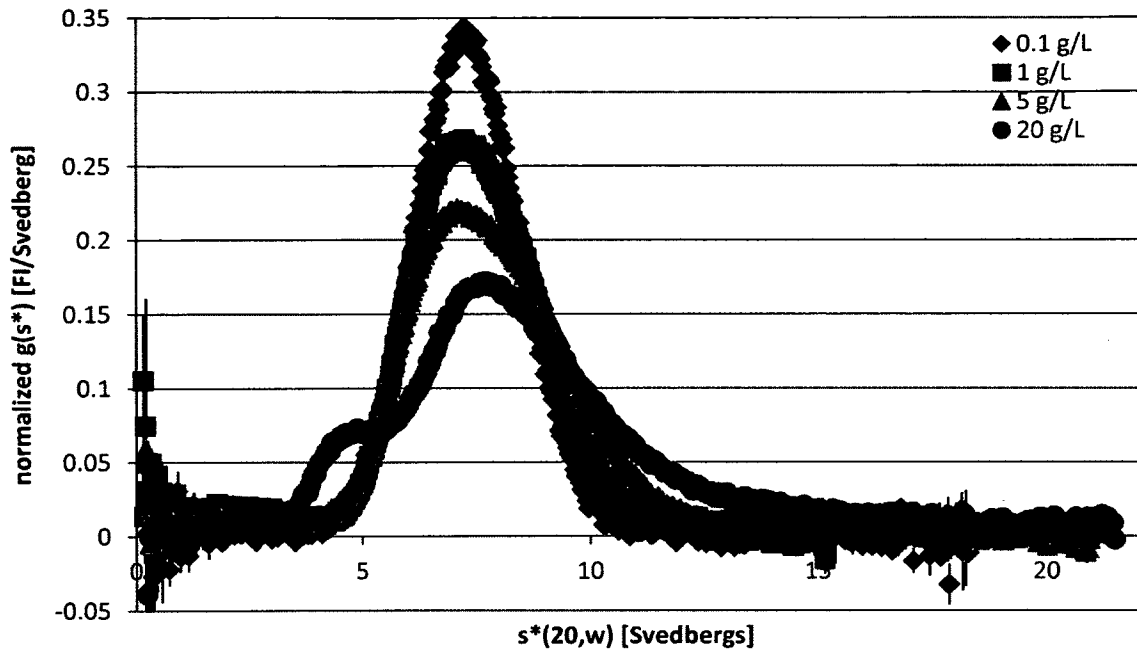


Figure 18. 40 nM GFP, 40 nM anti-GFP in HEL. Graph shows  $g(s)$  plots for a series of sedimentation velocity experiments in the concentration of HEL indicated by the legend. Data were acquired using the Fluorescence detection system.

The results of sedimentation velocity experiments of 40 nM GFP and 40 nM anti-GFP in 0.1 g/L, 1 g/L, 5 g/L and 20 g/L of HEL are shown in Figure 18. In the 0.1 g/L HEL condition in Figure 18, only one peak is seen. However, when the HEL concentration is increased to 1 g/L HEL, some additional features are present, one corresponding to free GFP, and the other running faster even than the GFP, anti-GFP complex, evidenced by slight skewing toward high  $s$  values when compared to 0.1 g/L HEL. This faster material is most likely the GFP, anti-GFP complex binding non-specifically with the background HEL, presumably in the same manner that the free GFP did in the previous set of experiments (Figures 12 to 14).



Each additional increase of HEL concentration results in higher degrees of nonspecific interaction between the GFP, anti-GFP complex and the background (Figure 18). There was no obvious trend in the amount of free GFP with concentration of HEL. However, free GFP being present at all indicates that high concentrations of HEL may interfere with the binding of GFP to anti-GFP, possibly by competing either by binding to the antibody or by binding to GFP. Since it has been demonstrated in previous experiments that GFP interacts favorably with HEL, the latter is likely at least partially responsible. Lastly, in the highest concentration of HEL a new peak developed, sedimenting between that of free GFP and the GFP:anti-GFP complex. It is unlikely that this is GFP binding to a degradation product of the antibody. Rather, GFP and HEL were seen to have a significant fraction of material in 20 g/L HEL that ran in the 3 to 5 s range (Figure 13), indicative of attractive interactions, and corroborating the idea that HEL could be behaving as a competitive inhibitor of the GFP:anti-GFP interaction. Alternatively, this peak could be a reaction boundary between any of the aforementioned species.

An experiment was conducted to test the hypothesis that the material seen in Figure 18 faster than 7s results from nonspecific interaction between the GFP:anti-GFP complex and HEL. Two molar NaCl was added to the solvent (Figure 21). While there were no peaks pointing to species sedimenting faster than the GFP:anti-GFP complex, the additional salt also interfered with the formation of the GFP:anti-GFP complex, as indicated by an increase in 2.7 s material.

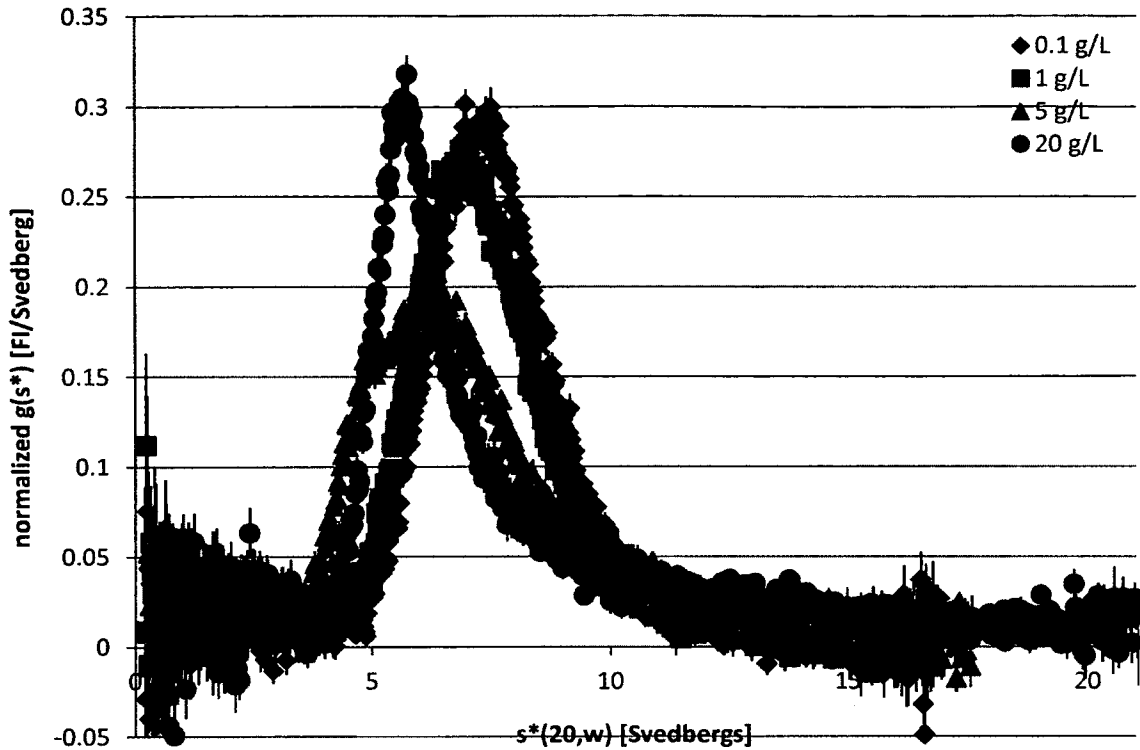


Figure 19. 40 nM GFP, 40 nM anti-GFP in Dextran. Graph shows  $g(s)$  plots for a series of sedimentation velocity experiments in the concentration of dextran indicated by the legend. Data were acquired using the Fluorescence detection system.

The results of sedimentation velocity experiments of 40 nM GFP and 40 nM anti-GFP in 0.1 g/L, 1 g/L, 5 g/L and 20 g/L of dextran are shown in Figure 19. The results were similar to those of the HEL conditions in that there was material present running faster than 7 s, indicative of nonspecific binding between the GFP:anti-GFP complex and the background molecule. The amount of this faster material tends to increase with increasing concentrations of dextran. There also appears to be a small amount of material sedimenting between 2 and 2.8 s, consistent with the presence of free GFP. The quantity of this slower material showed no trend with concentration of dextran. However, in this case the amount of the 2 to 2.8 s material was extremely small and

may be an artifact (this finding may be more visible in the individual plots in Appendix C).

Like the results of the sedimentation velocity experiments of GFP and anti-GFP in HEL, a reaction boundary appears in dextran between the peaks of free GFP and the GFP:anti-GFP complex. However in the case where dextran is the background molecule, the reaction boundary appears in the 5 g/L condition. As with the previous experiments of GFP alone in dextran, dextran appears to interact nonspecifically with the signal molecule, GFP:anti-GFP in the case, to a far greater extent than both HEL and STI.

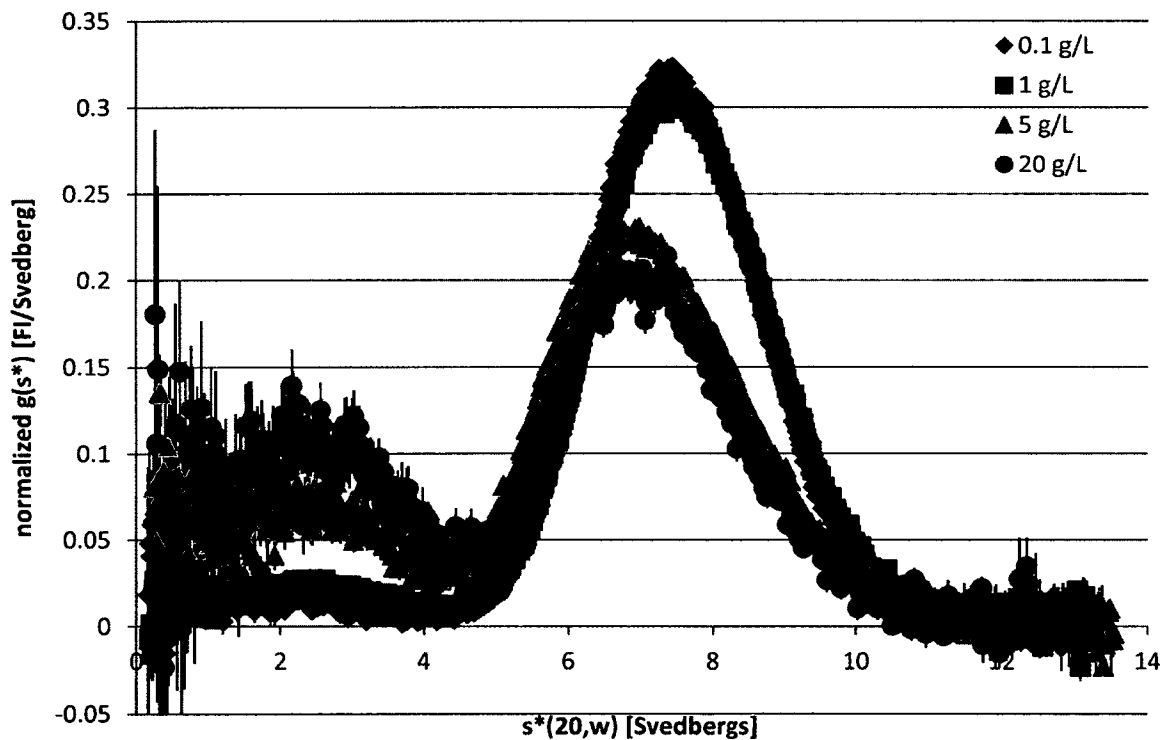


Figure 20. 40 nM GFP, 40 nM anti-GFP in STI. Graph shows  $g(s)$  plots for a series of sedimentation velocity experiments in the concentration of STI indicated by the legend. Data were acquired using the Fluorescence detection system.

The results of sedimentation velocity experiments of 40 nM GFP and 40 nM anti-GFP in 0.1 g/L, 1 g/L, 5 g/L and 20 g/L of STI are shown in Figure 20. Unlike the previous

experiment with HEL as a crowder, there was little or no nonspecific interaction between GFP and the background. Additionally in this case a peak at about 2.6 s is visible, similar to what would be expected for free GFP. There were larger amounts of free GFP present when compared to the HEL condition, and the amount of free GFP increases with increasing concentrations of STI. This increasing amount of free GFP may indicate that small anionic crowding molecules interfere with the binding of anti-GFP to GFP to a greater extent than small cationic molecules such as HEL. A likely cause is that STI binds to one of the reactants, thus acting as a competitive inhibitor. It is unlikely that this 2.6 s peak is a result of the Johnston-Ogston effect, since there was no characteristic peak in the concentration profile of the raw data.

The small amount of 2 to 2.8 s material in the GFP, anti-GFP in dextran experiments in Figure 18 is evidence that dextran interferes with the binding of GFP to anti-GFP, albeit to a far lesser extent than does a charged molecule such as HEL or STI. The finding that dextran interferes with GFP binding to anti-GFP to a lesser extent than both HEL and STI lends credence to the hypothesis that the interference is the result of competitive inhibition. The amount of the 2 to 2.8 s material was highest when STI was used as a crowder, meaning that STI was the most effective inhibitor of the GFP:IgG complex. This makes sense in that STI is similar to GFP in that it is anionic, and thus would compete GFP for anti-GFP binding better than the neutral or cationic molecules.

Individual plots and fits for all experiments in this section can be found in Appendix C. To examine the effects of 2 M NaCl on a multi-component interacting system, sedimentation velocity experiments were performed with the AU-FDS on 40 nM

GFP and 40 nM anti-GFP in high concentrations of the three background molecules and 2 M NaCl. Results were identical for all experimental conditions; results for 40 nM GFP, 40 nM anti-GFP in 20 g/L HEL and 2 M NaCl are shown in Figure 21 to serve as an example. These results indicate that the binding of GFP to anti-GFP is driven in part by favorable electrostatic interactions. This supports the hypothesis that STI acts as a competitive inhibitor as GFP and STI have similar electrostatic characteristics.

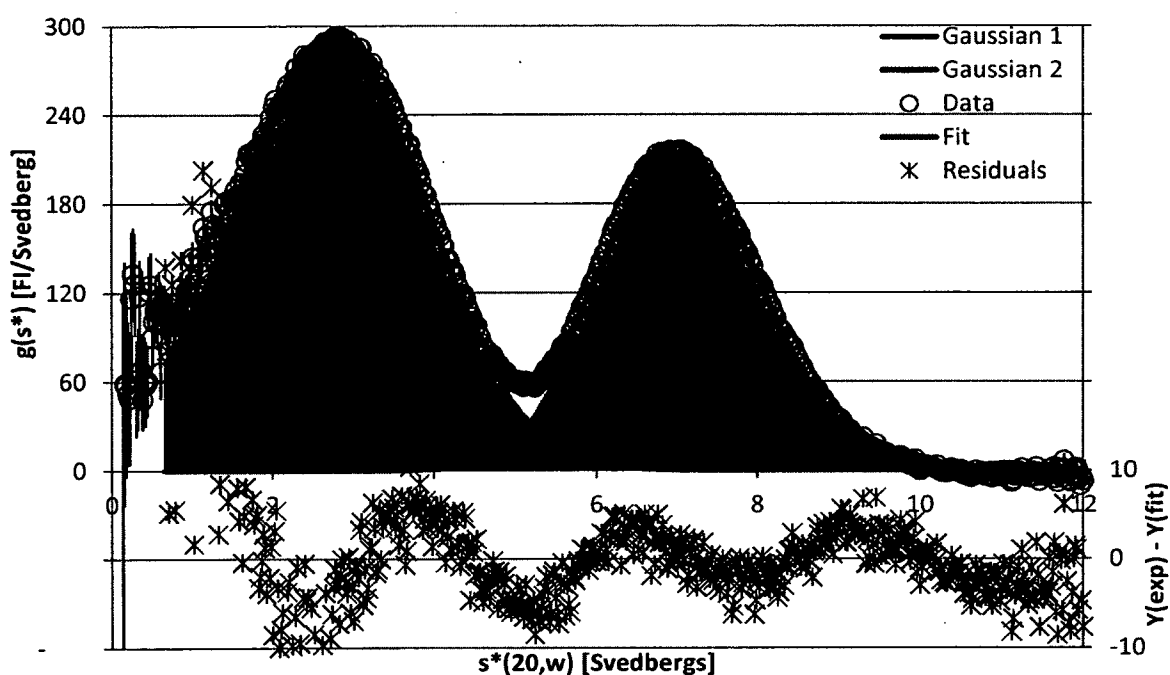


Figure 21. 40 nM GFP, 40 nM anti-GFP in 20 g/L HEL and 2 M NaCl. A  $g(s)$  plot from a sedimentation velocity experiment. On the primary axis is plotted the experimental data (Data), and putative plots for all Gaussians, with the area under the curve colored to indicate which portions of the total signal they can account for. Also on the primary axis is the proposed fit to the data. Residuals are plotted on the secondary axis. Data were acquired with the fluorescence detection system.

## CHAPTER V

### SEDIMENTATION VELOCITY OF GFP AND LABELED SERUM COMPONENTS IN SERUM

#### Materials and Methods

##### Materials

Materials used were as described in Chapter I. Additionally, human IgG (I4506, lot 050M7006,  $E_{280}$  203,000 cm M<sup>-1</sup>, M= 150,000 Da), and human serum albumin (A-1653, lot 64F-9349,  $E_{280}$  35,300 cm M<sup>-1</sup> Da) were purchased from Sigma. Human Serum (lot BRH146153) was purchased from Bioreclamation, Inc.

Fluorescent label (Alexa Flour 488 carboxylic acid tetrafluorophenyl ester, A20181, lot 871315) was purchased from Invitrogen.

##### Methods

Serum dilutions were made using PBS. HSA and IgG were labeled as directed by Molecular Probes Alexa Flour<sup>TM</sup> 488 Protein Labeling Kit (A-10235). Moles of dye per mole of protein was less than one in all cases. Methods used included the sedimentation velocity method, described in Chapter II.

## Results

As an opportunity to examine the  $M/M_{app}$  in a more complex, physiologically relevant crowded solution, sedimentation velocity experiments were performed on 40 nM GFP in twenty five percent, fifty percent, seventy five percent, and one hundred percent serum. In order to gain a better understanding of the sedimentation profile of the complex solution, sedimentation velocity experiments were also performed on labeled serum components, human serum albumin (HSA) and labeled poly clonal IgG, at the same concentrations that these components are found in serum. For controls, Figures 22 and 23 show the results of sedimentation velocity experiments of labeled HSA and labeled IgG alone in PBS. The  $s^*(20,w)$  values for both labeled components are similar to those of the unlabeled components, about 4 s for labeled HSA and 6.5 s for labeled IgG, although it must be noted that the s value for HSA is lower than expected.

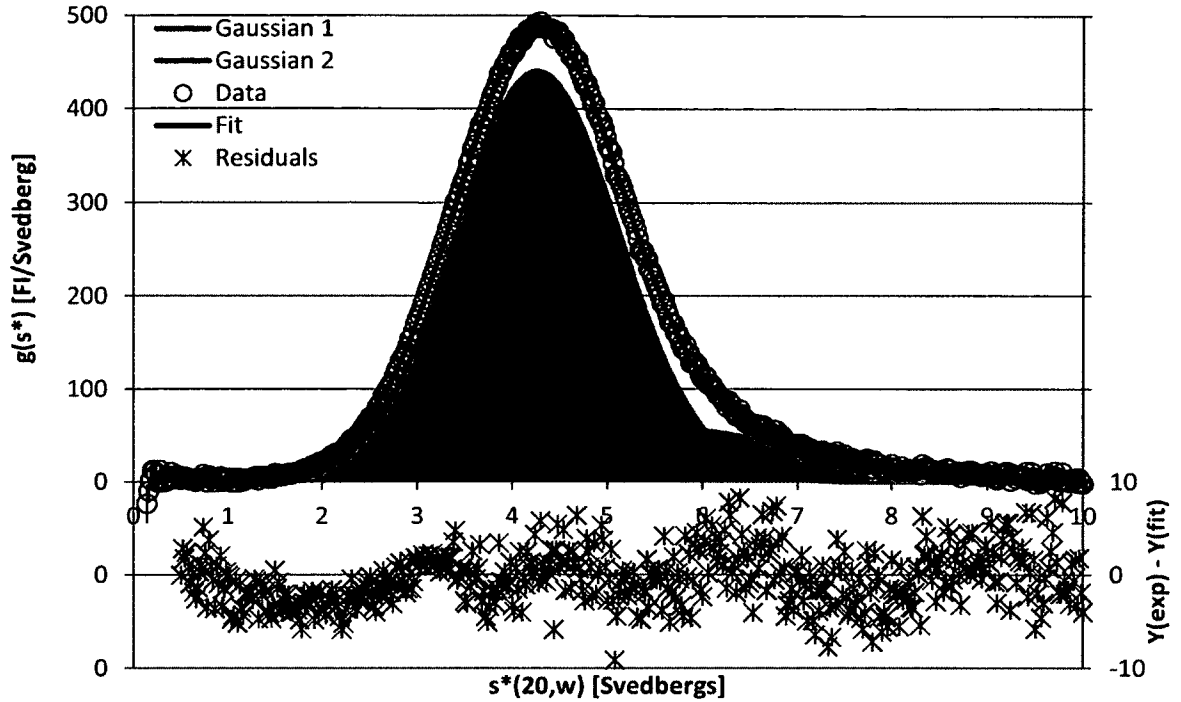


Figure 22. **40 nM Alexa-HSA in PBS.** A  $g(s)$  plot from a sedimentation velocity experiment. On the primary axis is plotted the experimental data (Data), and putative plots for all Gaussians, with the area under the curve colored to indicate which portions of the total signal they can account for. Also on the primary axis is the proposed fit to the data. Residuals are plotted on the secondary axis. Data were acquired with the fluorescence detection system.

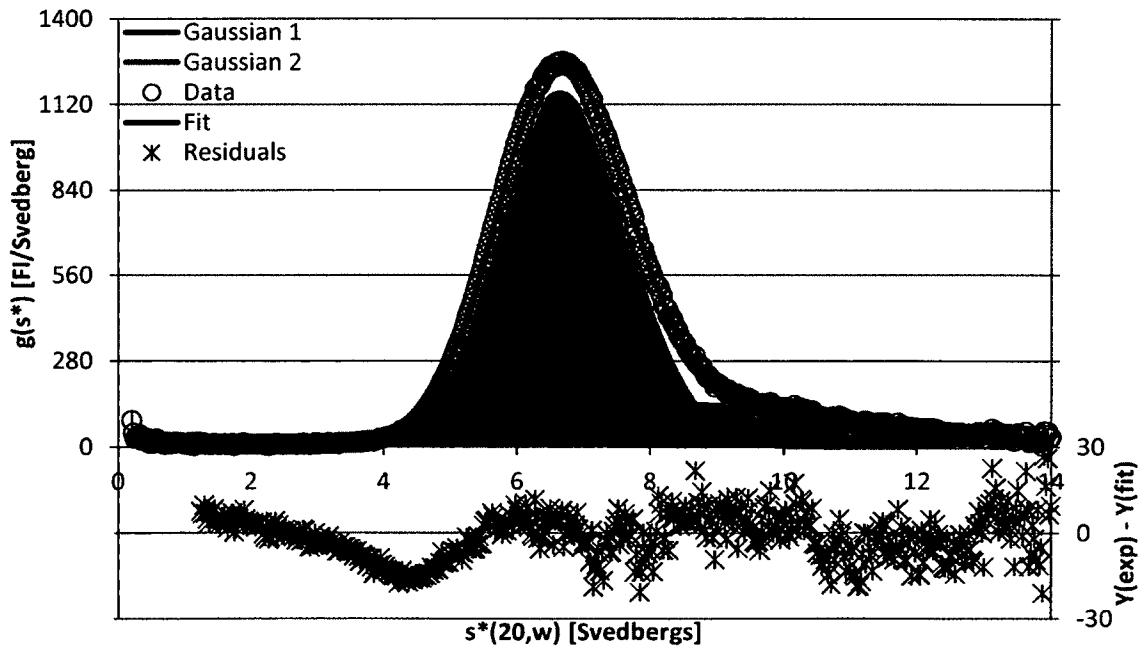


Figure 23. **40 nM Alexa-IgG in PBS.** A  $g(s)$  plot from a sedimentation velocity experiment. Data were acquired with the fluorescence detection system.



To control for the autofluorescence of human serum, human serum was run in the absence of GFP. The result can be seen in Figure 24. There is a main peak sedimenting at slightly lower than 4 s, in addition to a small peak at 2 s. It has been hypothesized elsewhere that the larger peak at 4 s represents some amount of serum albumin that has bound an autofluorescent serum component such as bilirubin (Wolfbeis and Leiner, 1985). The 2 s peak may be conjugated bilirubin, present at low concentrations in the blood stream (Juniper, 2004), or it may be some other complex.

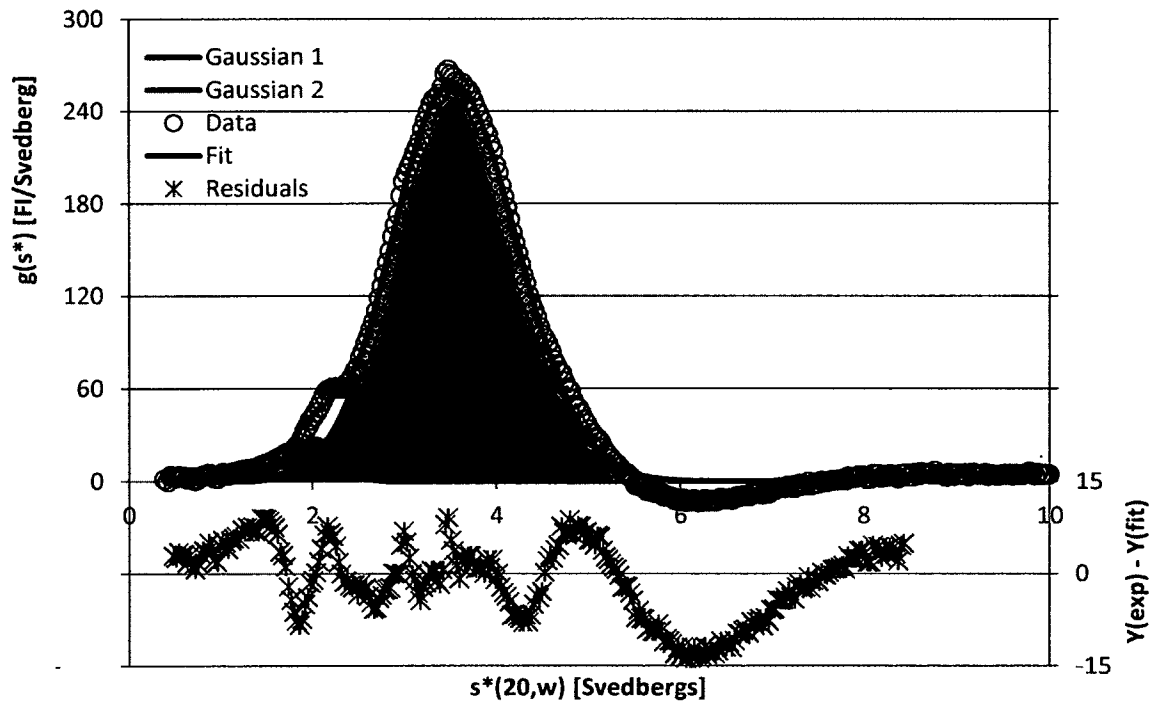


Figure 24. **Autofluorescence of serum.** A  $g(s)$  plot from a sedimentation velocity experiment run on 100 percent serum (no GFP). Data were acquired with the fluorescence detection system.

Figures 25 to 27 show the results of HSA, IgG, and GFP analyzed in 25% serum. The results for 40 nM labeled human serum albumin (HSA) shows a peak shape that is somewhat skewed toward lower  $s$ . There was no skewing of the labeled HSA that was

seen in PBS (Figure 22). The main HSA peak was found to run at about 4.5 s, which is slightly faster than is observed in PBS. It is possible that the conversion from  $s$  to  $s(20,w)$  may be inaccurate in the case of serum because the density and viscosity exhibited by serum is the result of complex mixtures that unmix over the course of the experiment. Results for 40 nM labeled IgG run in 25 percent serum are shown in Figure 26. Apart from a small peak at  $\sim 4.9$  s, most likely the autofluorescent serum component seen in Figure 24, and a broad zone sedimenting faster the main peak, possibly labeled IgG interacting non-specifically with other serum components, the main IgG peak ran at  $\sim 7.2$  s, somewhat faster than labeled IgG in buffer, which ran at  $\sim 6.5$  s (see Figure 23). The difference in  $s(20,w)$  could be a result of an inaccuracy in the density and viscosity correction, or it may be the consequence of a non-specific interaction.

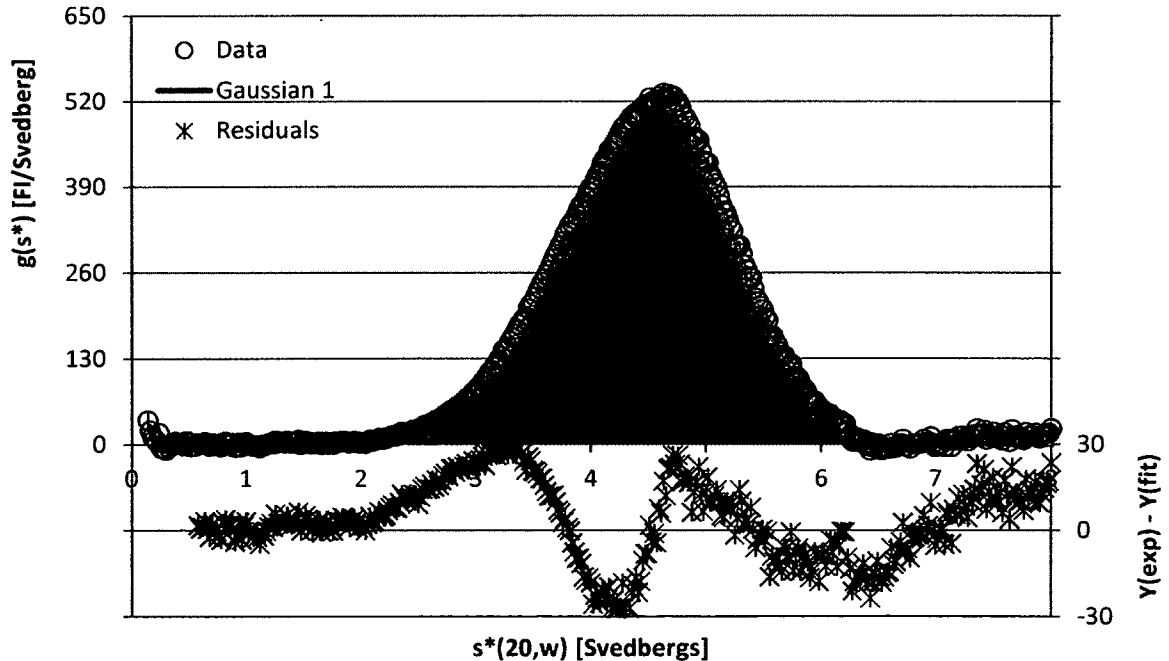


Figure 25. 40 nM Alexa-HSA in 25% serum. A  $g(s)$  plot from a sedimentation velocity experiment. On the primary axis is plotted the experimental data (Data), and a putative plot for the Gaussian that represents the proposed fit to the data, with the area under the curve colored to indicate which portions of the total signal it can account for. Residuals are plotted on the secondary axis. Data were acquired with the fluorescence detection system.

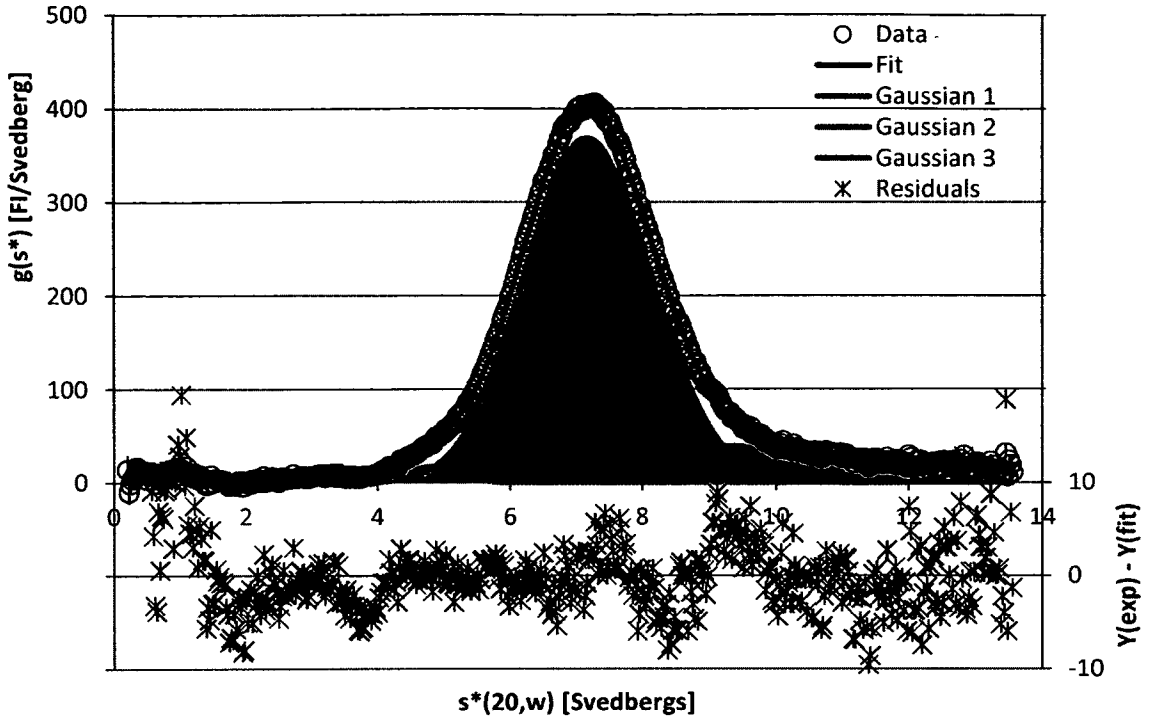


Figure 26. 40 nM Alexa-IgG in 25% serum. A  $g(s)$  plot from a sedimentation velocity experiment. Data were acquired with the fluorescence detection system.

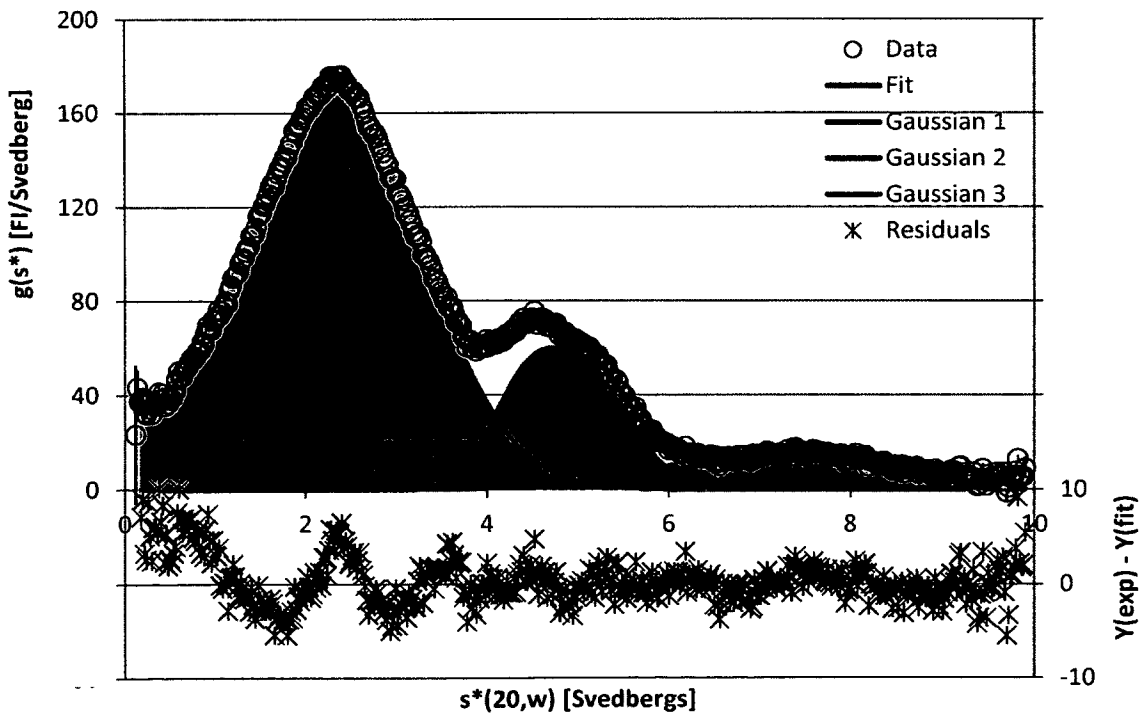


Figure 27. 40 nM GFP in 25% serum. A  $g(s)$  plot from a sedimentation velocity experiment. Data were acquired with the fluorescence detection system.

Figure 27 shows the results of 40 nM GFP run in 25 percent serum. There are three peaks, the first running at  $\sim 2.5$  s and fitting to a molecular weight around 30 kDa, exactly what would be expected of free GFP. There is an additional peak running at  $\sim 4.8$  s. Though this 4.8 s material sediments where the autofluorescent serum component is observed (Figure 24), it is moving faster than this material. This peak is an example of a distortion that can occur in complex solutions, the Johnston-Ogston (J-O) effect (Soda et. al., 1967), in which the sedimentation of a molecule is retarded by other sedimenting species. This J-O effect can cause hyper sloping of boundaries and areas of negative  $g(s)$ . The last peak is perhaps a bit surprising, a broad peak running at about 7.2 s, the same position as the labeled IgG in serum, suggesting that the GFP may bind to serum antibodies. However, the broadness of the peak argues against a specific interaction. It is more likely a nonspecific interaction between GFP and serum components.

The results of GFP, labeled HSA, and labeled IgG sedimented in 50 percent serum are displayed in Figures 28, 29, and 30. As before, labeled HSA and labeled IgG were run in 50 percent serum, the results of which are shown in a Figures 28 and 29. The results look very similar to the results in 25 percent serum. In the IgG control (Figure 29), both the autofluorescent component and the peak representing nonspecific interaction between IgG and serum components increased in concentration, as would be expected for a mass action equilibrium. Figure 30 shows the results for GFP run in 50 percent serum. Apart from poorer fit, due in part to a stronger Johnston-Ogston effect, the results look very similar to those in 25 percent serum; only the relative amount of signal in the peaks has changed. In particular, the amount of free GFP has decreased and the

amount of signal in both the 4.8 s and ~7 s peaks has increased. While the former is due in part to an increase in the concentration of the autofluorescent serum component, it is also possible that this peak is a result of increased J-O effects.

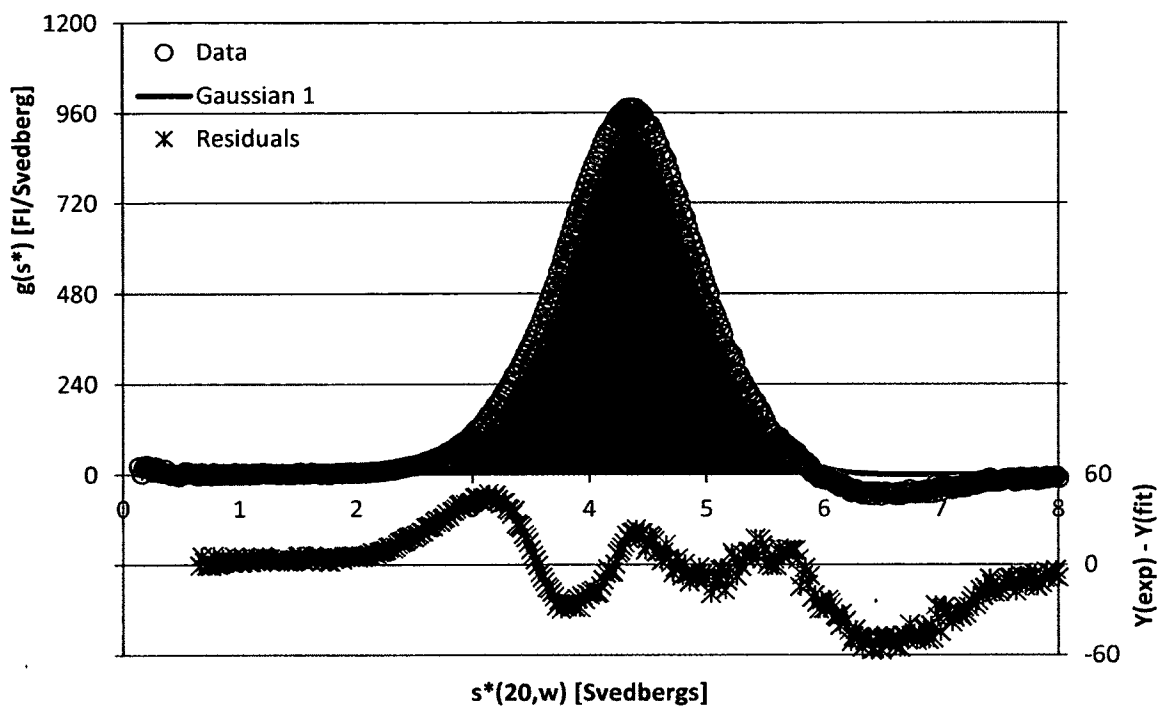


Figure 28. 40 nM Alexa-HSA in 50% serum. Data were acquired with the fluorescence detection system.

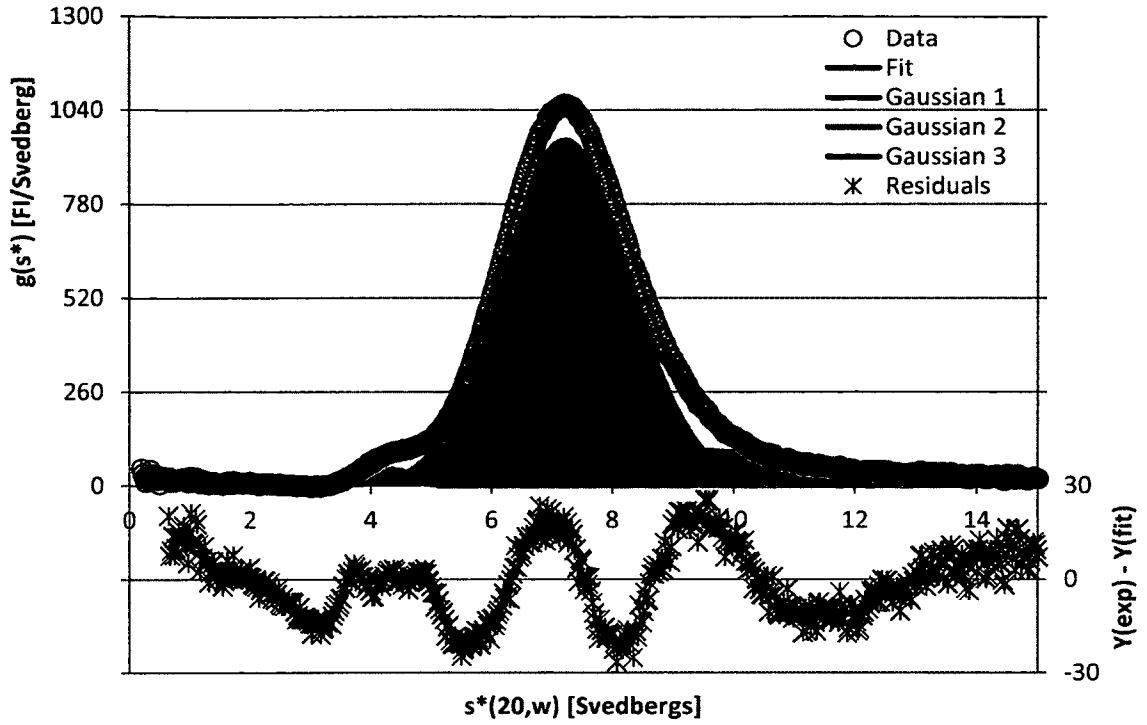


Figure 29. 40 nM Alexa-IgG in 50% serum. A  $g(s)$  plot from a sedimentation velocity experiment. Data were acquired with the fluorescence detection system.

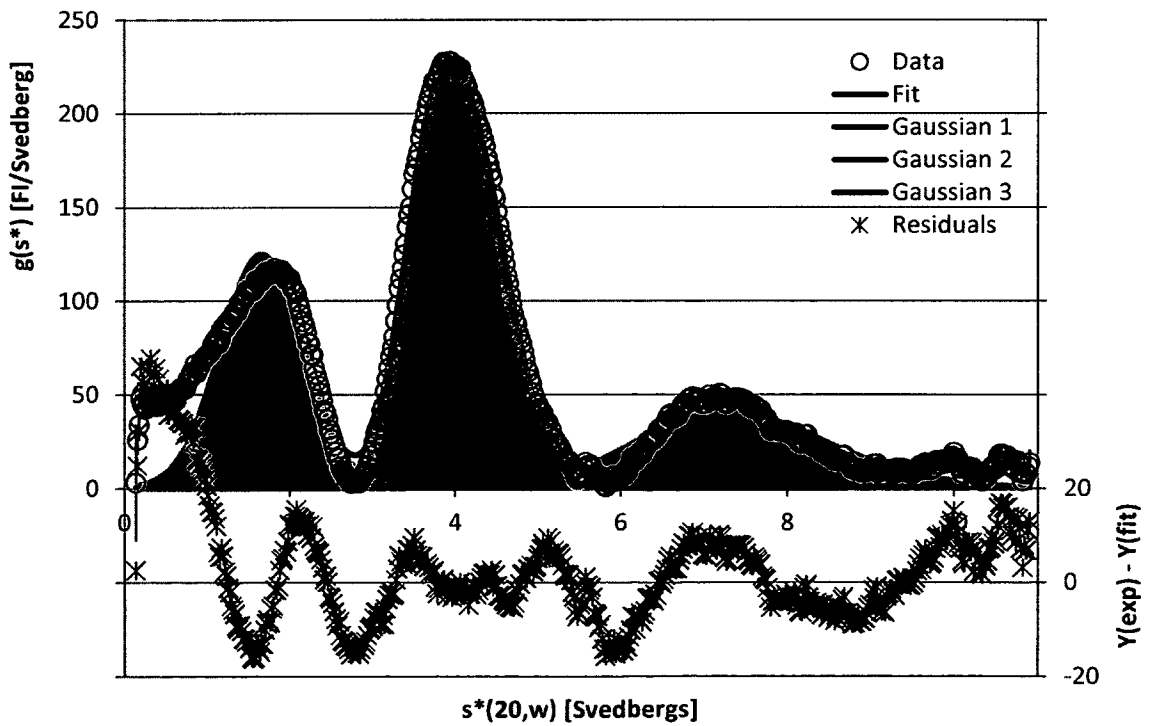


Figure 30. 40 nM GFP in 50% serum. A  $g(s)$  plot from a sedimentation velocity experiment. Data were acquired with the fluorescence detection system.

The results for GFP, labeled HSA, and labeled IgG sedimented in 75 percent serum are displayed in Figures 31, 32, and 33. Figures 31 and 32 show labeled HSA and labeled IgG respectively run in 75 percent serum. The results look very similar to the previous serum experiments. Again, In the IgG control (Figure 32), both the autofluorescent component and the peak representing nonspecific interaction between IgG and serum components increased in concentration. Figure 33 shows the results of GFP run in 75 percent serum. While the results are similar to those seen in 50 percent serum, the Johnston-Ogston effect is more severe, and again the pattern is seen where the amount of signal in the free GFP has dropped as the concentration of serum has increased, there are other differences as well. The 7 s material has disappeared, and the peak that was earlier attributed to HSA binding bilirubin and GFP has split into two peaks. The smaller of the two split peaks sedimented at  $\sim 3.4$  s, while the larger sediments at  $\sim 4.1$  s. The absence of a  $\sim 7$  s peak could be attributed to HSA outcompeting IgG for GFP binding, or that all of the additional serum constituents disrupting the binding of IgG to GFP.

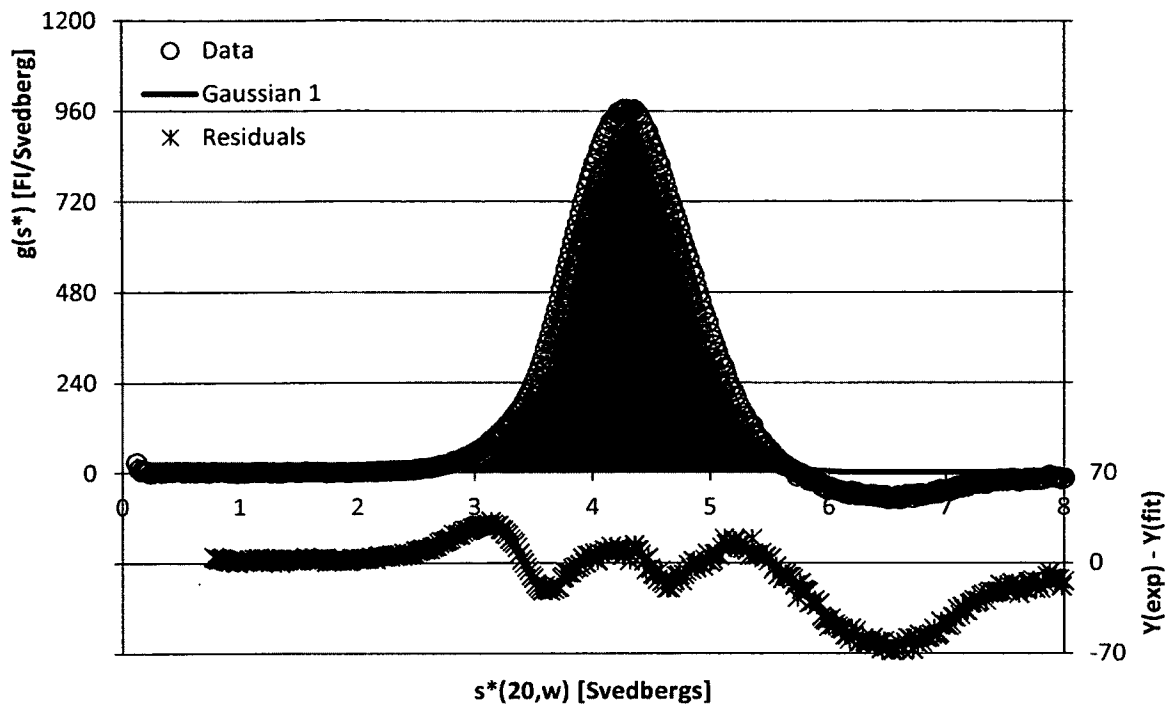


Figure 31. 40 nM Alexa-HSA in 75% serum. Data were acquired with the fluorescence detection system.

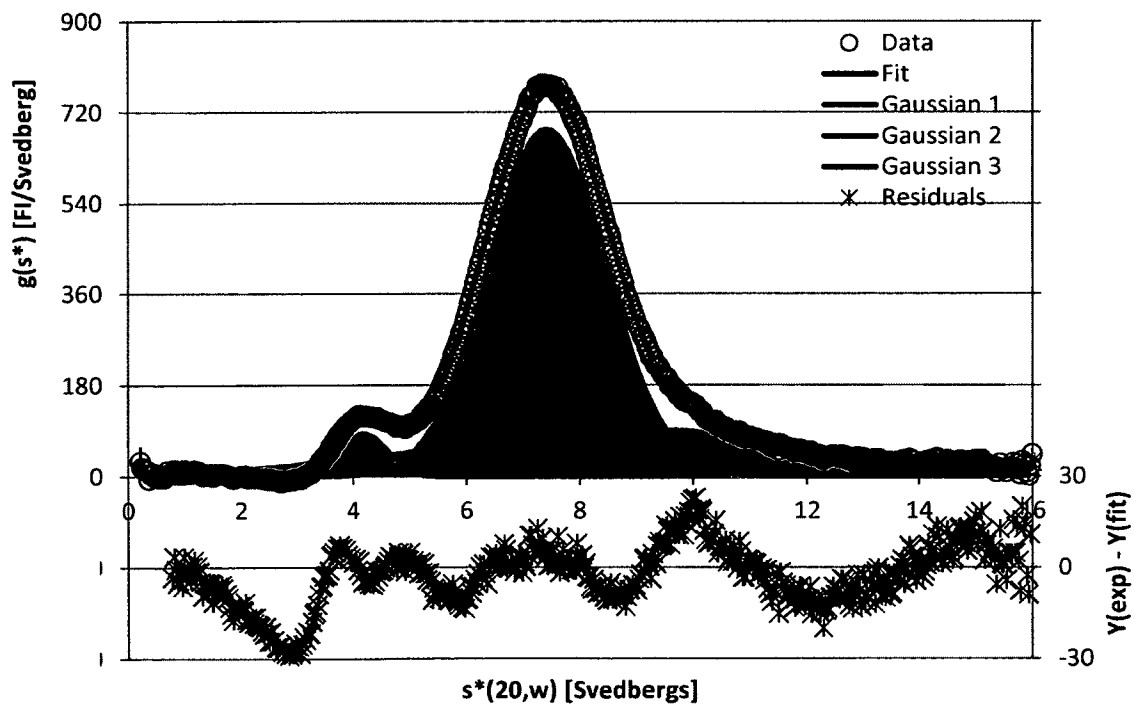


Figure 32. 40 nM Alexa-IgG in 75% serum. A  $g(s)$  plot from a sedimentation velocity experiment. Data were acquired with the fluorescence detection system.



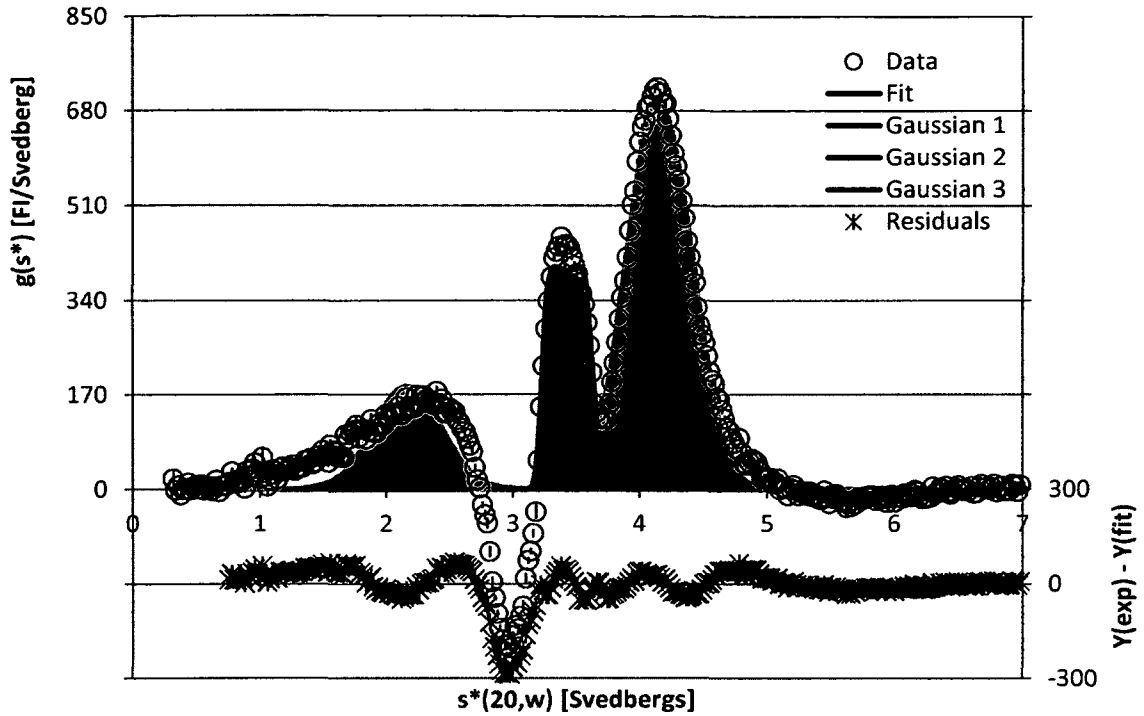


Figure 33. 40 nM GFP in 75% serum. A  $g(s)$  plot from a sedimentation velocity experiment. Data were acquired with the fluorescence detection system.

The results of GFP, labeled HSA, and labeled IgG sedimented in 99.75 percent serum are displayed in Figures 34, 35, and 36. Figures 34 and 35 show labeled HSA and labeled IgG respectively run in 99.75 percent serum. The results again look very similar to the previous experiments in 75 % serum. Yet again, in the IgG experiment (Figure 35), both the autofluorescent component and the peak representing nonspecific interaction between IgG and serum components increased in concentration.

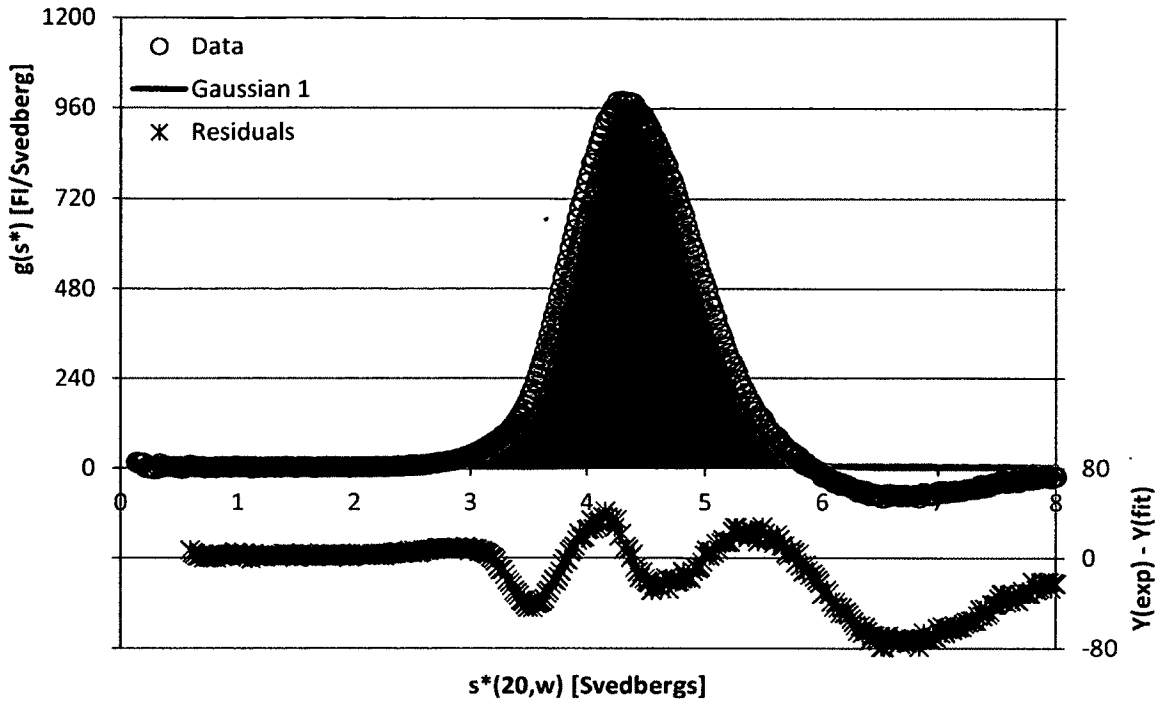


Figure 34 40 nM Alexa-HSA in 100% serum. A  $g(s)$  plot from a sedimentation velocity experiment. Data were acquired with the fluorescence detection system.

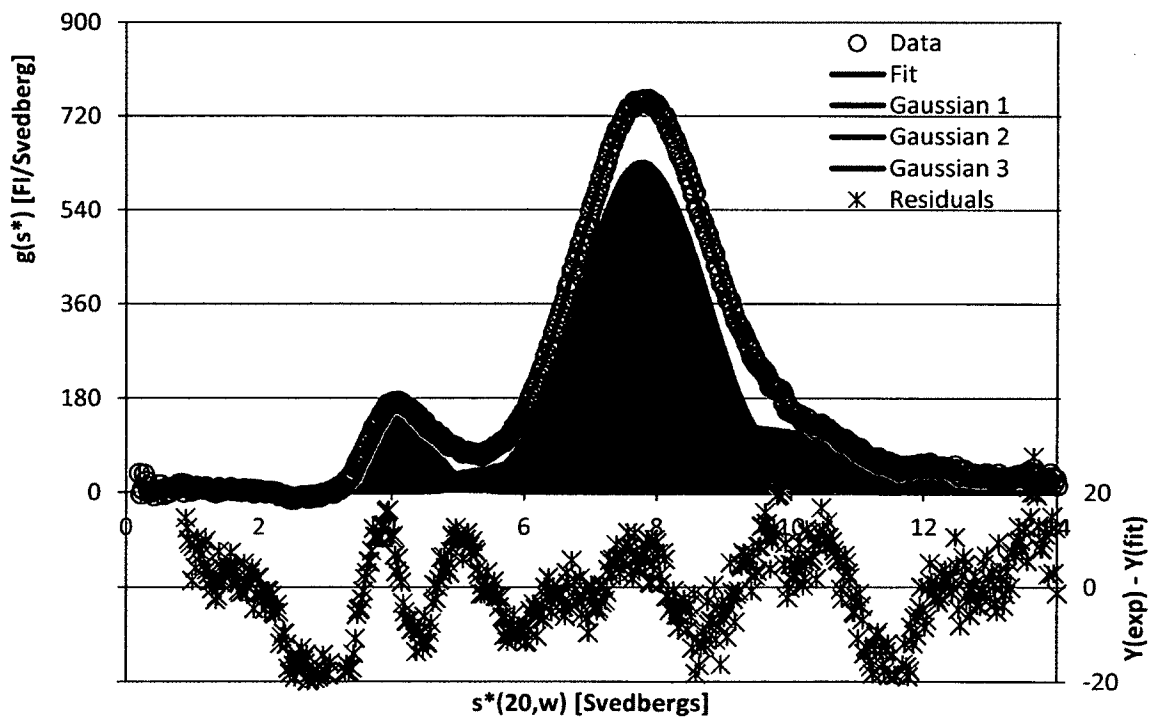


Figure 35. 40 nM Alexa-IgG in 100% serum. A  $g(s)$  plot from a sedimentation velocity experiment. Data were acquired with the fluorescence detection system.

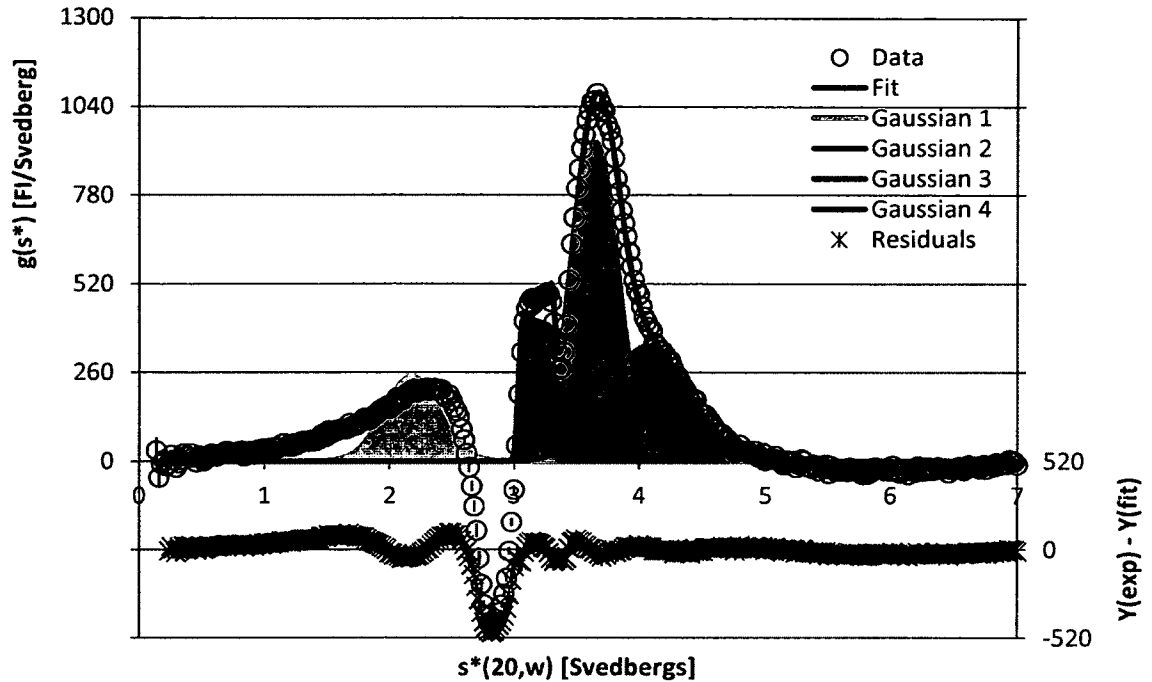


Figure 36. 40 nM GFP in 100% serum. A  $g(s^*)$  plot from a sedimentation velocity experiment. Data were acquired with the fluorescence detection system.

Figure 36 shows the results of GFP run in 99.75 percent serum. For the most part the  $g(s^*)$  distributions look very similar to the previous results. There is an extra peak running slightly faster than the peak previously hypothesized to be HSA-GFP (Figure 27). The fit in Figure 33 misses in the area immediately following this peak, so this peak may be present there as well. This extra peak at  $\sim 4.1$  s present in 99.75 percent serum could be a reaction boundary representing nonspecific interaction between GFP and a serum component or a superfluous Gaussian introduced by the software to improve the fit, it is difficult to identify true peaks in  $g(s^*)$  curves that are this complex and distorted. The only other difference is that the two putative HSA peaks have shifted to lower  $s$  values, by about 0.2 to 0.3 s, perhaps a viscosity effect not fully corrected by the  $s^*(20,w)$  correction.

A summary of the previous data from sedimentation velocity experiments of labeled HSA and IgG in serum can be seen in Figure 37, where the  $s(20,w)$  of the main peak is plotted against serum concentration. It can be seen here that the  $s(20,w)$  of HSA does not vary significantly or systematically with serum concentration, indicating that the  $s(20,w)$  correction for density and viscosity has been successful. However, in the case of IgG, it can be seen that the  $s(20,w)$  of labeled IgG tends to increase with serum concentration. Because the results with HSA indicated that the  $s(20,w)$  correction for density and viscosity was successful, the most likely explanation for this result is that IgG is interacting with a serum component, increasing the  $s$  value of the main peak.

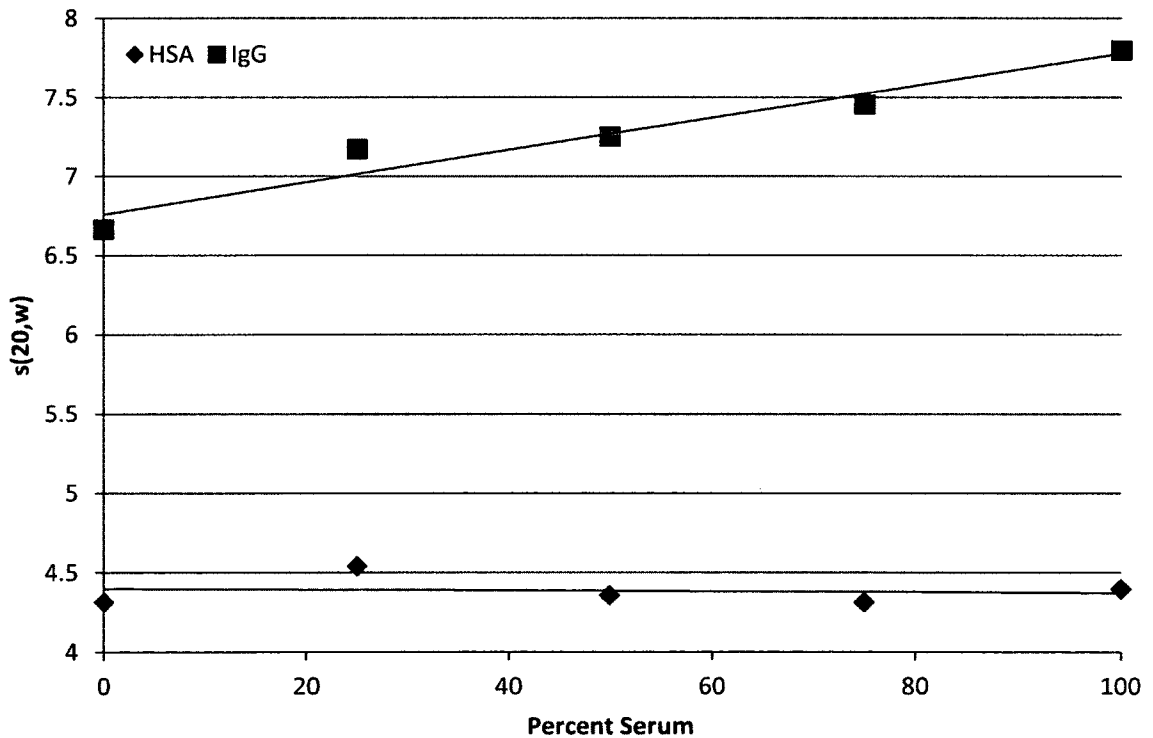


Figure 37. Results of sedimentation velocity experiments of labeled IgG and HSA in serum. The  $s(20,w)$  values (y axis) for labeled HSA and IgG at the indicated concentration of serum (x axis).

Sedimentation equilibrium experiments were conducted on 40 nM GFP in various serum concentrations. The raw data from these experiments can be seen in Figure 38. Analysis did not proceed because the data could not be fit to an exponential curve, due to bizarre artifacts such as areas, or “kinks,” where signal went down with radial position (27%, 36% and 9% serum), and inflection points (73%, 82%, 91%, and 100% serum). This effect was also seen in all of the sedimentation velocity experiments of GFP in serum, an example of the raw data from the sedimentation velocity analysis of 40 nM GFP in 100% serum is shown in Figure 39, and this low concentration region is visible towards the base of the cell.

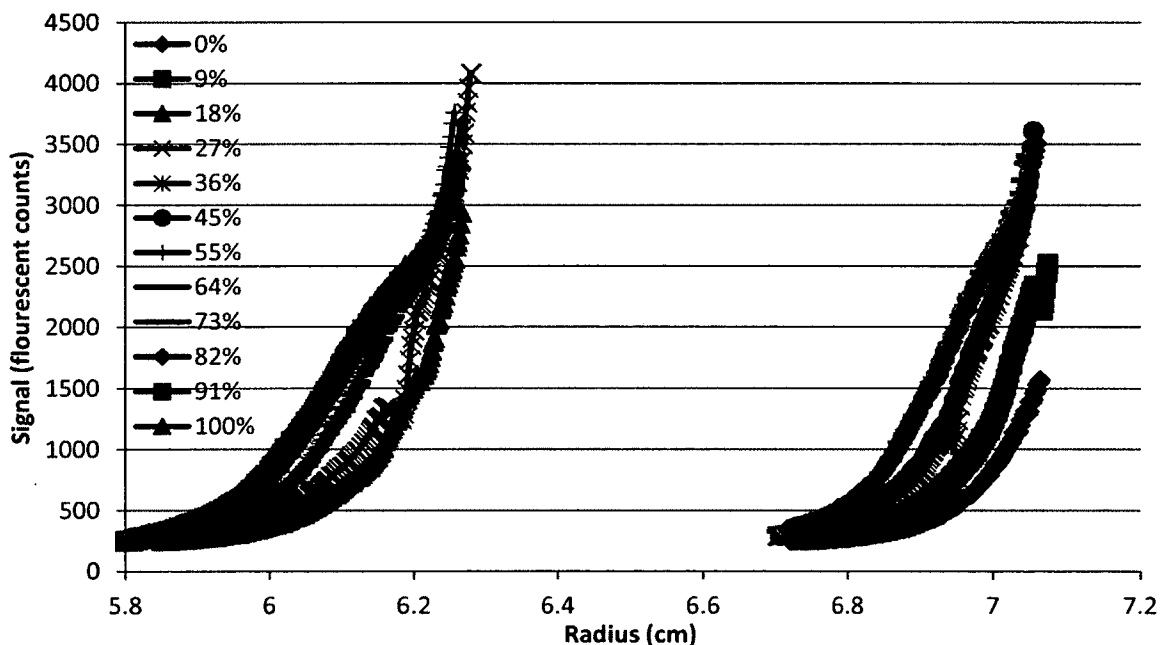


Figure 38. 40 nM GFP in serum. Raw data from a sedimentation equilibrium experiment conducted at 25K RPM. Experiment was conducted in dilutions of serum as indicated by the legend. Data were acquired with the fluorescence detection system.

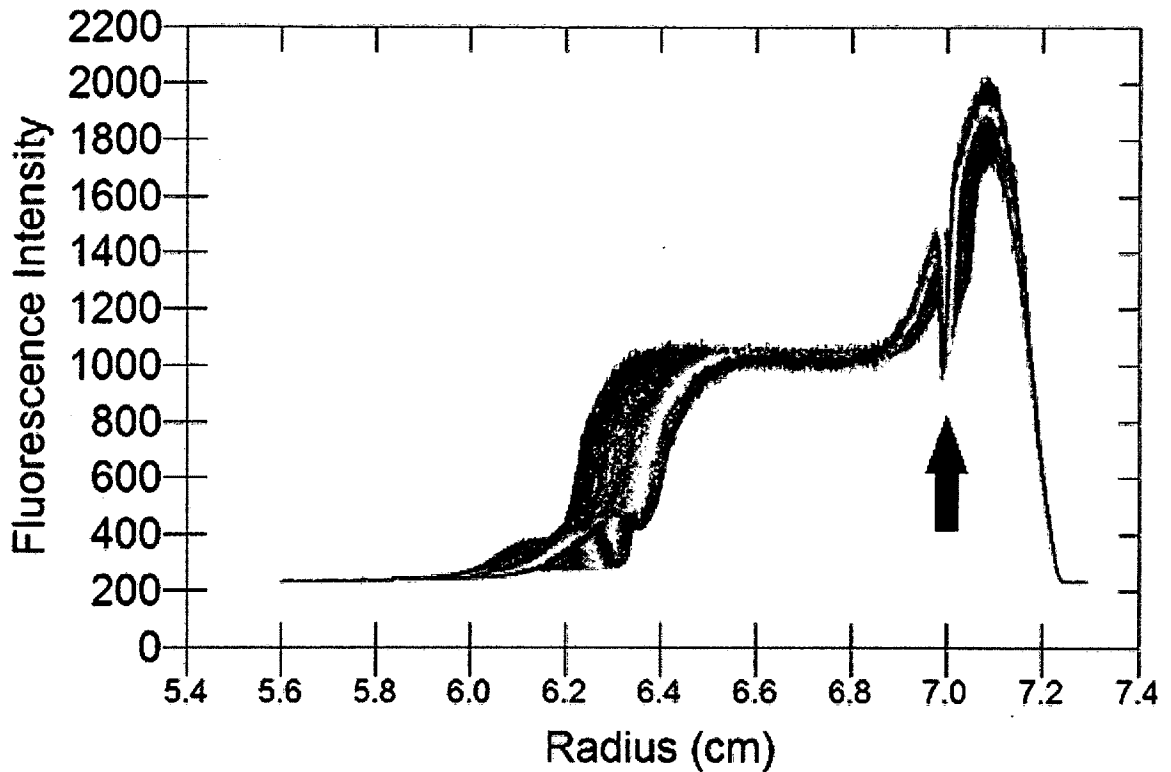


Figure 39. 40 nM GFP in 100% serum. Raw data from a sedimentation velocity experiment conducted at 45K RPM. Data were acquired with the fluorescence detection system.

The fact that the concentration dip is visible consistently in both sedimentation velocity and equilibrium data indicates that the cause has a thermodynamic origin that warrants further study. One possibility is that LDL banding may be the cause due to the density gradient that forms over the course of an experiment, the serum LDL bands at its neutral density point. To account for the data, GFP would have to be excluded from this phase, resulting in the drop in concentration. The equilibrium results, however, show that the chemical activity of GFP is very high in this region.

## CHAPTER VI

### SEDIMENTATION OF LABELED MAB 1, MAB 2, and MAB 3 IN HIGH CONCENTRATIONS OF THEMSELVES

#### Materials and Methods

##### Materials

Materials used were as described in Chapter I. Additionally, mAb 1, mAb 2, and mAb 3 were supplied by Hoffmann-La Roche, Ltd.

##### Methods

Methods used included the sedimentation equilibrium method, described in Chapter I, and the sedimentation velocity method, described in Chapter II.

Densities and Viscosities of Solutions of mAbs 1,2, and 3. Densities of the antibody solutions were measured using a Mettler/Par Precision Density Meter model DMA 02D. The viscosities of the antibody solutions were measured using an Anton Paar Automated Micro Viscometer, using a capillary of 1.6 mm diameter and a ball of 1.5 mm diameter and having a density of 7.85 g/mL.

Charge Determination of mAbs 1, 2 and 3 Via Membrane Confined Electrophoresis. Charge determinations were performed using a Spin Analytical Membrane Confined

Electrophoresis machine. The buffer used was 100 mM NaCl, 10 mM MES, and each sample was exhaustively dialyzed against this prior to the experiment. The membranes used had a molecular weight cut-off of 8,000 Da. Each antibody was loaded at a concentration of 1 g/L and run at a current of 5 mA.

Labeling of mAbs 1, 2 and 3. All mAbs were labeled as directed by Molecular Probes Alexa Flour™ 488 Protein Labeling Kit (A-10235). Moles of dye per mole of protein was less than one in all cases.

Sedimentation Velocity of Labeled mAbs 1, 2, and 3 in High Concentrations of Themselves. Sedimentation velocity experiments were performed at 20°C in 100 mM NaCl, 10 mM MES, pH 6.0. Data were collected at a rotor speed of 45, 000 RPM in two sector charcoal-filled epon centerpieces, either Spin Analytical SEDVEL60K or Beckman, with either quartz or sapphire windows and in an An60 Ti 4-hole rotor. Experiments were conducted by adding either 1.6 µL of a 24 µM stock solution of labeled mAb 1, 1.5 µL of a 32 µM stock solution of labeled mAb 2, or 1 µL of a 48 µM stock solution of labeled mAb 3 to 400 µL of a concentration series of mAb 1, 2 or 3 (from 0 to 72 g/L for mAb 1, from 0 to 80 g/L for mAb 2, and from 0 to 100 g/L for mAb 3), resulting in a final labeled mAb concentration of 120 nM. All stock solutions were dialyzed (1:100) against 100 mM NaCl, 10 mM MES, pH 6, changing the buffer two times at a 4 hour interval and once before dialyzing overnight.

The data were analyzed using the DCDT+ software version 2.3.2 (John S. Philo). A partial specific volume of 0.73 mL/g was used for all mAbs. The solution densities and viscosities used were shown below (Figures 40 and 41).



Sedimentation Equilibrium of Labeled mAbs 1, 2, and 3 in High Concentrations of Themselves. Sedimentation equilibrium experiments were performed at 20°C in 100 mM NaCl, 10 mM MES, pH 6.0. Data were collected at rotor speeds of 8,000 and 12,000 RPM in 4-sector Spin Analytical centerpieces with either quartz or sapphire windows and in an An60 Ti 4-hole rotor. Experiments were conducted by adding either 1.6  $\mu$ L of a 24  $\mu$ M stock solution of labeled mAb 1, 1.5  $\mu$ L of a 32  $\mu$ M stock solution of labeled mAb 2, or 1  $\mu$ L of a 48  $\mu$ M stock solution of labeled mAb 3 to 400  $\mu$ L of a concentration series of mAb 1, 2 or 3 (from 0 to 50 g/L for all mAbs), resulting in a final labeled mAb concentration of 120 nM. All stock solutions were dialyzed (1:100) against 100 mM NaCl, 10 mM MES, pH 6, changing the buffer two times at a 4 hour interval and once before dialyzing overnight.

Data were analyzed using the HeteroAnalysis software version 1.1.44 (James L. Cole, Jeffrey W. Lary). The single ideal species model was used, with a partial specific volume of 0.73 mL/g and the densities of solutions shown below (Figure 40). The apparent molecular weight reported by the software for each background concentration was averaged over the 2 rotor speeds. Any fit where systematic residuals were observed was refit to a monomer-nmer model, where both the apparent stoichiometry (n) and the  $\ln K$  of the association were fit for, averaged over the 2 rotor speeds, and reported.

Sedimentation Equilibrium in Low Salt Conditions of Labeled mAbs 1, 2, and 3 in High Concentrations of Themselves. Sedimentation equilibrium experiments were performed as described above, except all stock solutions were dialyzed (1:100) against 10 mM NaCl,

10 mM MES, pH 6, changing the buffer two times at a 4 hour interval and once before dialyzing overnight.

Sedimentation Velocity of Labeled mAbs 1, 2, and 3 in Serum. Serum dilutions were made using PBS. Sedimentation velocity experiments were conducted as described above.

## Results

### Densities and Viscosities of Solutions of mAb 1,2, and 3

The densities of all mAbs increased linearly with concentration (Figure 40) as expected (all had  $R^2$  greater than 0.999 when fit by linear least squares). The viscosities of mAbs 2 and 3 increased quite sharply with concentration (Figure 41), with mAb 2 increasing the most sharply. The mAb seen to increase the least in viscosity with concentration was mAb 1.

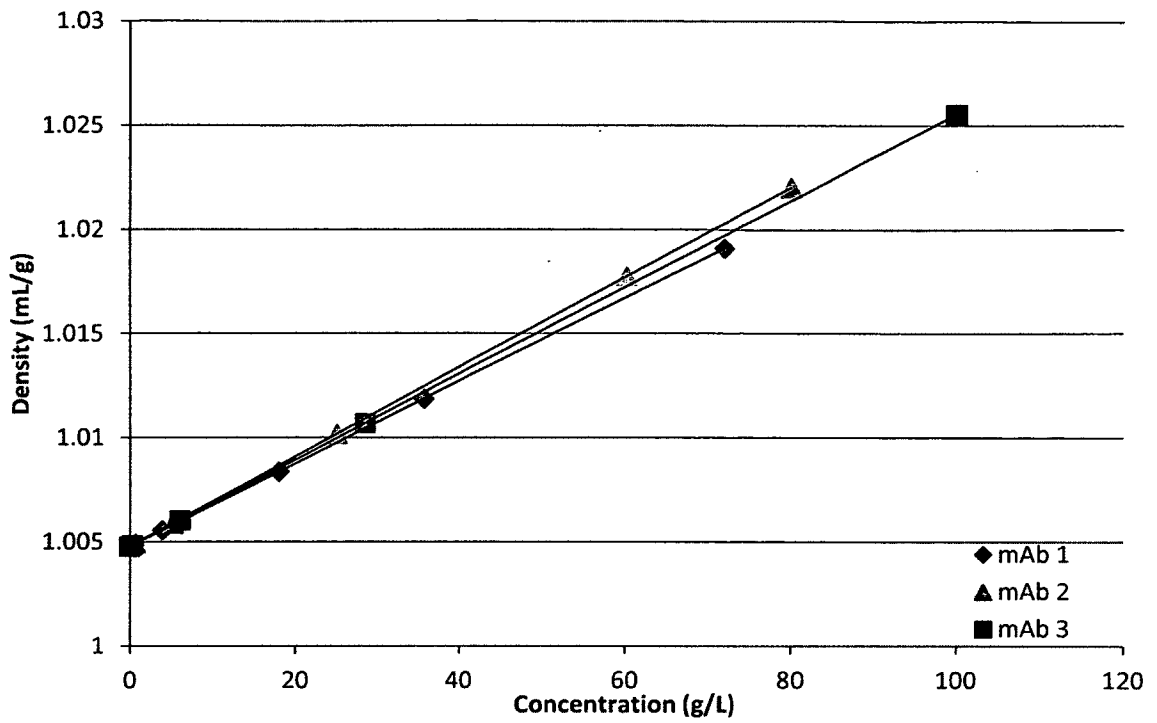


Figure 40. Densities of mAb 1, 2, and 3 as a function of concentration.

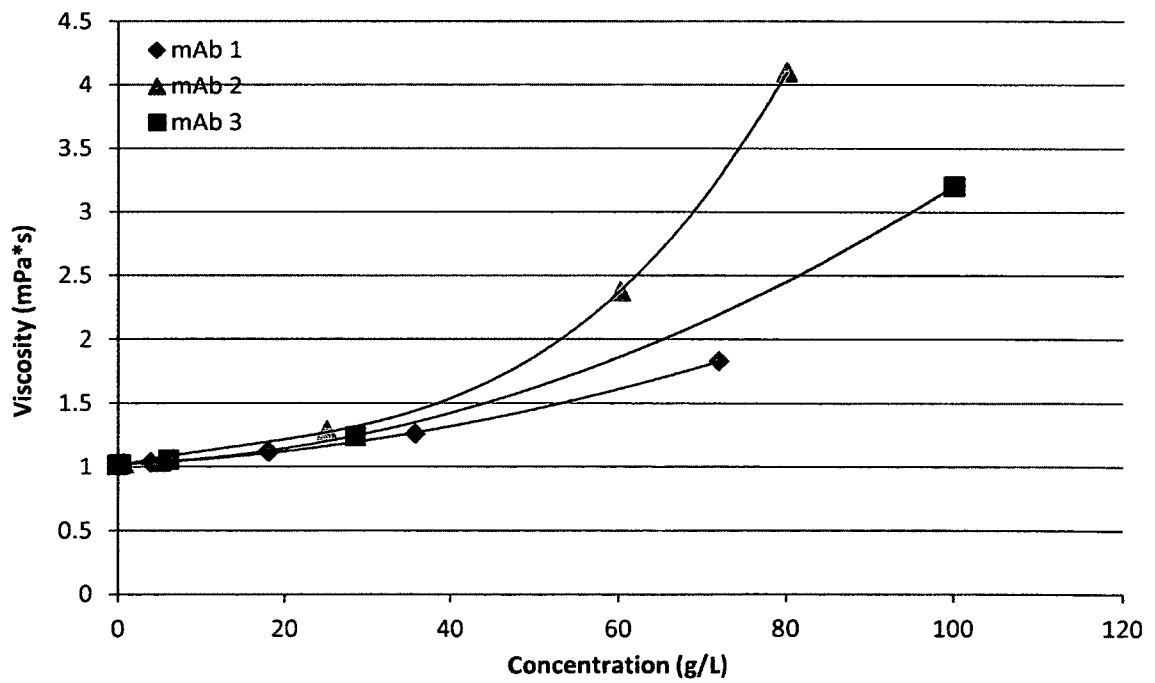


Figure 41. Viscosities of mAb 1, 2 and 3 as a function of concentration.

### Charge Determination of mAbs 1, 2 and 3 Via Membrane Confined Electrophoresis

Salt Concentration (mM)	mAb 1	mAb 2	mAb 3
100	0	0	0
10	7.4	2.3	*

Table 2. Charges of mAb 1, 2, and 3. Charge determination was performed via membrane confined electrophoresis by Dana I. Filoti

Charge determination was performed by Dana I. Filoti via membrane confined electrophoresis. The value marked with an (\*) indicates that the data had a very odd distribution due to the solution gelling upon application of current, preventing an accurate measurement of charge.

### Sedimentation Velocity of Labeled mAb 1, 2, and 3 in High Concentrations of Themselves

MAb 1. MAb 1 seemed to be relatively well behaved in these experiments. For the most part it ran between 6.5 and 7.3 s (Figures 42 – 47), about what would be expected of an antibody monomer. The only exception is at 72 g/L (Figure 47), where mAb 1 ran at 9.15 s. 9.15 s(20,w) is close to as fast as a dimer of a 6.5 s(20,w) protein would be expected to sediment (a ratio of 1.45 is expected). Additionally, starting at 1 g/L, increasing concentrations of mAb 1 can be seen to sediment at slightly higher s values (Figures 48 and 49). This is consistent with mAb 1 slightly self-associating under these conditions. The sedimentation equilibrium experiments below will give a clearer picture regarding the self-association of mAb 1.

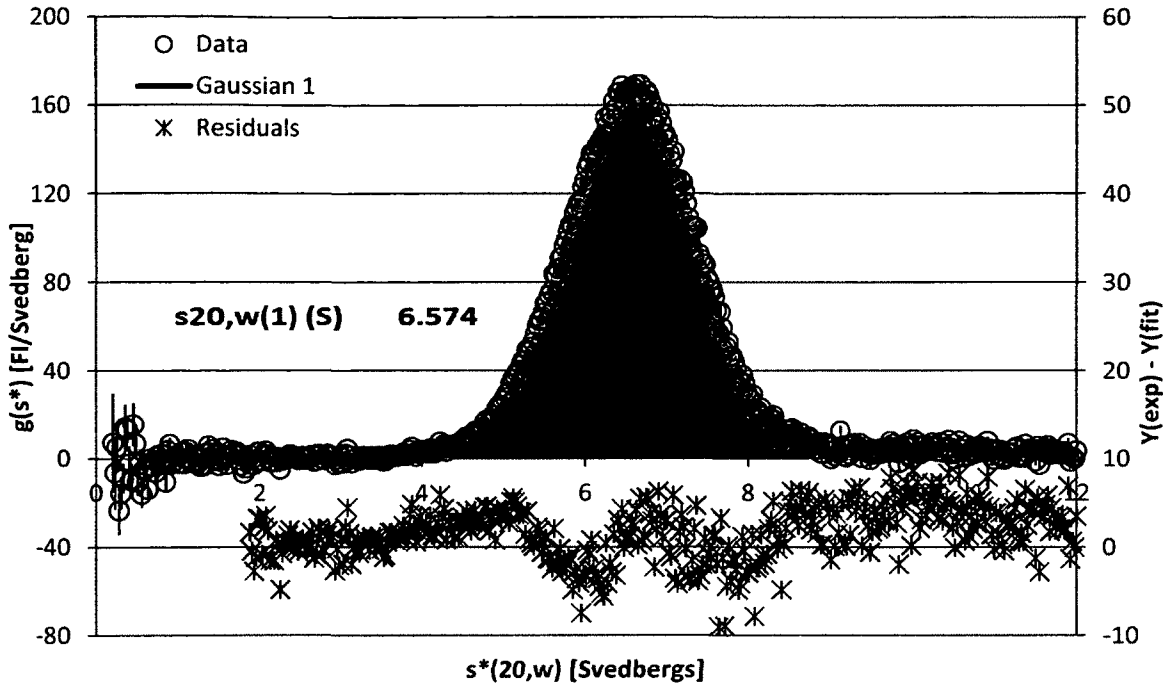


Figure 42. 120 nM Alexa-mAb 1 in 100 mM NaCl, 10 mM MES. A  $g(s)$  plot from a sedimentation velocity experiment. Data were acquired with the fluorescence detection system.

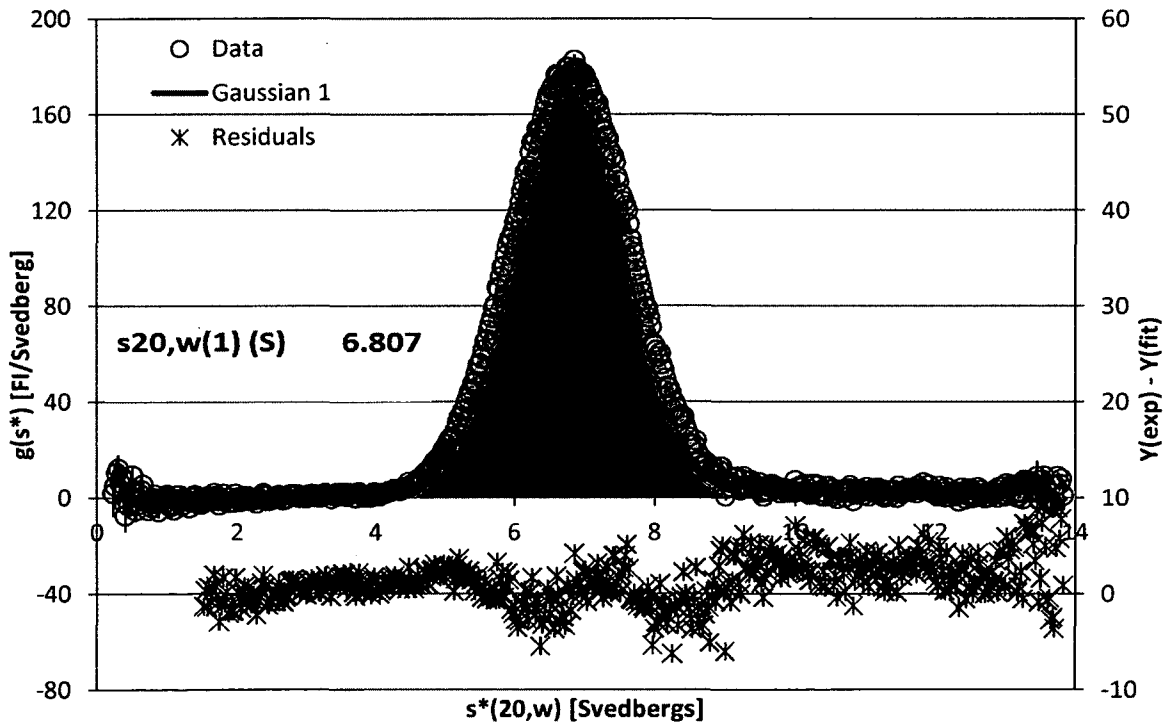


Figure 43. 120 nM Alexa- mAb 1 in 0.5 g/L mAb 1. A  $g(s)$  plot from a sedimentation velocity experiment. Data were acquired with the fluorescence detection system.

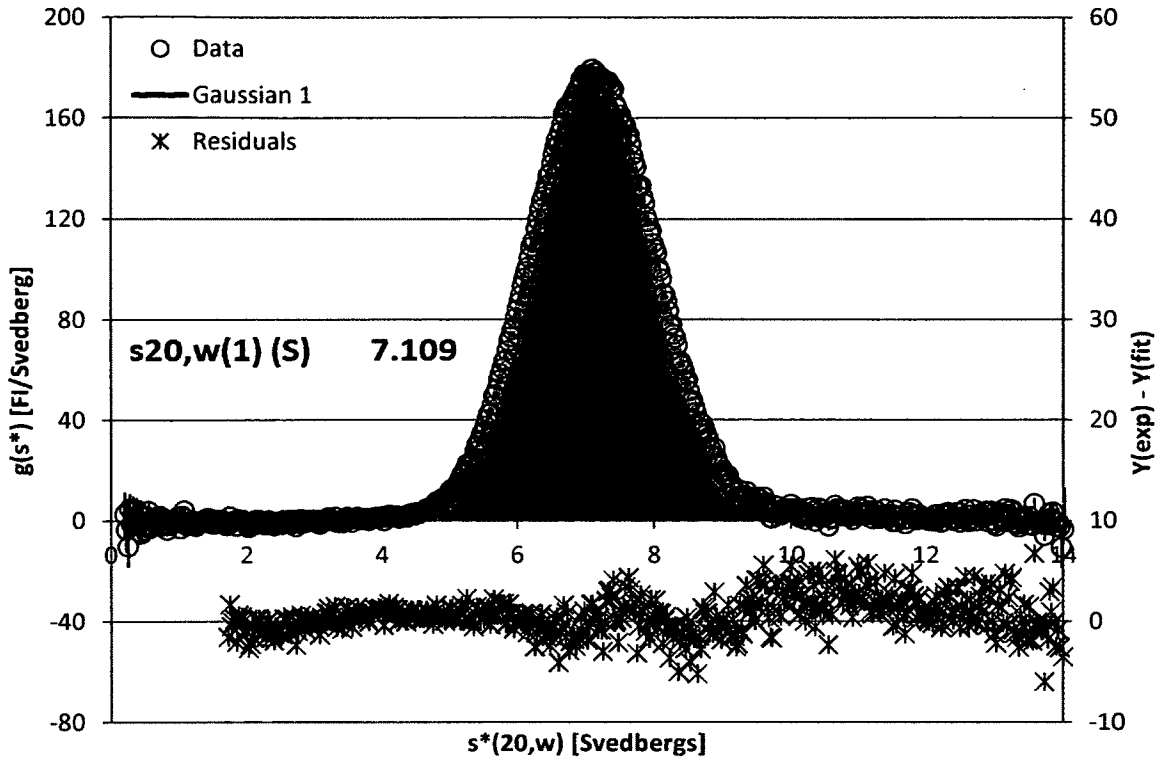


Figure 44. 120 nM Alexa- mAb 1 in 5 g/L mAb 1. A  $g(s)$  plot from a sedimentation velocity experiment. Data were acquired with the fluorescence detection system.

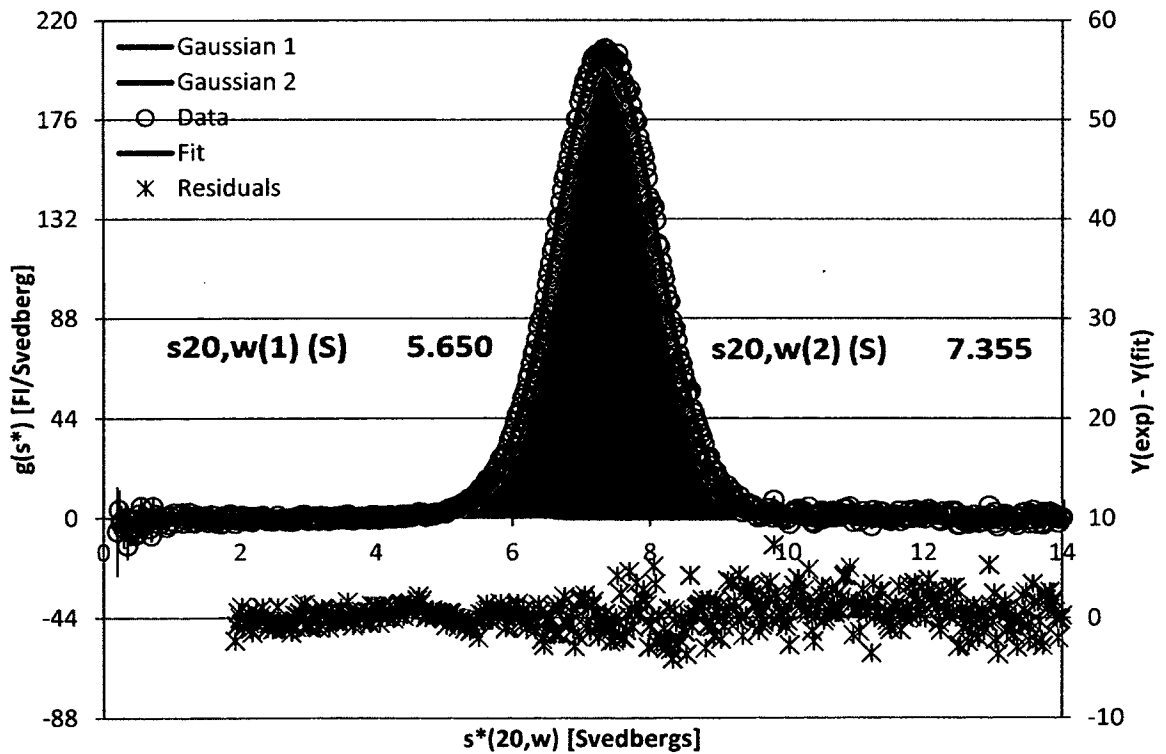


Figure 45. 120 nM Alexa- mAb 1 in 20 g/L mAb 1. A  $g(s)$  plot from a sedimentation velocity experiment. Data were acquired with the fluorescence detection system.

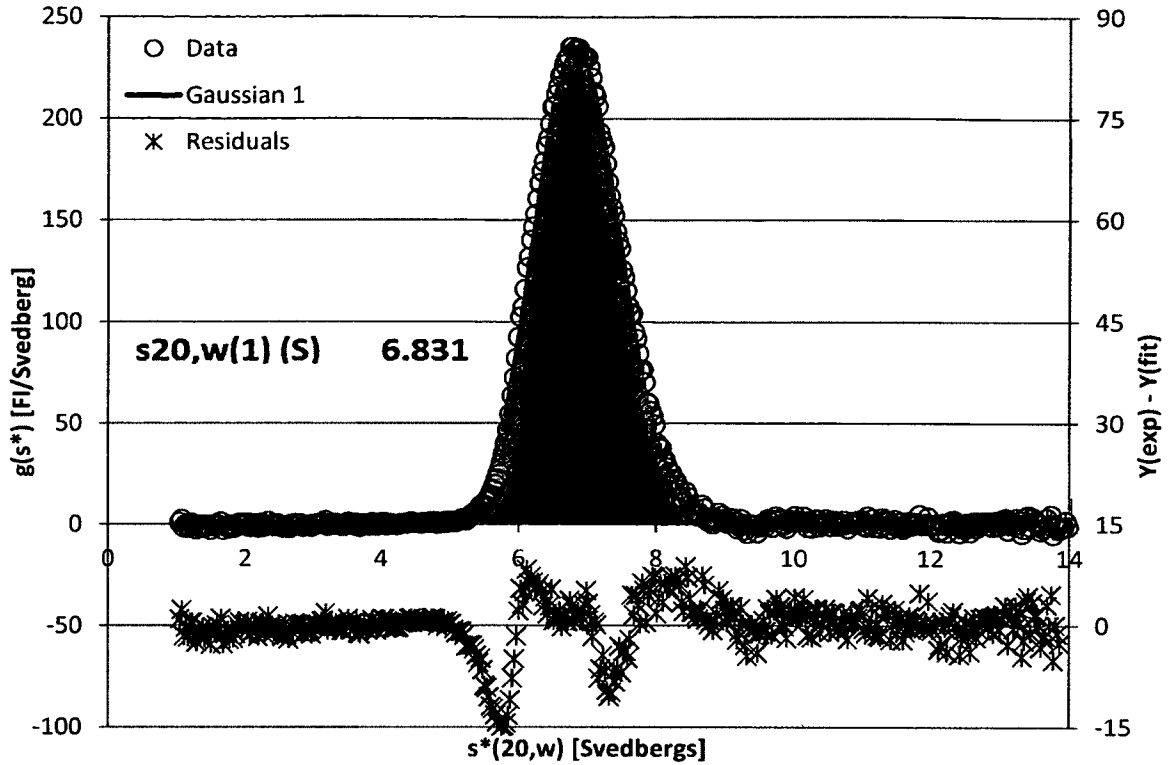


Figure 46. 120 nM Alexa- mAb 1 in 35 g/L mAb 1. A  $g(s)$  plot from a sedimentation velocity experiment. Data were acquired with the fluorescence detection system.

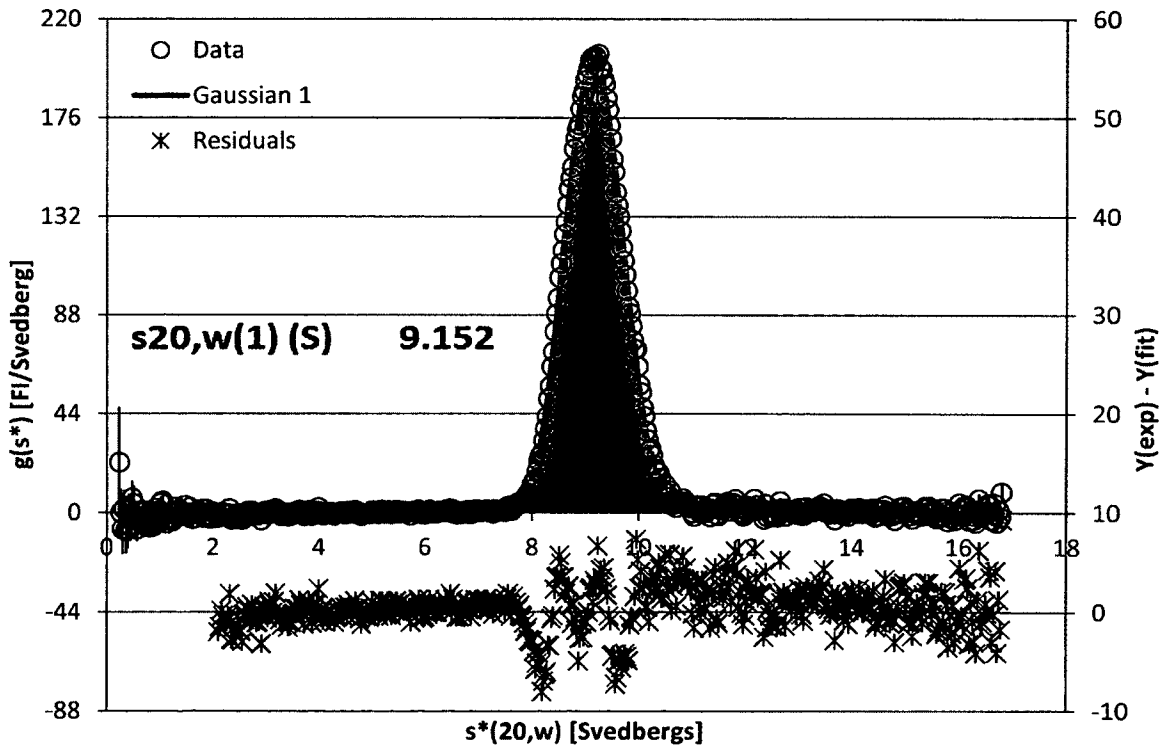


Figure 47. 120 nM Alexa- mAb 1 in 72 g/L mAb 1. A  $g(s)$  plot from a sedimentation velocity experiment. Data were acquired with the fluorescence detection system.

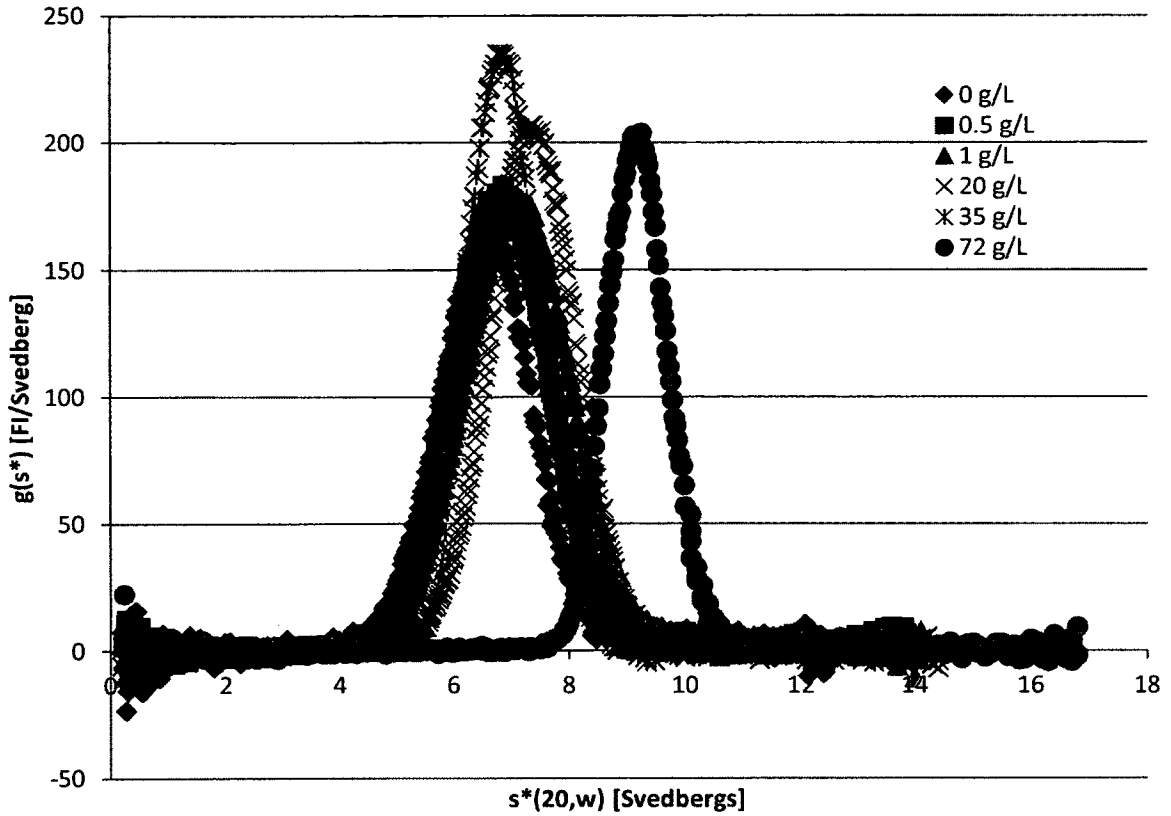


Figure 48. 120 nM Alexa-mAb1 in mAb 1. Graph shows  $g(s)$  plots for a series of sedimentation velocity experiments in the concentration of mAb 1 indicated by the legend. Data were acquired using the Fluorescence detection system.

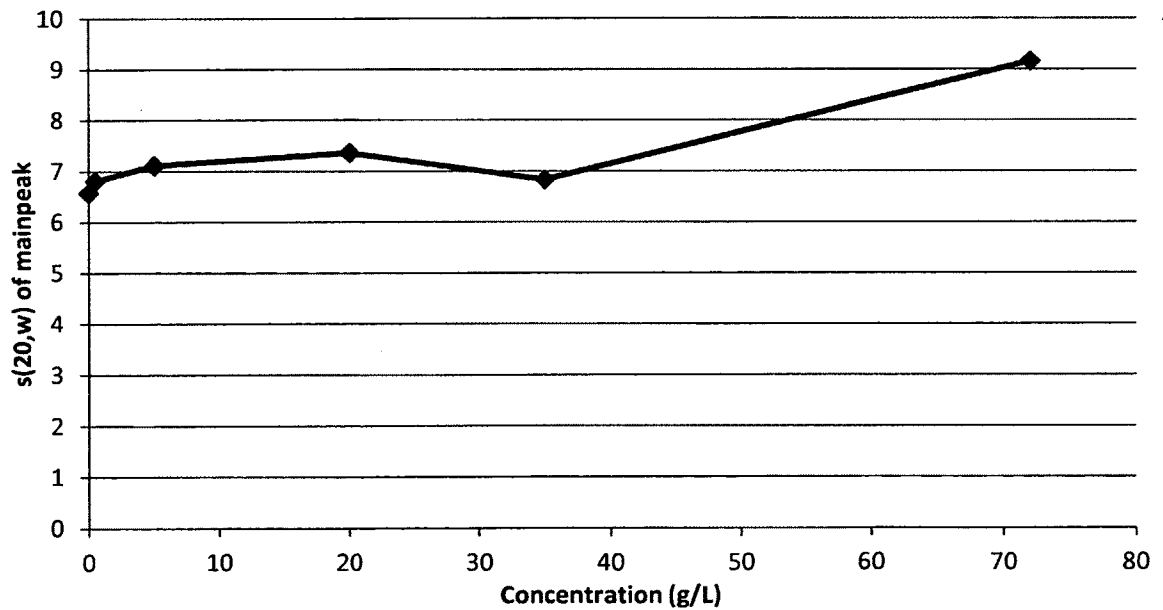


Figure 49. Results of sedimentation velocity experiments of labeled mAb 1 in the indicated concentration of mAb 1 (x axis).



Unfortunately, under conditions of high viscosity fitting the width of the peak to a molecular weight is not very useful, because this relies on being able to fit to the diffusional coefficient. The force of sedimentation that is applied to create the concentration gradient will also create a gradient in the viscosity. Therefore, when a molecule diffuses down the concentration gradient it will be diffusing into an area of lower viscosity, will sediment faster in this area of lower viscosity, and catch back up. This effect will tend to create very sharp boundaries in the raw data (see Figure 50 below), which will tend to make the g(s) peaks thinner than expected, and therefore fit to unrealistically high molecular weights.

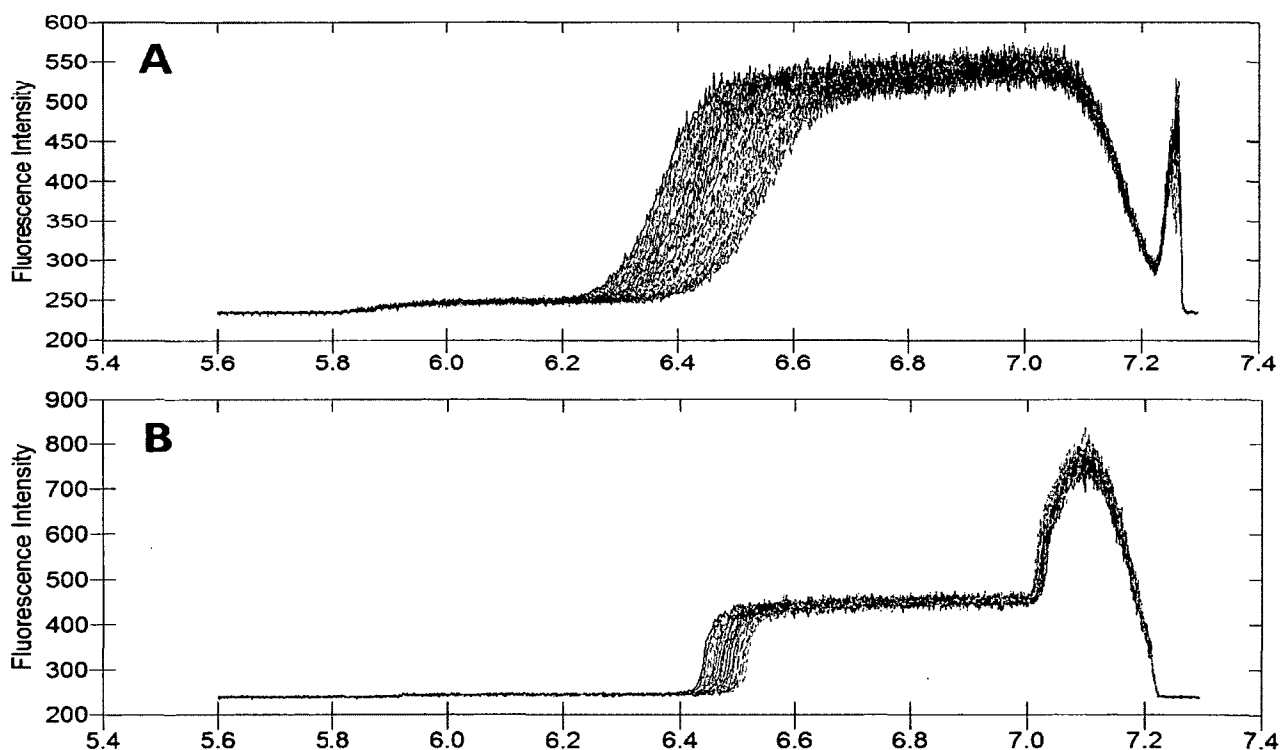


Figure 50. Examples of the raw data from a sedimentation experiment of mAb 1 in a low concentration, low viscosity solution (A, Buffer) and a high concentration, high viscosity solution (B, 200 g/L mAb 1).

**MAb 2.** At 0 to 5 g/L mAb 2 (Figures 51 – 53), 120 nM Alexa-mAb 2 fits to a single peak, however the  $s(20,w)$  value of that peak steadily increases with concentration, which is evidence of self-association. At 25 g/L (Figure 54) this hypothesis is confirmed, indicated by the main peak running at 12.3 s, about what would be expected of a linear tetramer of a 6.3 s(20,w) protein. There is also evidence of lower order associations, a peak at 8.3 s(20,w) is about what would be expected of a dimer of a 6.3 s(20,w) protein. However this peak could also be a reaction boundary between tetramer and lower order associations or monomer.

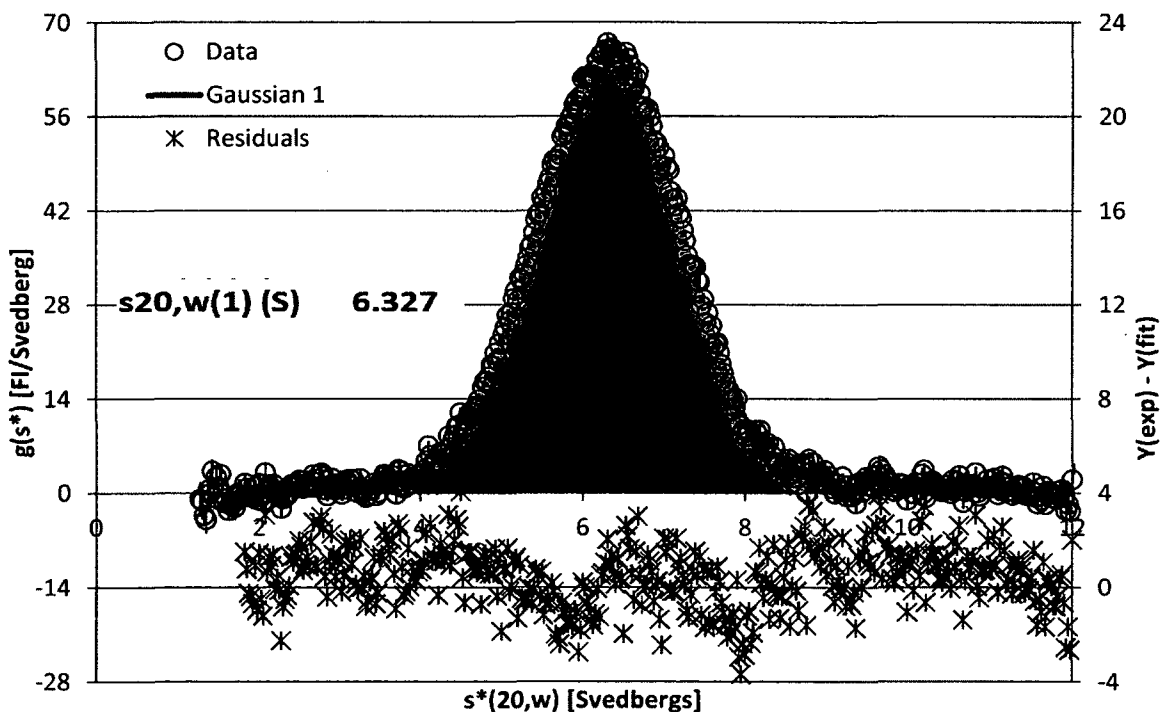


Figure 51. 120 nM Alexa-mAb 2 in 100 mM NaCl, 10 mM MES. A  $g(s)$  plot from a sedimentation velocity experiment. Data were acquired with the fluorescence detection system.

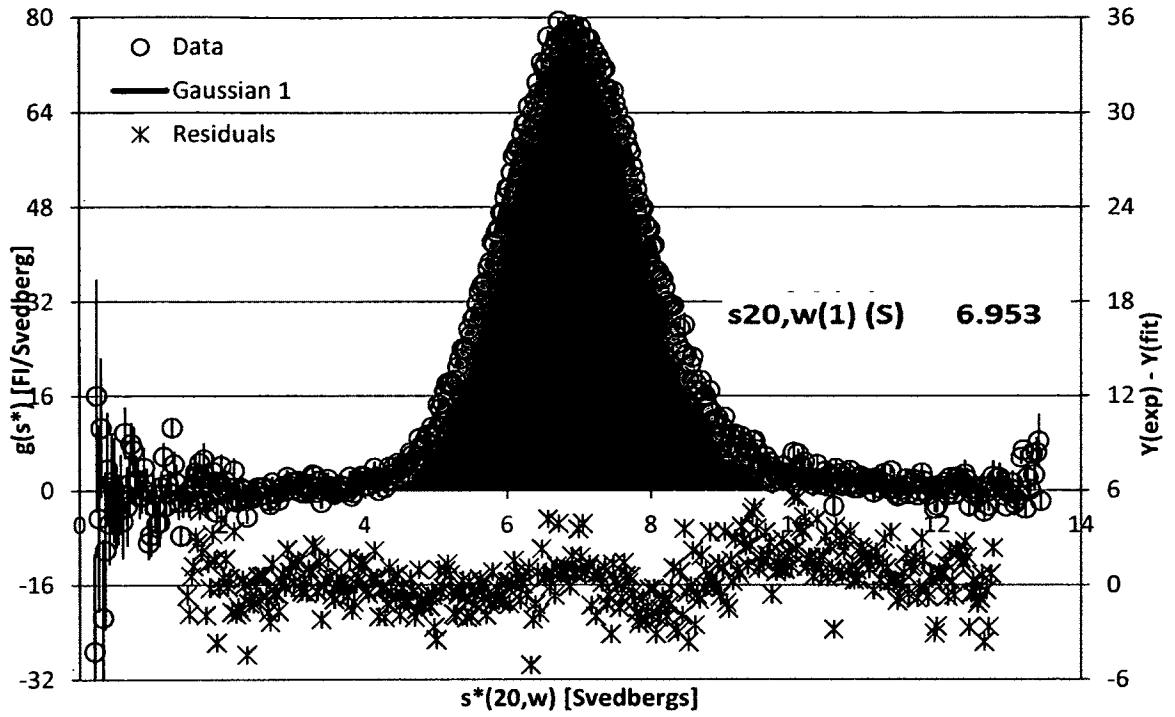


Figure 52. 120 nM Alexa-mAb 2 in 0.5 g/L mAb 2. A  $g(s)$  plot from a sedimentation velocity experiment. Data were acquired with the fluorescence detection system.

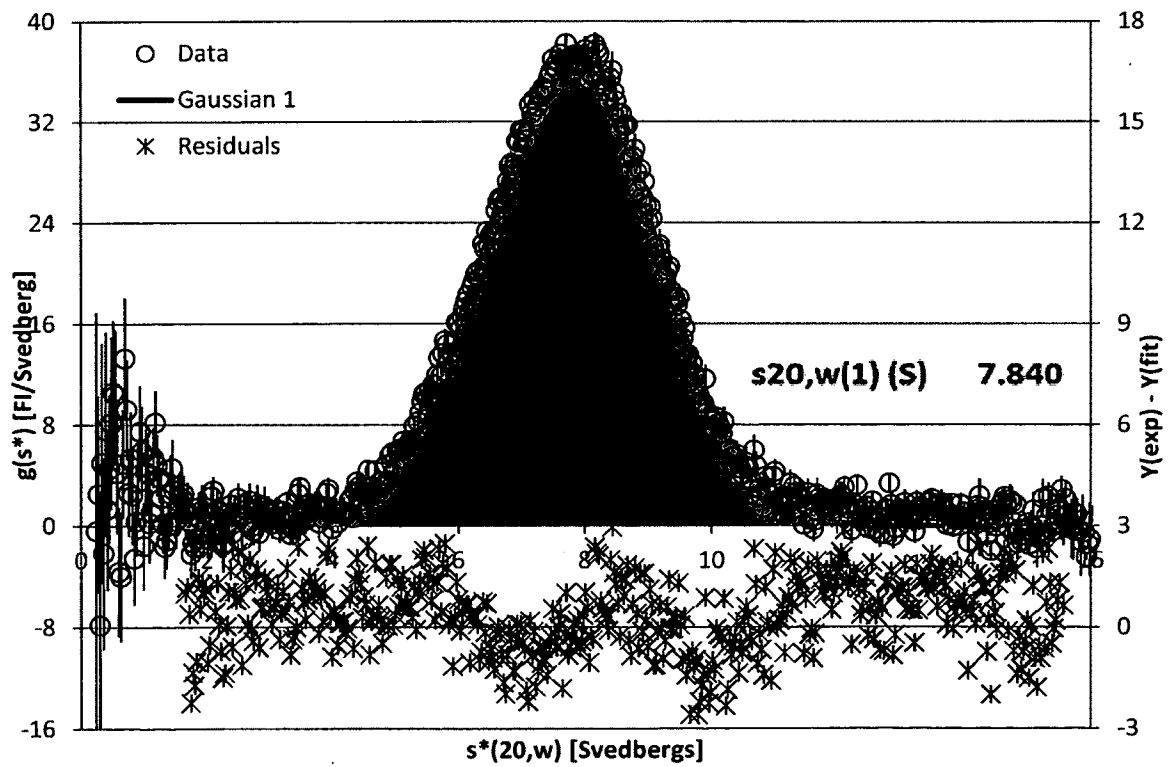


Figure 53. 120 nM Alexa-mAb 2 in 5 g/L mAb 2. A  $g(s)$  plot from a sedimentation velocity experiment. Data were acquired with the fluorescence detection system.

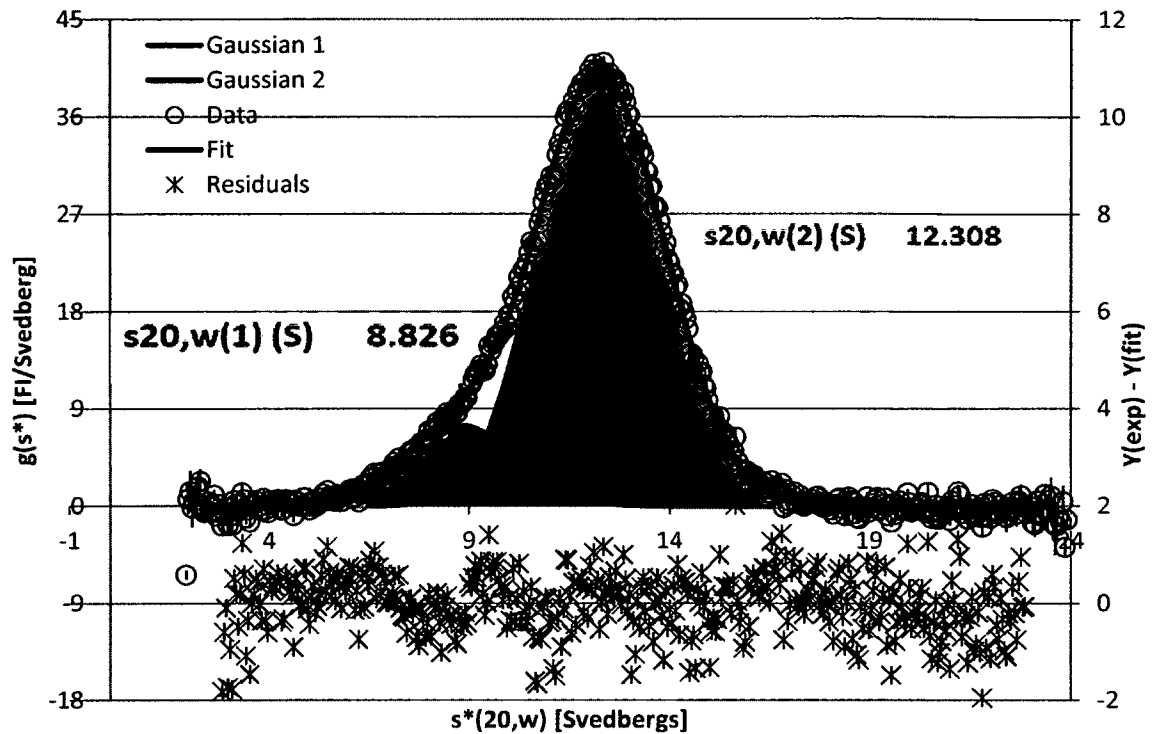


Figure 54. 120 nM Alexa-mAb 2 in 25 g/L mAb 2. A  $g(s)$  plot from a sedimentation velocity experiment. Data were acquired with the fluorescence detection system.

In the 60 g/L mAb 2 experimental condition (Figure 55) the main peak ran at about 15.27  $s(20,w)$ , evidence of a higher order association than tetramer. There is evidence of even higher order associations due to material sedimenting at  $s(20,w)$  values higher than 15.27  $s(20,w)$ . There is also evidence of lower order associations due to a peak at 13.2  $s(20,w)$ , but again, this could also be a reaction boundary.

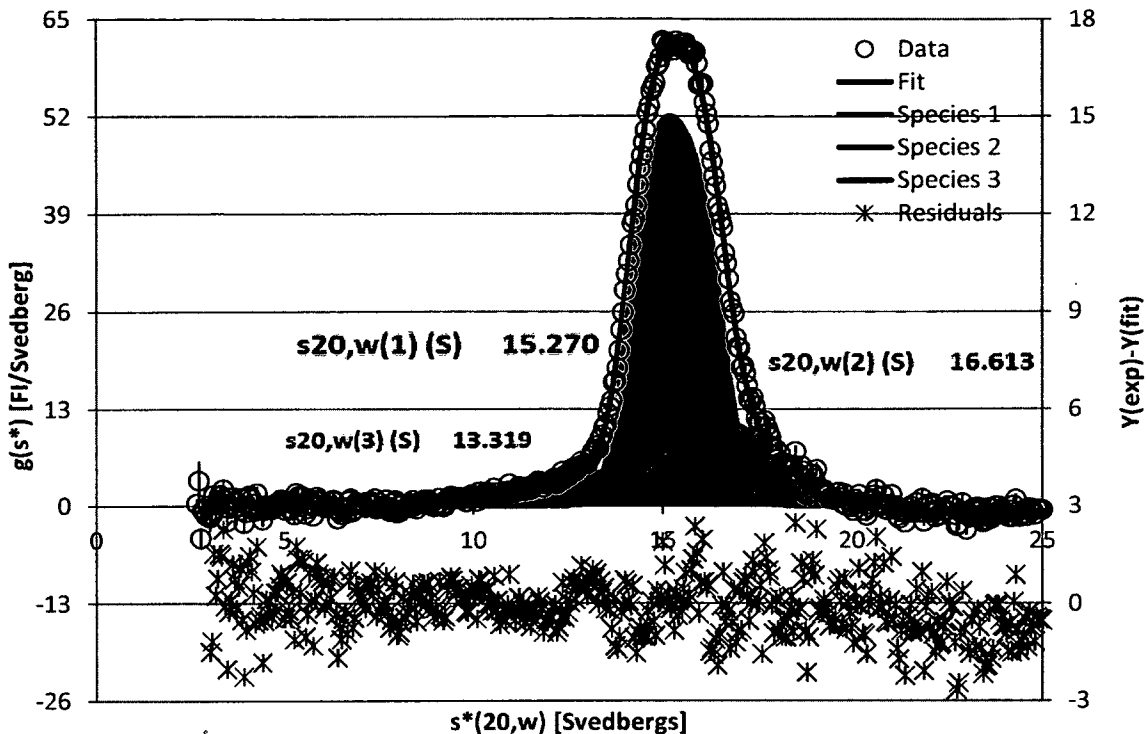


Figure 55. 120 nM Alexa-mAb 2 in 60 g/L mAb 2. A  $g(s)$  plot from a sedimentation velocity experiment. Data were acquired with the fluorescence detection system.

The  $g(s)$  distribution from the 120 nM Alexa-mAb 2 sedimented in 80 g/L mAb 2 (Figure 56) was too complex to fit. However, evident in the data is material sedimenting between 25 and 30  $s(20,w)$ , an indication of extremely high order associations. In the graphs comparing the  $g(s)$  distributions of all concentrations of MAb 2 (Figures 57 and 58), it can be seen that the  $s(20,w)$  of the main peak steadily increases with concentration, clear evidence of a high amount of self-association. Again, sedimentation equilibrium will reveal more information about stoichiometry and molecular weights.

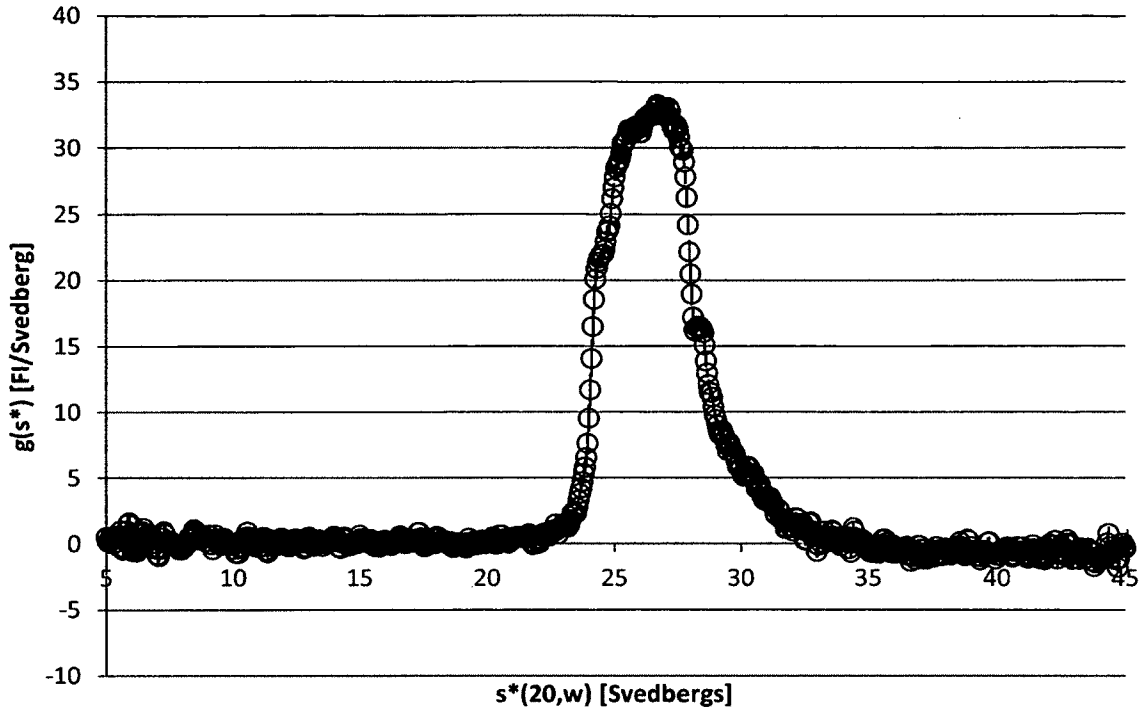


Figure 56. 120 nM Alexa-mAb 2 in 80 g/L mAb 2. A g(s) plot from a sedimentation velocity experiment. Data were acquired with the fluorescence detection system.

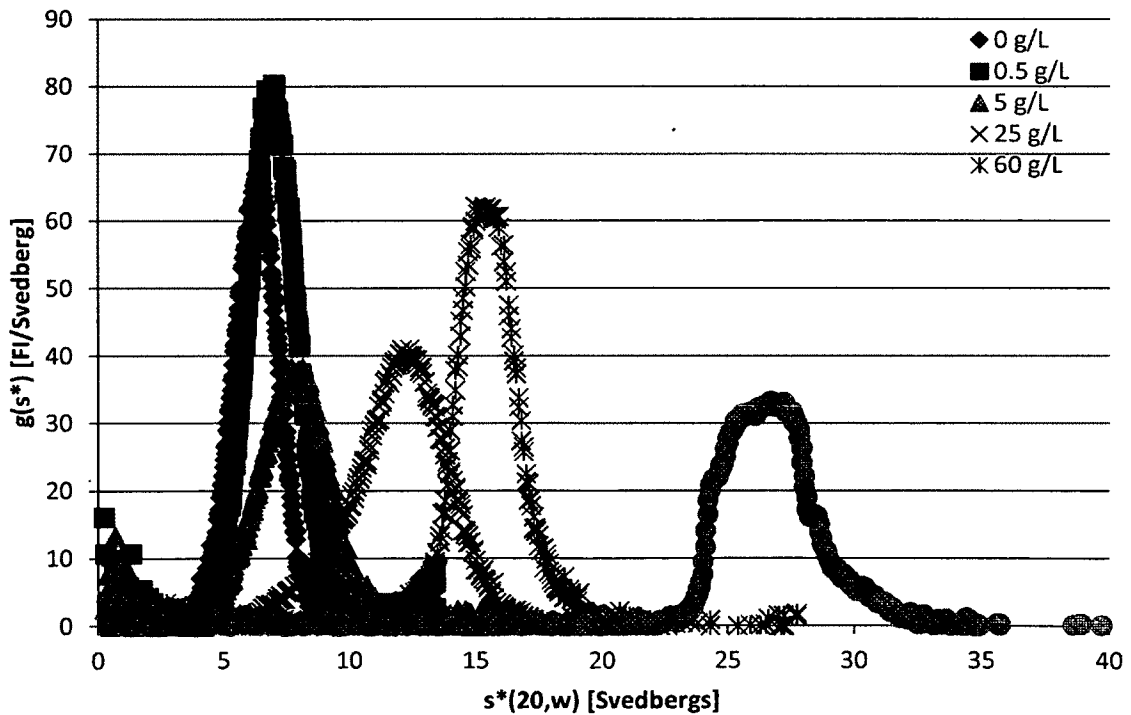


Figure 57. 120 nM Alexa-mAb2 in mAb 2. Graph shows g(s) plots for a series of sedimentation velocity experiments in the concentration of mAb 1 indicated by the legend. Data were acquired using the Fluorescence detection system.

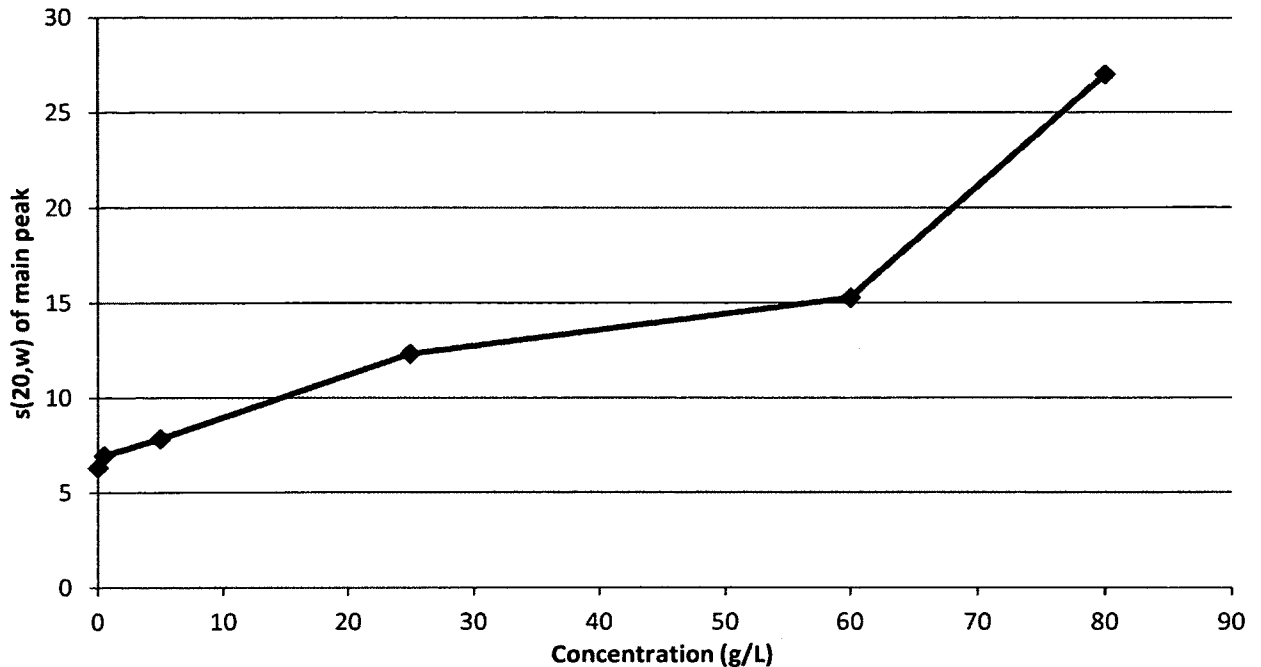


Figure 58. Results of sedimentation velocity experiments of labeled mAb 2 in the indicated concentration of mAb 2 (x axis).

MAB 3. At the concentrations of 0 to 6 g/L mAb 3 (Figures 59 – 61), 120 nM Alexa-mAb 3 fit to a single peak around 6.6 to 7.3 s, similar to the mAb 1 data and what would be expected of an antibody monomer. However, the  $s(20,w)$  does increase with increasing concentration of mAb 3, which could be evidence of self-association. At 30 g/L mAb 3 (Figure 62) this hypothesis is confirmed, as in this experimental condition the main peak is 9.25 s, about what would be expected of a dimer of a 6.65 s(20,w) protein. There is even evidence of monomer at lower  $s$ , about 8.1 s, which is a bit higher than would be expected of a pure monomer, but this peak could also be a reaction boundary. There is also evidence of higher order associations in this experimental condition indicated by a peak at 12.3 s(20,w), which is about the  $s(20,w)$  that would be expected of a triangular trimer of a 6.6 s(20,w) protein.

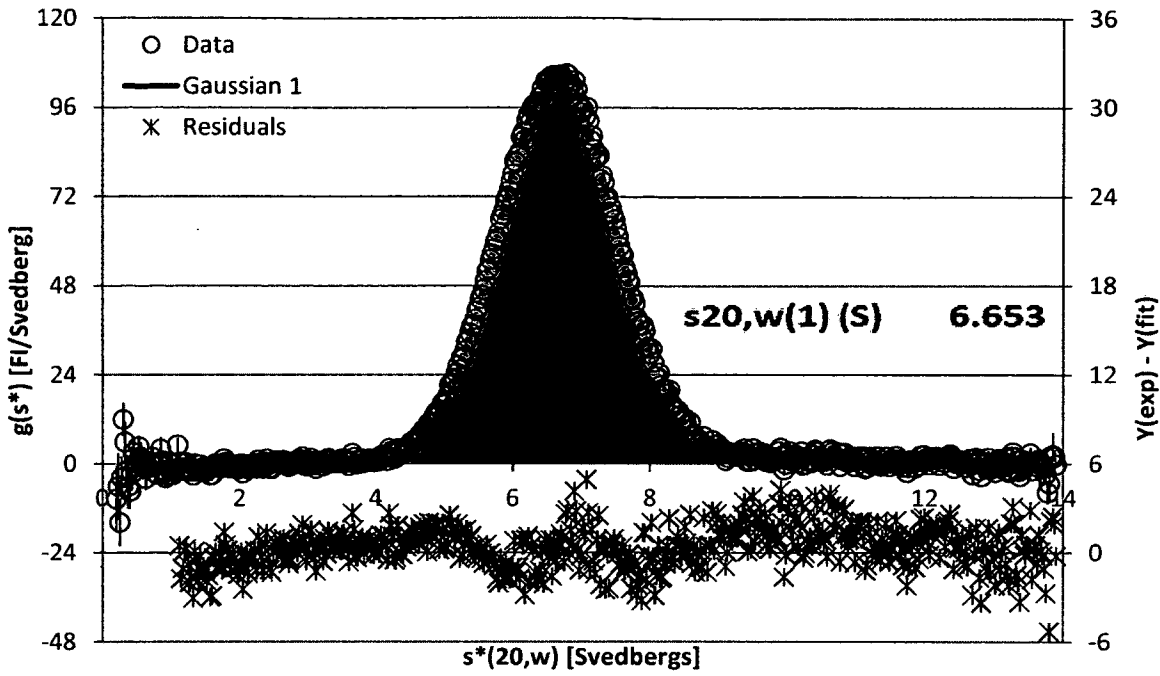


Figure 59. 120 nM Alexa-MAb 3 in 100 mM NaCl, 10 mM MES. A g(s) plot from a sedimentation velocity experiment. Data were acquired with the fluorescence detection system.

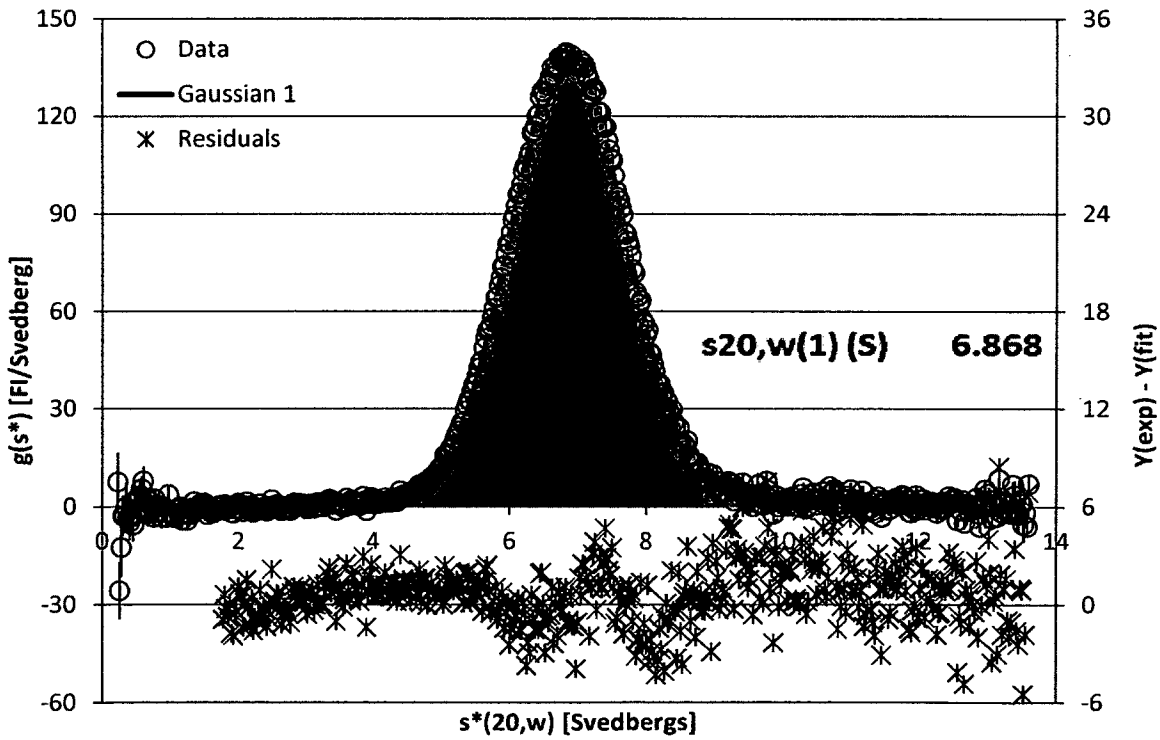


Figure 60. 120 nM Alexa-mAb 3 in 0.5 g/L mAb 3. A g(s) plot from a sedimentation velocity experiment. Data were acquired with the fluorescence detection system.



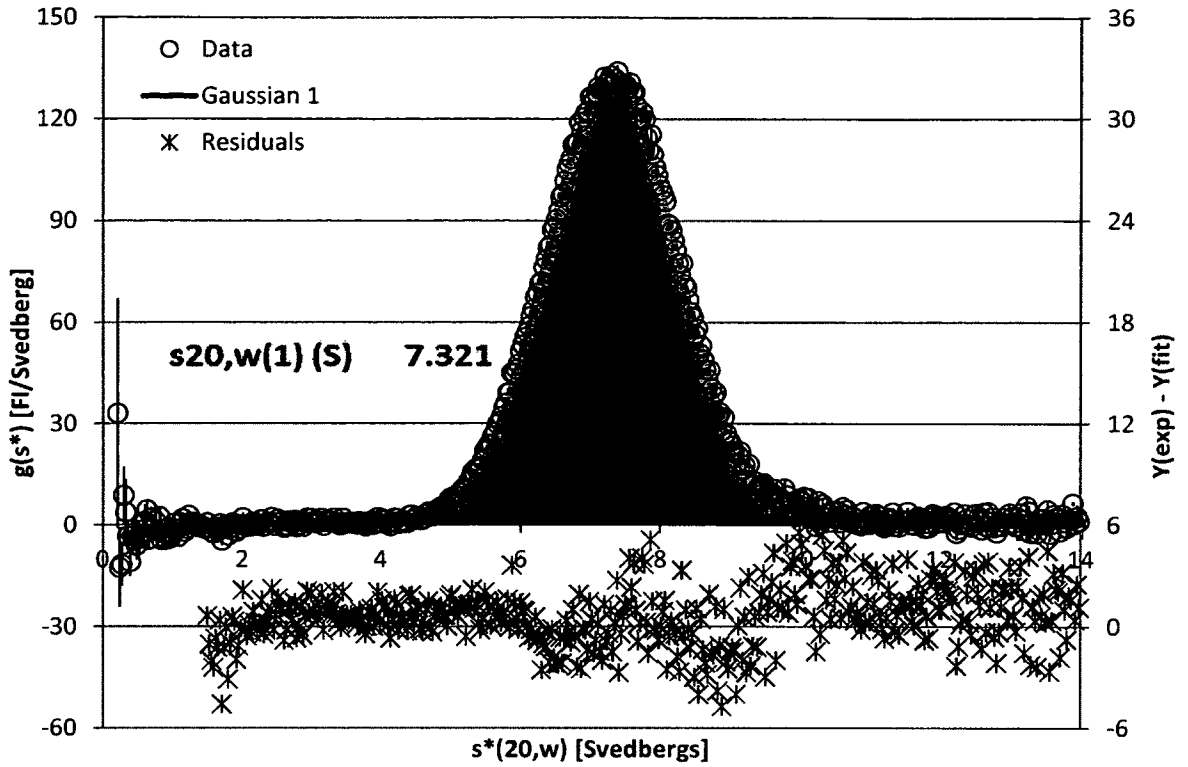


Figure 61. 120 nM Alexa-mAb 3 in 6 g/L mAb 3. A  $g(s)$  plot from a sedimentation velocity experiment. Data were acquired with the fluorescence detection system.

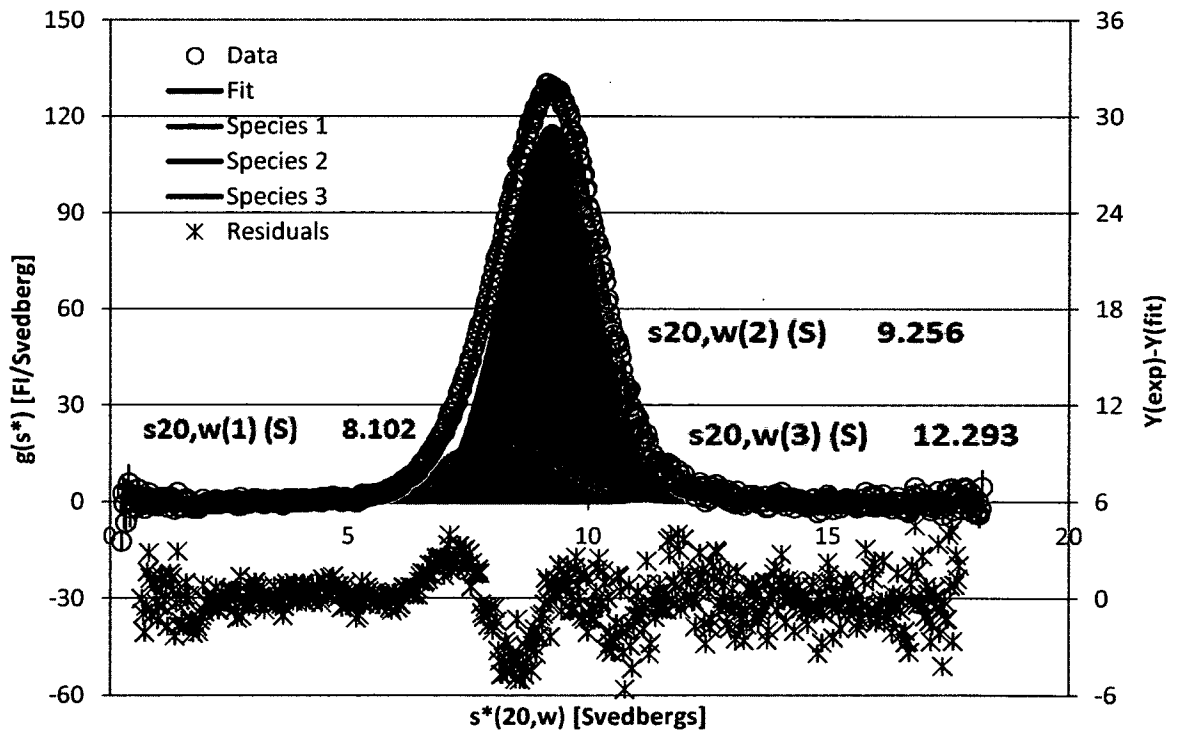


Figure 62. 120 nM Alexa-mAb 3 in 30 g/L mAb 3. A  $g(s)$  plot from a sedimentation velocity experiment. Data were acquired with the fluorescence detection system.

The next concentration of mAb 3, 60 g/L (Figure 63), also shows evidence of mAb 3 higher order self-associations. The main peak here is 13.7 s, which is about the  $s(20,w)$  that would be expected of a linear tetramer of a 6.6  $s(20,w)$  protein. There is also a peak at 11.6  $s(20,w)$ , which corresponds to a sedimentation coefficient ratio, to monomer, of about 1.75, about what would be expected of a linear trimer, however it is also quite possible that this 11.6  $s(20,w)$  peak is a reaction boundary between tetramer and lower order associations or monomer. There is also evidence of even higher order associations indicated by a peak at 14.65 s.

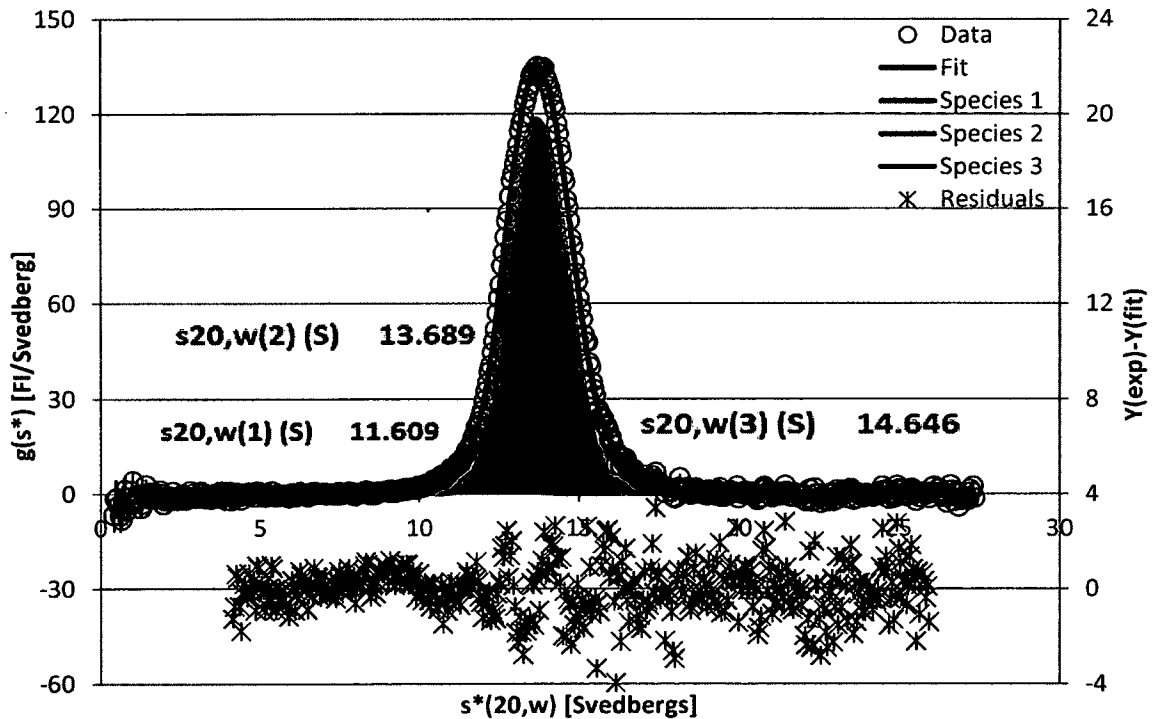


Figure 63. 120 nM Alexa-mAb 3 in 60 g/L mAb 3. A  $g(s)$  plot from a sedimentation velocity experiment. Data were acquired with the fluorescence detection system.

At the highest concentration of mAb 3, 100 g/L (Figure 64), the main peak ran at 15.76  $s(20,w)$ , much higher than any known conformation of tetramer would be expected

to run, and there is evidence of species running at even higher  $s(20,w)$  values, indicated by a peak at 16.37  $s(20,w)$ . The comparison graphs with all concentrations of mAb 3 (Figures 65 and 66) show the  $s(20,w)$  of the main peak steadily increasing with concentration, clear evidence of self-association. Sedimentation equilibrium will give a clearer picture as to molecular weights and stoichiometry of the associations.

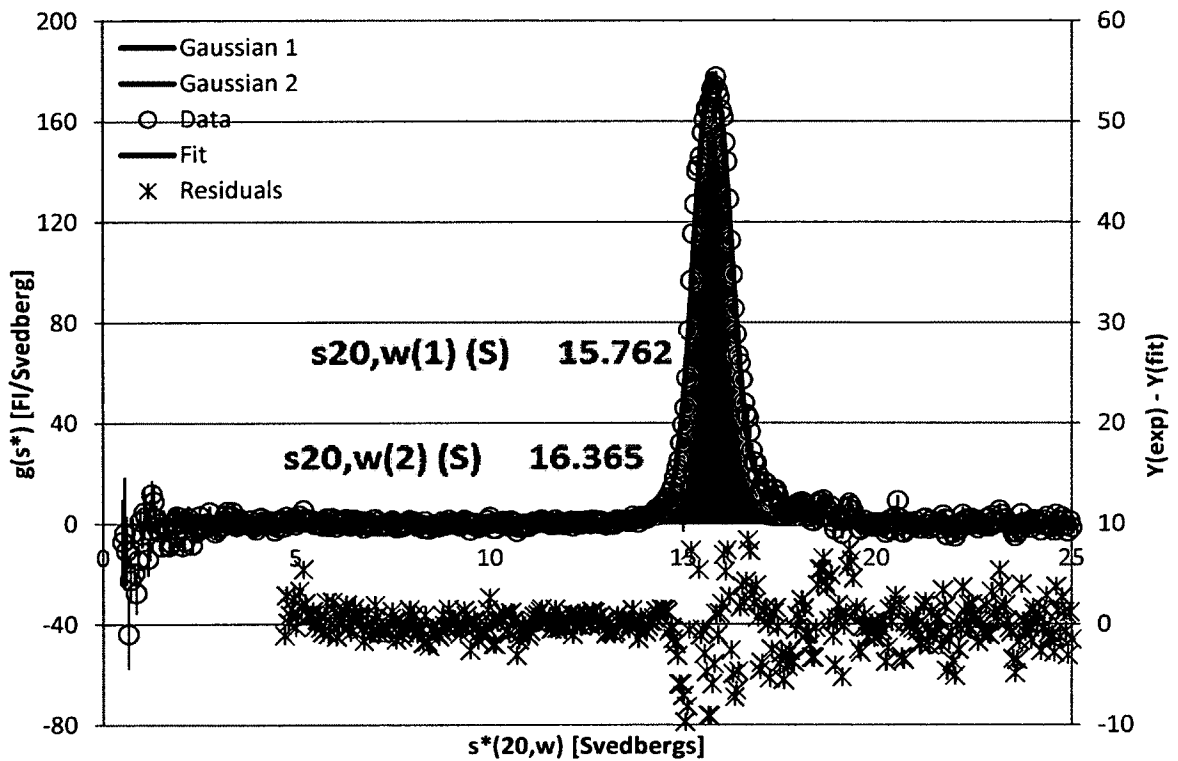


Figure 64. 120 nM Alexa-mAb 3 in in 100 g/L mAb 3. A  $g(s)$  plot from a sedimentation velocity experiment. Data were acquired with the fluorescence detection system.

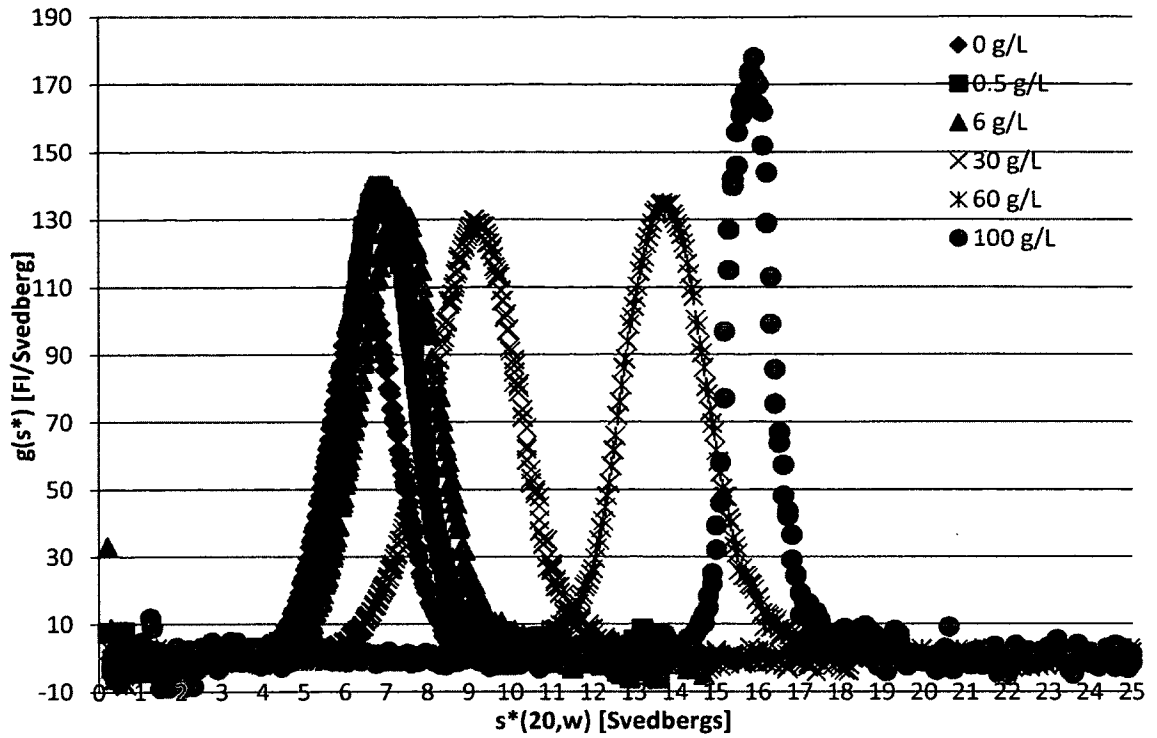


Figure 65. 120 nM Alexa-mAb3 in mAb 3. Graph shows  $g(s)$  plots for a series of sedimentation velocity experiments in the concentration of mAb 1 indicated by the legend. Data were acquired using the Fluorescence detection system.

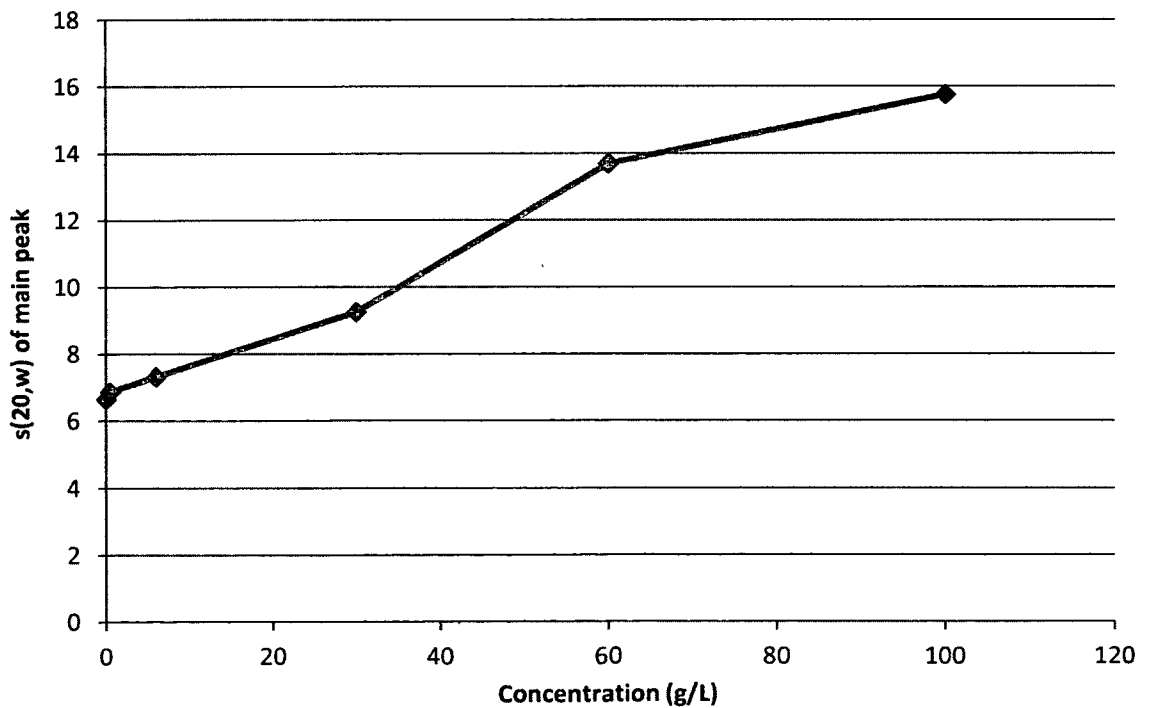


Figure 66. Results of sedimentation velocity experiments of labeled mAb 3 in the indicated concentration of mAb 3 (x axis).

### Sedimentation Equilibrium of Labeled mAb 1, 2, and 3 in High Concentrations of Themselves

In the sedimentation equilibrium experiments it can be seen that at and above 10 g/L mAbs 1, 2, and 3 fit to  $M/M(\text{app})$  significantly below 1 when fit to a single ideal species (Figure 67). mAb 2 started to fit to a  $M/M(\text{app})$  below 1 even earlier at 1 g/L. This information is consistent with all 3 of these molecules self-associating.

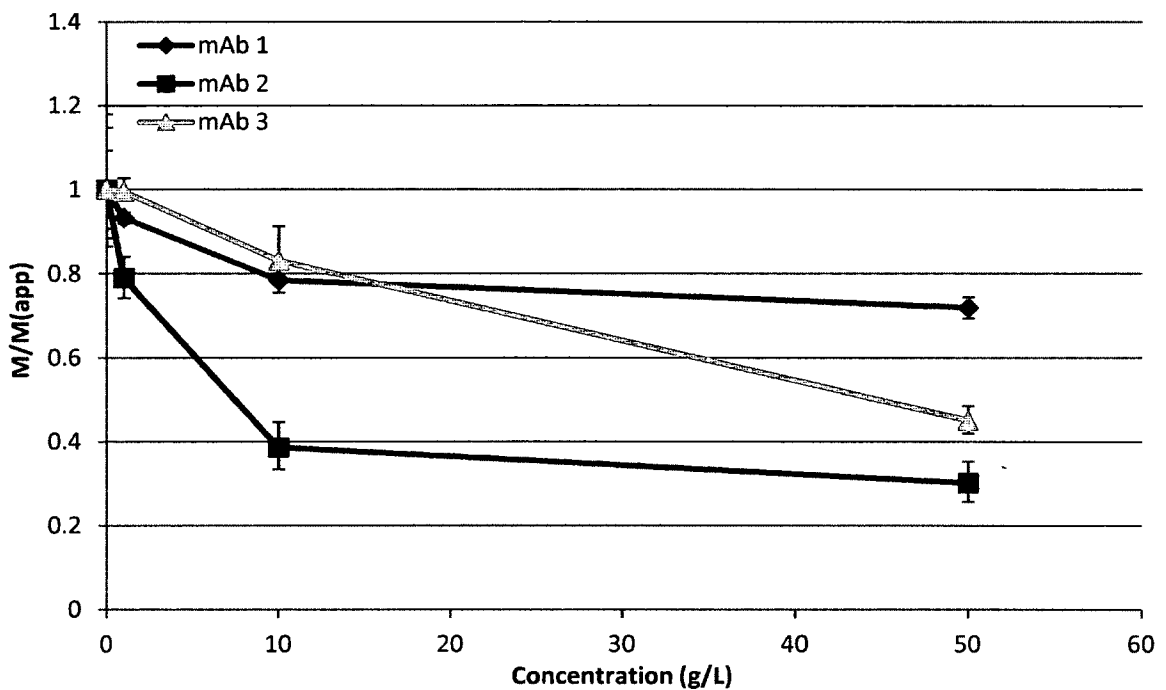


Figure 67.  $M/M(\text{app})$  of labeled mAbs in high concentrations of themselves. This graph summarizes a series of FDS sedimentation equilibrium experiments of labeled mAbs in high concentrations of themselves. The Y value of each data point in the experimental series is an average of 2 experiments conducted at rotor speeds 8K rpm and 12K rpm when fit to a single ideal species model.

When fit to a monomer-nmer association (Figure 68) it can be seen that the stoichiometry of mAb 1 association held fairly steady around 2 at the experimental conditions 1, 10 and 50 g/L and the  $\ln K$  of the dimerization was also fairly steady, around 3, in all of these experimental conditions.

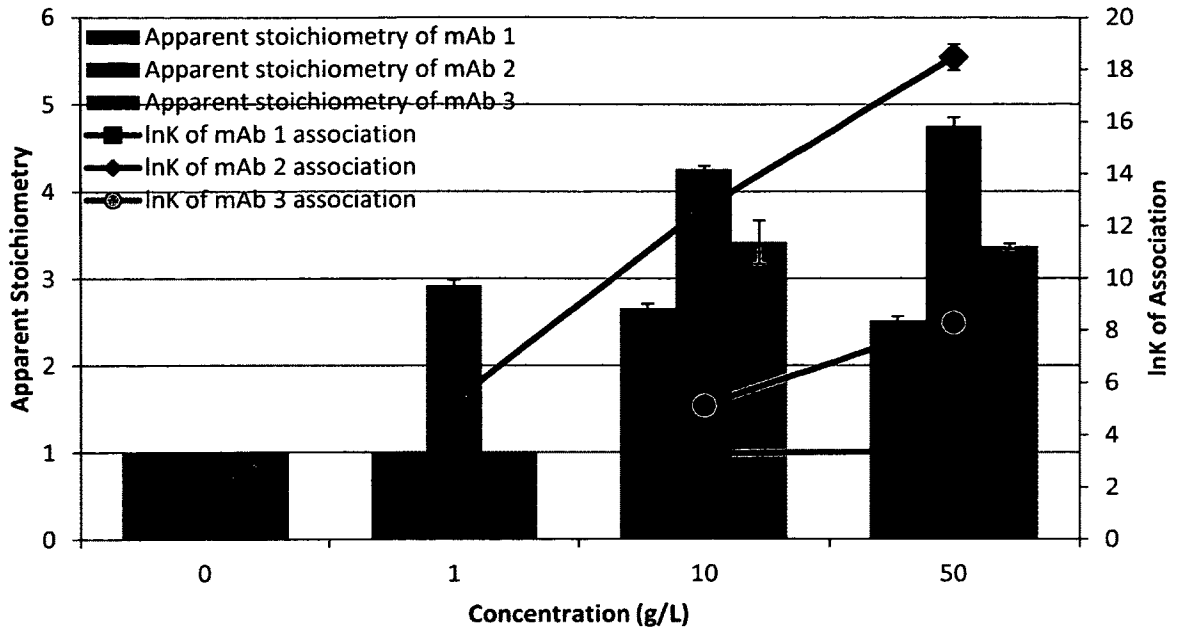


Figure 68. **Nature of mAb 1, 2, and 3 self-association.** Results of a fit of the previous data to a monomer-nmer association, where bars represent the stoichiometry of the association, and lines represent the lnK of the association, all averages of two experiments at 8k RPM and 12k RPM. A stoichiometry of one indicates that the experimental condition fit well to a single ideal species.

In contrast, the stoichiometry of mAb 2 association increased steadily across all of the experimental conditions that fit to a monomer-nmer association, as did the lnK of the association, all of which is characteristic of an indefinite association. Similarly, while only the 10 and 50 g/L mAb 3 conditions fit to a monomer-nmer association, both the stoichiometry and lnK of the association was increased at 50 g/L condition when compared to the 10 g/L condition, also characteristic of an indefinite association.

### Sedimentation Equilibrium in Low Salt (10 mM) Conditions of Labeled mAbs 1, 2, and 3 in High Concentrations of Themselves

In the sedimentation equilibrium experiments in 10 mM salt (Figures 69 and 70), it can be seen that mAb 1 no longer self-associates. This is evident by the  $M/M(\text{app})$  of mAb 1 remaining close to 1 over the concentration range (Figure 69) as well as a lack of improvement in the residuals when fit to a monomer-nmer model (Figure 70).

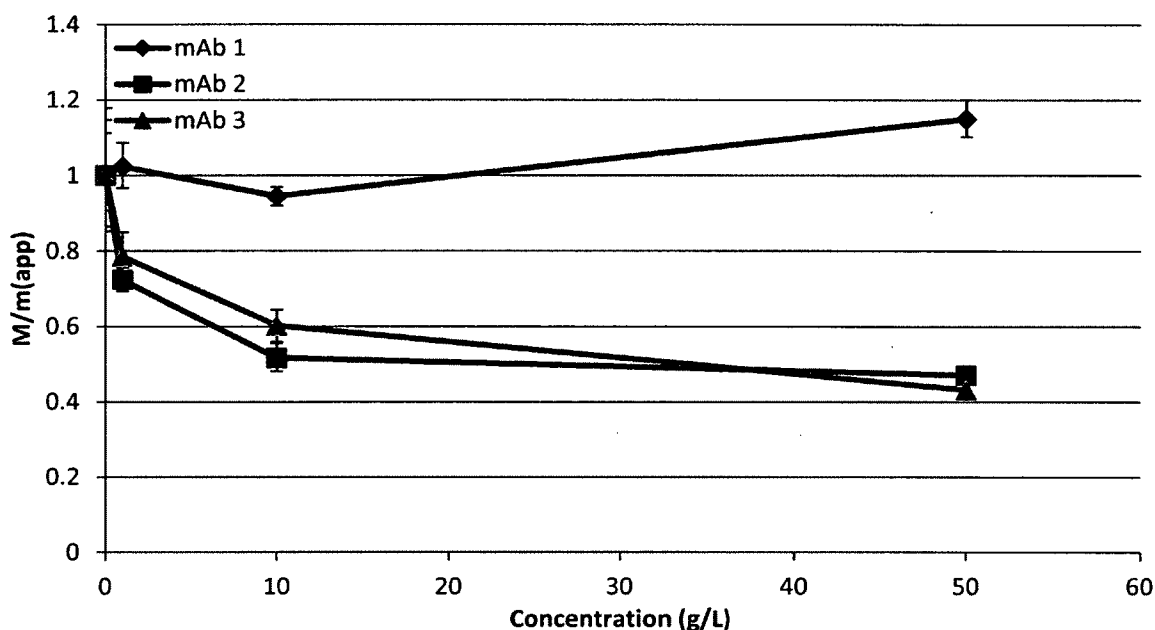


Figure 69.  $M/M(\text{app})$  of labeled mAbs in high concentrations of themselves in low salt (10 mM). This graph summarizes a series of FDS sedimentation equilibrium experiments of labeled mAbs in high concentrations of themselves. The Y value of each data point in the experimental series is an average of 2 experiments conducted at rotor speeds 8K rpm and 12K rpm when fit to a single ideal species model.

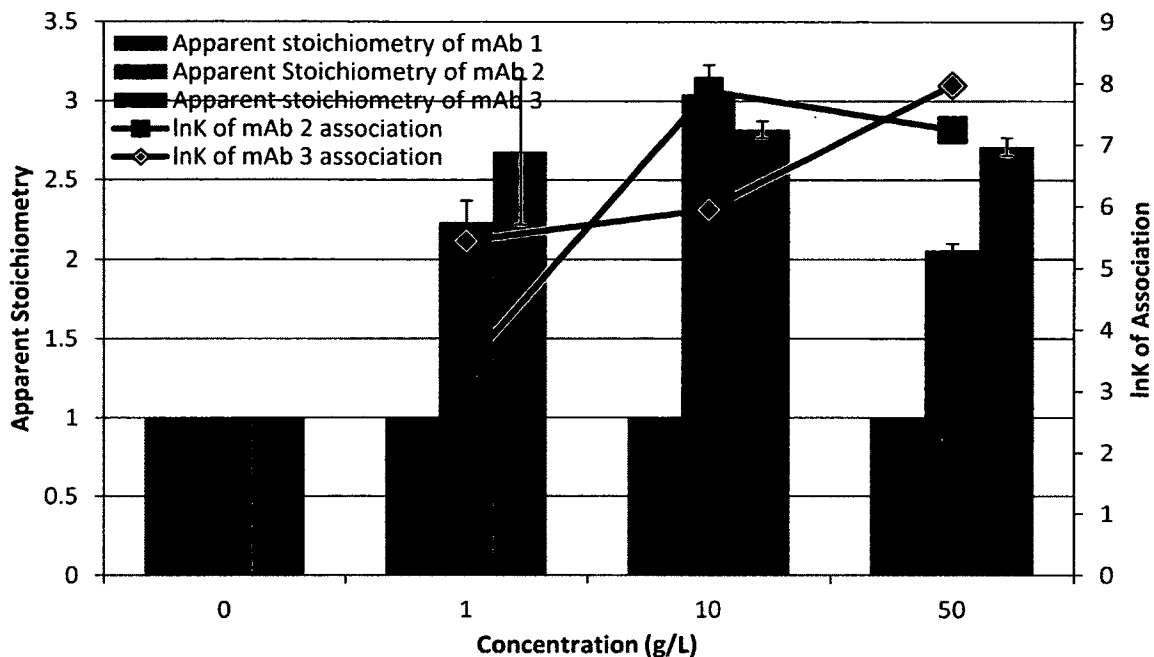


Figure 70. Nature of mAb 1, 2, and 3 self-association in low salt (10 mM). Results of a fit of the previous data to a monomer-nmer association, where bars represent the stoichiometry of the association, and lines represent the lnK of the association, all averages of two experiments at 8k RPM and 12k RPM. A stoichiometry of one indicates that the experimental condition fit well to a single ideal species.

Evident also in Figures 69 and 70 is that the self-association of mAb 2 has been reduced in 10 mM salt when compared to 100 mM salt. The  $M/M(\text{app})$  of mAb 2 is significantly higher in Figure 69 than in Figure 67 at the 10 and 50 g/L conditions. Additionally, at every concentration above g/L both the apparent stoichiometry and lnK of mAb 2 association is lower in Figure 70 when compared to Figure 68.

The self-association of mAb 3 appears to be somewhat unchanged in 10 mM salt when compared to 100 mM salt. At the highest concentration of 50 g/L the  $M/M(\text{app})$  of mAb 3 in Figure 69 is similar to that in Figure 67, although at the concentrations of 1 and 10 g/L the  $M/M(\text{app})$  was higher in Figure 69 than in Figure 67. When fit to a monomer-nmer association, the apparent stoichiometry of mAb 3 in 10 mM salt was between 2.5



and 3 at all concentrations above 0 g/L (Figure 70), while in 100 mM the apparent stoichiometry of mAb 3 was slightly above 3 (Figure 68). In 10 mM salt the  $\ln K$  of mAb 3 association increased from about 5.5 at the lowest concentration to about 8 at the highest concentration (Figure 70). In 100 mM salt the  $\ln K$  of mAb 3 association had similar values, increasing from about 5 at the lowest concentration association was observed to about 8 at the highest.

### **Sedimentation Velocity of Labeled mAb 1, 2, and 3 in Serum**

The resulting  $g(s)$  plots from experiments of labeled mAb 1, mAb 2, and mAb 3 sedimented in serum all looked very similar (Figures 71 – 79). All had the 3.5 to 4  $s(20,w)$  autofluorescent serum component seen in the control of 100% serum with no added components. Apart from this autofluorescent serum component all conditions had a main peak ranging from 6.7 to 8.4  $s(20,w)$  representing the labeled antibody, and some higher molecular weight material running faster than the labeled antibody, evidence of the antibody interacting with a serum component, most likely serum IgG. In the conditions of Alexa-mAb 1 sedimented in higher serum concentrations this higher  $s(20,w)$  material could not be fit to, but systematic error present in the residuals in the area immediately following the antibody peak indicate that there are still interactions between antibody and serum components under these conditions.

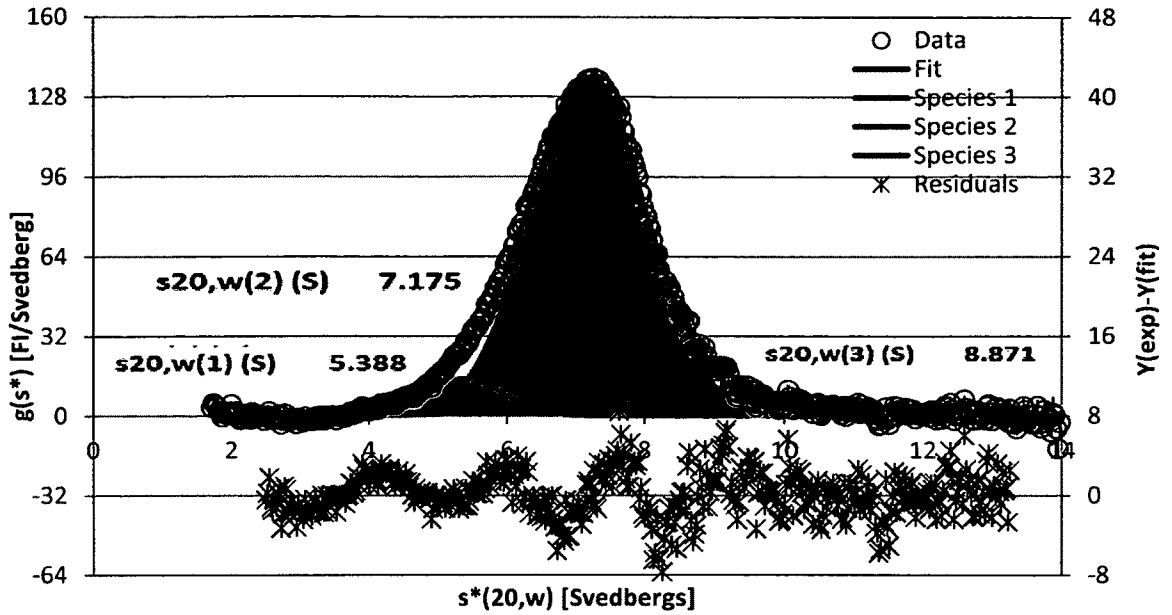


Figure 71. 120 nM Alexa-mAb 1 in 25% serum. A  $g(s)$  plot from a sedimentation velocity experiment. Data were acquired with the fluorescence detection system.

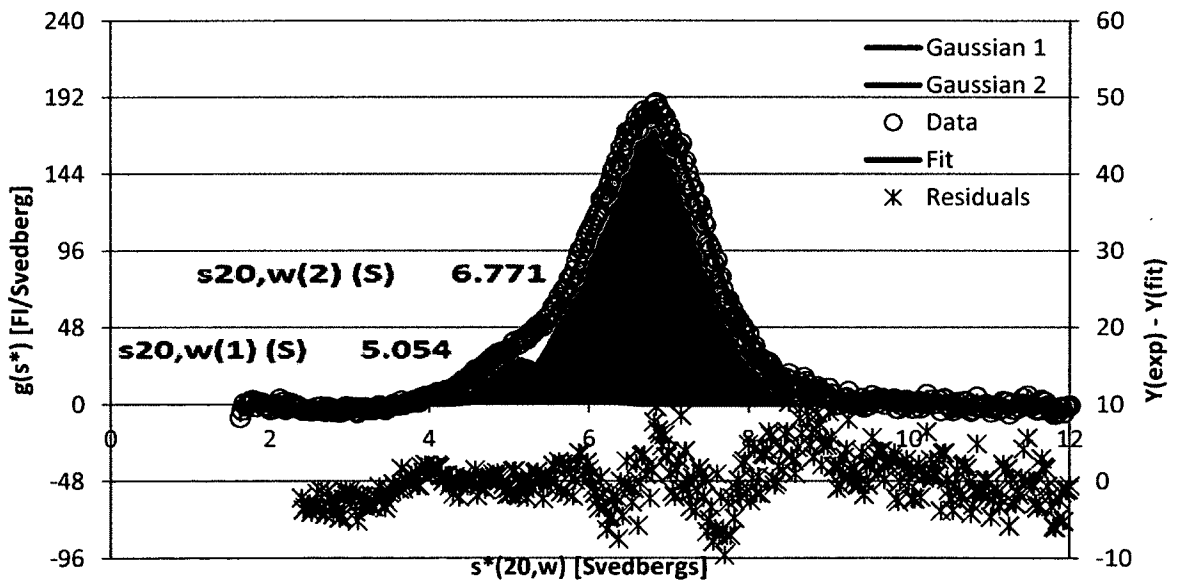


Figure 72. 120 nM Alexa-mAb 1 in 50% serum. A  $g(s)$  plot from a sedimentation velocity experiment. Data were acquired with the fluorescence detection system.

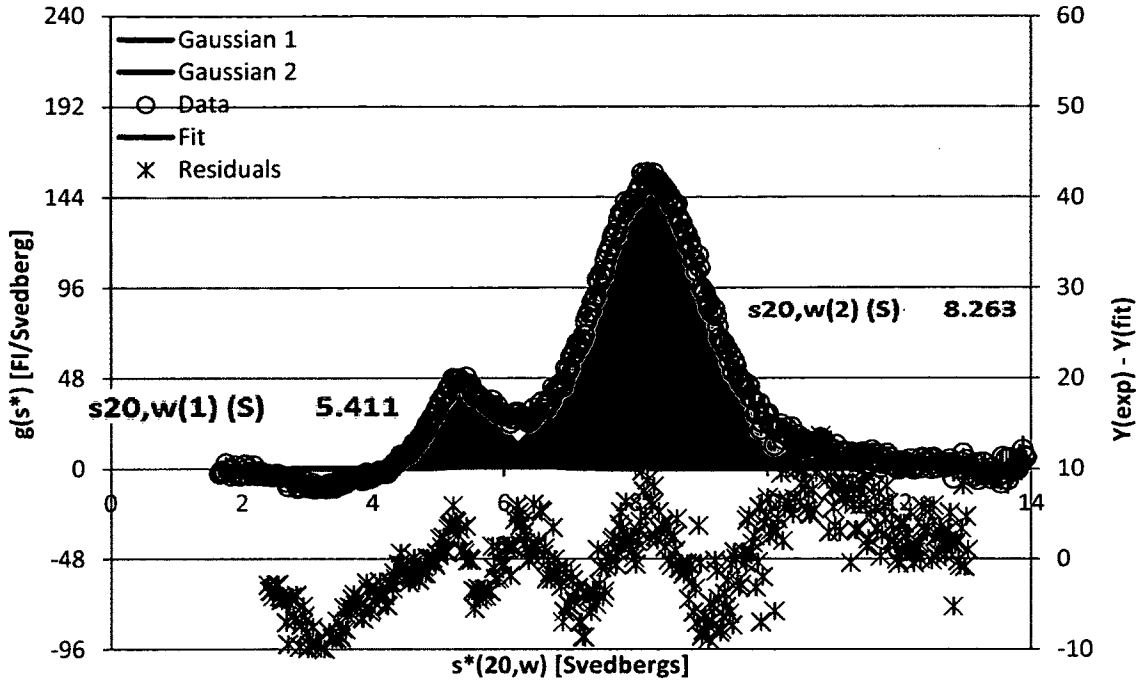


Figure 73. 120 nM Alexa-mAb 1 in 100% serum. A  $g(s)$  plot from a sedimentation velocity experiment. Data were acquired with the fluorescence detection system.

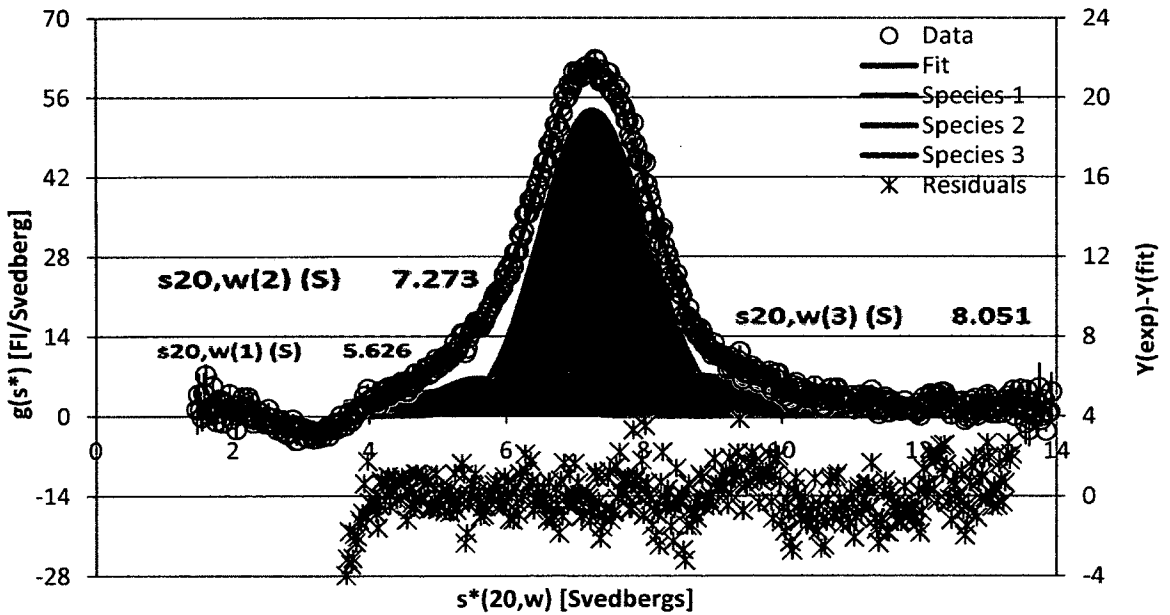


Figure 74. 120 nM Alexa-mAb 2 in 25% serum. A  $g(s)$  plot from a sedimentation velocity experiment. Data were acquired with the fluorescence detection system.

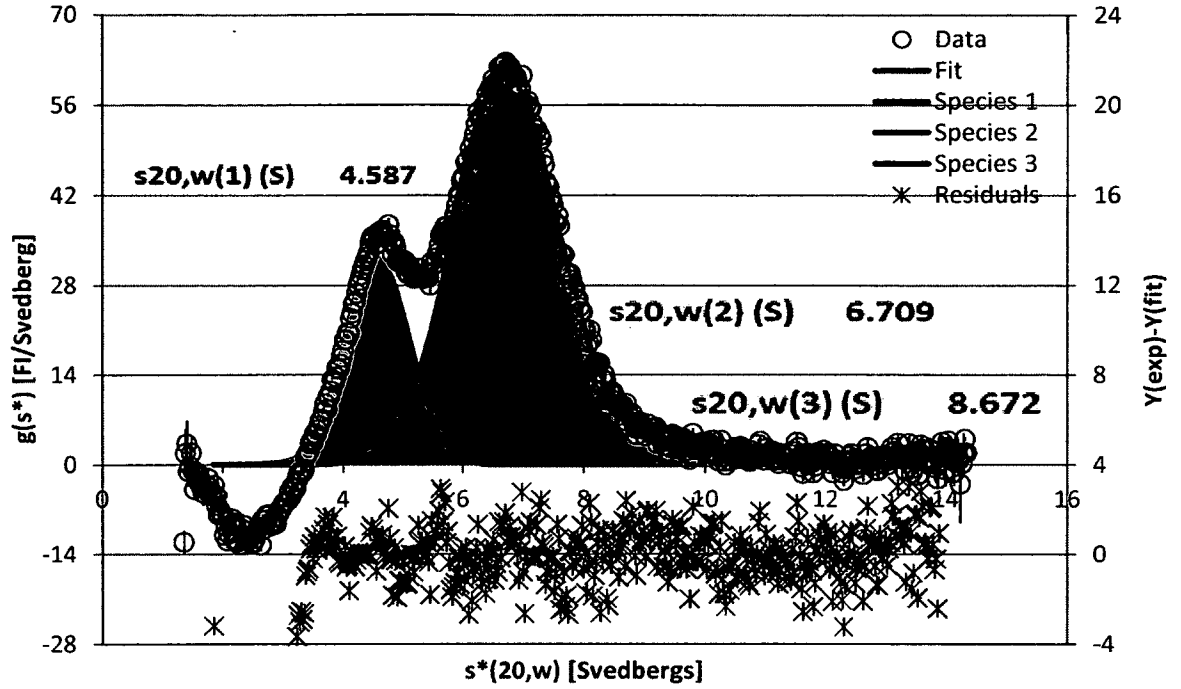


Figure 75. 120 nM Alexa-mAb 2 in 50% serum. A  $g(s)$  plot from a sedimentation velocity experiment. Data were acquired with the fluorescence detection system.

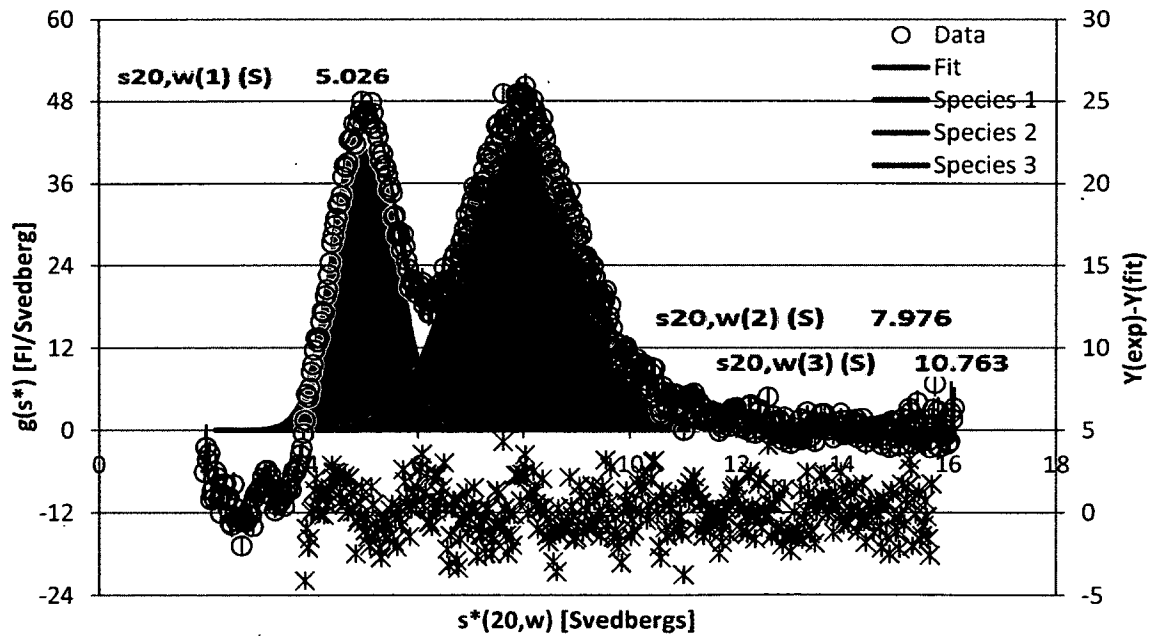


Figure 76. 120 nM Alexa-mAb 2 in 100% serum. A  $g(s)$  plot from a sedimentation velocity experiment. Data were acquired with the fluorescence detection system.

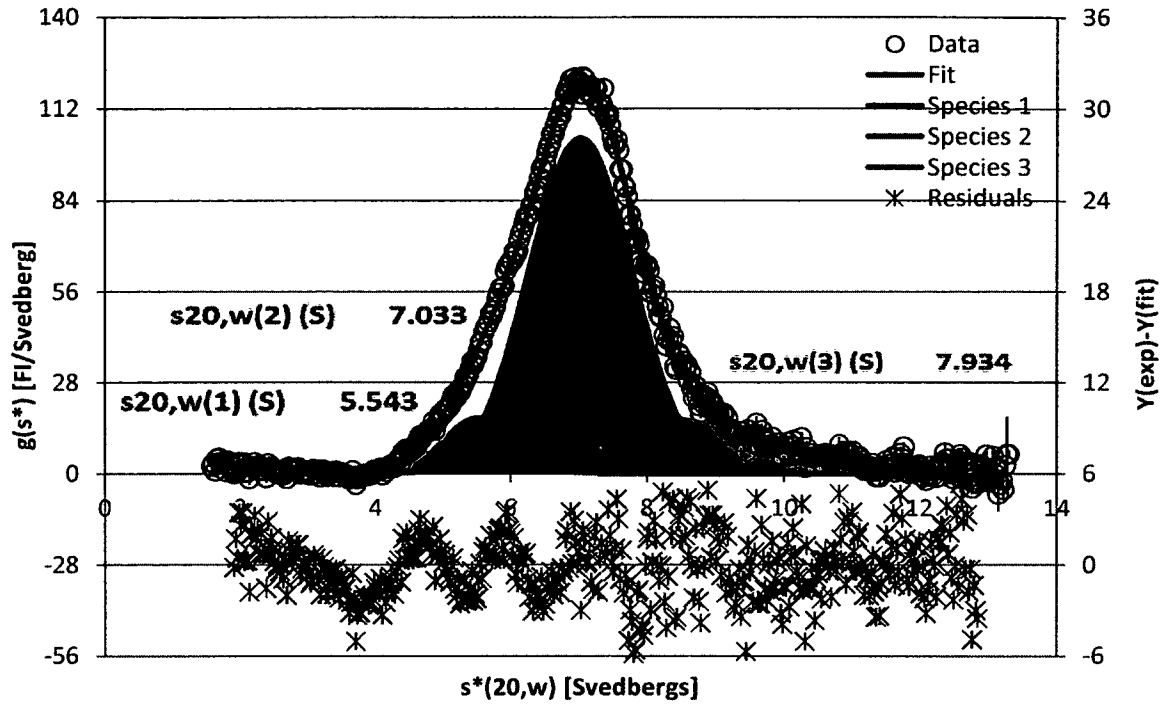


Figure 77. 120 nM Alexa-mAb 3 in 25% serum. A  $g(s)$  plot from a sedimentation velocity experiment. Data were acquired with the fluorescence detection system.

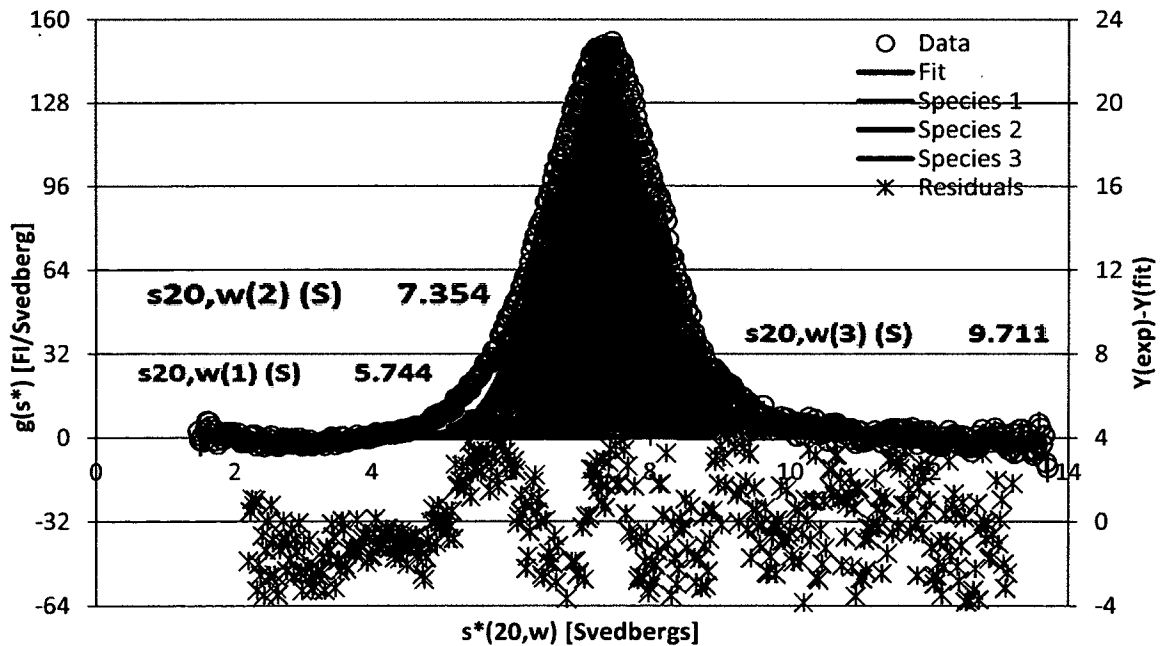


Figure 78. 120 nM Alexa-mAb 3 in 50% serum. A  $g(s)$  plot from a sedimentation velocity experiment. Data were acquired with the fluorescence detection system.

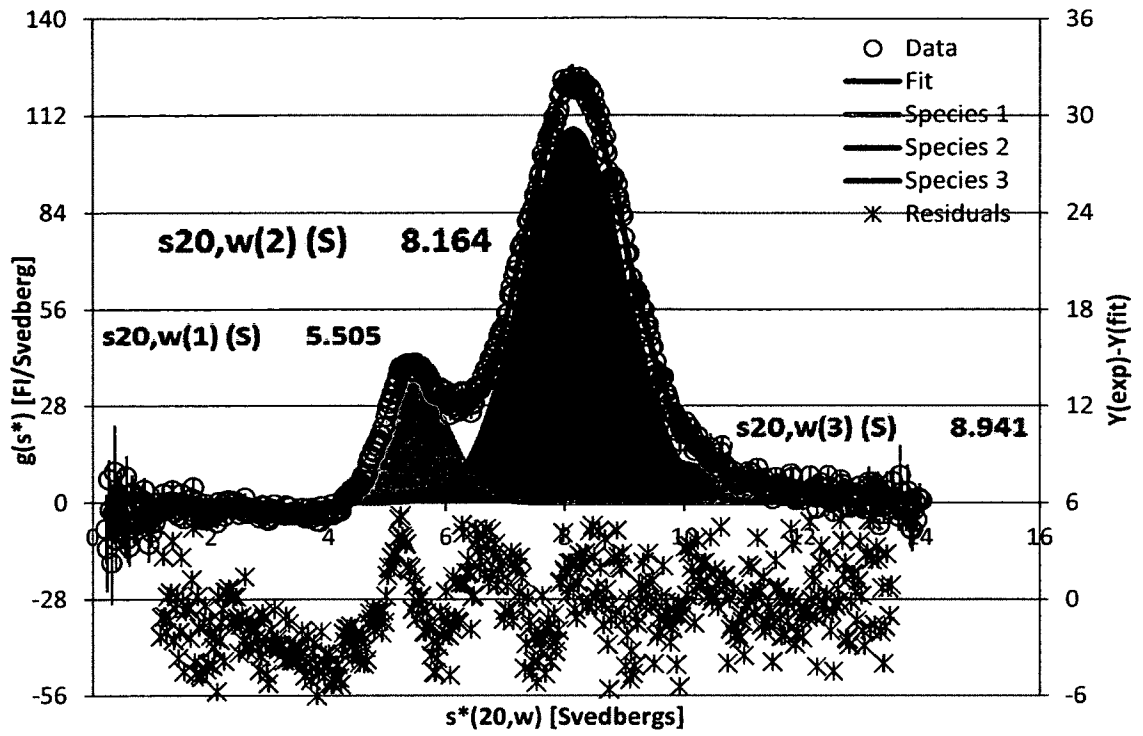


Figure 79. 120 nM Alexa-mAb 3 in 100% serum. A  $g(s)$  plot from a sedimentation velocity experiment. Data were acquired with the fluorescence detection system.

## CHAPTER VII

### DISCUSSION

#### **Hypothesis I: The FDS Will Enable the Tracking of a Single Component in a Complex Mixture**

The promise of using the FDS with sedimentation equilibrium and sedimentation velocity was that it would enable the tracking of a single component in a complex solution. A related hypothesis was that with the FDS the complexity of the solution would become irrelevant. The first hypothesis was confirmed up to a certain level of solution complexity. The FDS successfully allowed for the tracking of GFP during sedimentation experiments of two component solutions (GFP and a background molecule) and three component solutions (GFP, anti-GFP, and a background molecule).

However, this method broke down when applied to serum. Sedimentation equilibrium could not be used because the data could not be fit to a sum of exponential functions. These data contained inflection points and areas where concentration decreased with radial position that no model can account for. For this reason a program such as MixRat becomes extremely compelling, as it does not rely on a model. Sedimentation velocity was difficult to apply to serum as well. At the higher serum concentrations multiple simultaneous Johnston-Ogston effects had multiple effects on the  $g(s^*)$  plots that prevented quantitative fits, such as non-Gaussian peaks and areas of

negative  $g(s^*)$ . These effects cannot be accounted for by the Faxen approximation of the Lamm equation and thus quantitative results cannot be obtained. The resulting poor fits restrict the conclusions that can be reached to very qualitative ones.

Therefore, while the first hypothesis was confirmed, in that GFP was able to be analyzed in two and three component solutions, the second hypothesis that this could be done at any level of solution complexity cannot be confirmed, since the sedimentation methods broke down when applied to serum. A very effective work-around was the process of labeling serum components and sedimenting them in serum. This allowed for the putative identification of peaks in the GFP in serum data based on information obtained in other experiments. However, this did not obviate the inability to reach quantitative conclusions.

### **Hypothesis II: The Nonideality of the Tracer Will Differ from the Nonideality of the Background**

Another hypothesis, that the nonideality of a tracer (GFP) will differ from the nonideality of the background solution, was confirmed. There were many examples in which the activity of GFP in a solution was drastically different from the activity of that solution alone, such as the  $M/M_{app}$  of GFP in HEL when compared to that of HEL alone (Figure 11) and the  $M/M_{app}$  of GFP in dextran when compared to that of dextran alone (Figure 9).

The nonideality of a tracer will differ from the nonideality of the background if the properties of the molecules differ significantly. For example, in the case of GFP in HEL,



the charge of GFP differs significantly from that of HEL, so the activity of HEL in a high concentration solution of HEL differs significantly from the activity of GFP in a high concentration solution of HEL (Figure 11). In the case of GFP in STI, the charge of GFP is similar to that of STI, therefore the activity of STI in a high concentration solution of STI was similar to that of GFP in a high concentration solution of STI (Figure 10).

### **Hypothesis III: Sedimentation Velocity is as Effective as Sedimentation Equilibrium in the Analysis of Complex Solutions**

Another hypothesis was that sedimentation velocity could provide similar insights as sedimentation equilibrium, and that the former could be used in place of the latter. This hypothesis was confirmed for the 2 component systems; both sedimentation velocity and equilibrium were able to identify favorable interactions between GFP and HEL, GFP and dextran. While sedimentation velocity was able to identify the nature of the interaction through addition of excipients, similar experiments could have been done with sedimentation velocity. In fact, sedimentation velocity was able to provide further insights such as how many high molecular weight GFP forms were present and how large they were and the slight attraction between GFP and STI as evidenced by higher molecular weight GFP forms. The only caveat to this is that the information obtained through sedimentation velocity regarding nonideality is somewhat qualitative in that it is only able to say whether or not attractive interactions are present or not, and the extent of the interactions. If information regarding the chemical activity or second virial coefficient of the solution is sought, sedimentation equilibrium must be used.

As an additional note, this hypothesis was only confirmed in the above cases where the signal molecule sedimented ahead of the background molecule. This hypothesis was not tested in a case where the signal molecule would sediment slower than the background molecule.

This hypothesis was not confirmed when serum data were analyzed as both methods as originally described broke down and were unable to adequately describe the solution. However, with some modifications, both methods show promise. In sedimentation velocity the labeling of serum components and subsequent sedimentation in serum allowed for quantitative information to be obtained and then linked to features of the qualitative “big picture” experiment involving GFP in serum. In sedimentation equilibrium the use of MixRat on this highly irregular data will provide additional insights.

**Hypothesis IV: The Proximity Energy Framework, When Applied to a New System Involving the Molecules mAb 1, mAb 2, and mAb 3, Can Adequately Account for the Experimental Data.**

As mAb 1, mAb 2, and mAb 3 were demonstrated to have very little to no charge (Table 2), and one of the most common sources of high viscosity in solutions is a strong dipole of one of the solutes, it can be hypothesized that the amount of viscosity seen in Figure 41 is a result of these mAbs having a strong dipole moment, and that the amount of viscosity would correlate with the strength of the dipole. Under this hypothesis it would be expected that mAb 2 would have the highest dipole moment, as it has the

higher viscosity. It would also be expected that mAb 3 would have an intermediate dipole and mAb 1 would have to lowest dipole moment, for similar reasons.

If the dipole moment is also viewed as the source of the self-association of these mAbs, or at least the major impetus, it could be hypothesized that mAb 1 would be the most well-behaved of these molecules, as it has the lowest dipole. This hypothesis is supported by the equilibrium data (Figure 68), where mAb 1 associated the least as measured by both stoichiometry and  $\ln K$  of the association.

Following this hypothesis, it would be expected that mAb 2 would self-associate the most, as it has the highest dipole, and that the amount of mAb 3 association would fall somewhere between the other two. These are partially supported by the equilibrium data (Figure 68), as at every experimental condition mAb 2 had by far the highest  $\ln K$  of association. At every condition of mAb 2 that fit to a monomer-nmer association the stoichiometry of association was slightly larger than that of mAb 3, however the  $\ln K$  of association was far lower, although still above that of mAb 1.

In the 10 mM salt conditions, it was seen that the self-association of mAb 1 was completely eliminated when compared to the 100 mM salt condition, the self-association of mAb 2 was reduced when compared to the 100 mM salt condition, and the self-association of mAb 3 was not clearly affected in one direction or the other when compared to the 100 mM salt condition. This correlates in an interesting way with the charge data (Table 2); all three had no charge at 100 mM salt, mAb 1 had the highest charge at 10 mM salt, mAb 2 had an intermediate charge at 10 mM salt, and the results for mAb 3 were ambiguous at 10 mM salt. Therefore, it appears that the magnitude of

the mAb charge at 10 mM salt correlates with a reduction of the self-association exhibited by the mAb when compared to 100 mM salt, i. e. the more charge a mAb has at 10 mM salt, the more its self-association is reduced. These results indicate that charge-charge repulsion significantly impedes the interactions of these molecules with themselves under conditions of low salt.

## REFERENCES

Adkins, J., Varnum, S., Auberry, K., Moore, R., Angell, N., Smith, R., Springer, D., and Pounds, J. Toward a human blood serum proteome: analysis by multidimensional separation coupled with mass spectrometry. 2002. *Molecular and Cellular Proteomics* 1 (12): 947–955.

An, Z. *Therapeutic Monoclonal Antibodies: From Bench to Clinic*. Hoboken, New Jersey: John Wiley and Sons, Inc., 2003.

Banerjee, S., Pogolotti, A., and Rupley, J. Self-Association of Lysozyme. 1975. *The Journal of Biological Chemistry* 250(20):8260-8266.

Bean, S. 2004. Senior Thesis, Biochemistry, University of New Hampshire. Advisor: Tom Laue.

Belnikovich, N., Budtova, T., Ivanova, N. Panarin, Y., Panov, Y., and Frenkel, S. Vysokomolek. Soed. Ser. A, 31, 1691 (1989).

Bhavani, A. and Nisha, J. Dextran, the polysaccharide with versatile uses. 2010. *International Journal of Pharma and Bio Sciences* 1(4): 569-573.

Cole, J. Analysis of heterogeneous interactions. 2004. *Methods Enzymol.* 384:212-32.

Cole, J., Lary, J., Moody, T., and Laue, T. Analytical Ultracentrifugation: Sedimentation Velocity and Sedimentation Equilibrium. 2008. *Methods Cell Biol.* 84:143–179.

Cromwell, M., Hilario, E., and Jacobson, F. Protein Aggregation and Bioprocessing. *AAPS Journal*. 2006. 8(3): E572-E579.

Cruts, M., Gijssels, I., van der Zee, J., Engelborghs, S., Wils, H., Pirici, D., Rademakers, R., Vandenberghe, R., Dermaut, B., Martin, J., van Duijn, C., Peeters, K., Sciot, R., Santens, P., De Pooter, T., Mattheijssens, M., Van den Broeck, M., Cuijt, I., Vennekens, K., De Deyn, P., Kumar-Singh, S., and Van Broeckhoven, C. Null mutations in progranulin cause ubiquitin-positive frontotemporal dementia linked to chromosome. 2006. *Nature* 442(7105): 920–4.

Dani, B., Platz, R., and Tzannis, T. High concentration formulation feasibility of human immunoglobulin G for subcutaneous administration. 2007. *J Pharm Sci.* 96(6):1504-17.

Davis, S. and Vierstra, R. Soluble, highly fluorescent variants of green fluorescent protein (GFP) for use in higher plants. 1998. *Plant Molecular Biology* 36:521–528.

Ellis, R. Macromolecular Crowding: obvious but underappreciated. 2001. *Trends in Biochem. Sci.*, 26(10) 597-604.

Fundueanu, G., Nastruzzi, C., Carpov, A., Desbrieres, J., and Inaudo, M. Physico-chemical characterization of Ca-alginate microparticles produced with deferent methods. 1999. *Biomaterials* 20:1427-1435.

Granath, K. Solution properties of branched dextrans. 1958. *Journal of Colloid Science* 13(4):208-328.

Hall, D. and Minton, A. Macromolecular crowding: qualitative and semi-quantitative successes, quantitative challenges. 2003. *Biochimica et Biophysica Acta* 1649(2003):127-139.

Jain, D., Nair, D., Swaminathan, A., Abraham, E., Nagaraju, J., and Salunke., D. Structure of the Induced Antibacterial Protein from Tasar Silkworm, *Antheraea mylitta*. 2001. *The Journal of Biological Chemistry*, 276:41377-41382.

Kroe, R. 2005. Masters Thesis, University of New Hampshire. Advisor: Dr. Thomas Laue.

Lamm, O. Die differentialgleichung der ultrazentrifugierung. 1929. *Arkiv för matematik, astronomi och fysik* 21B No. 2, 1–4.

Laue, T. Proximity energies: a framework for understanding concentrated solutions. 2012. *Journal of Molecular Recognition* 25(3): 165–173.

Lin, Y., Ying, T., and Liao, L. Molecular modeling and dynamics simulation of a histidine-tagged cytochrome b<sub>5</sub>. 2011. *J Mol Model.* 17(5):971-8.

Martonen, T., Smyth, H., Isaacs, K., and Burton, R. Issues in Drug Delivery: Concepts and Practice. 2005. *Respiratory Care* 50(9):1228-1252.

McNaughton, B., Cronican, J., Thompson, D., and Liu, D. Mammalian cell penetration, siRNA transfection, and DNA transfection by supercharged proteins. 2009. *PNAS* 106(15):6111-6116.

Minton, A. Influence of excluded volume upon macromolecular structure and associations in “crowded” media. 1997. *Current Opinion in Biotechnology* 8(1): 65–69.

Minton, A. The effective hard particle model provides a simple, robust, and broadly applicable description of nonideal behavior in concentrated solutions of bovine serum albumin and other nonassociating proteins. 2007. *Journal of Pharmaceutical Sciences* 96(12): 3466–3469.

Minton, A. The Influence of Macromolecular Crowding and Macromolecular Confinement on Biochemical Reactions in Physiological Media. 2001. *J. Biol. Chem.* 276(14): 10577-10580.

Parsegian, V. and Gingell, D. On the electrostatic interaction across a salt solution between two bodies bearing unequal charges. 1972. *Biophysical Journal* 12(9):1192-1204.

Pattanaboonmee, N., Ramasamy, P., Yimnirun, R., and Manyum, Y. A comparative study on pure, L-arginine and glycine doped ammonium dihydrogen orthophosphate single crystals grown by slow solvent evaporation and temperature-gradient method. 2001. *Journal of Crystal Growth* 314(1):196–201.

Philo, J. A method for directly fitting the time-derivative of sedimentation velocity data and an alternative algorithm for calculating sedimentation coefficient distribution functions. 2000. *Anal. Biochem.* 279:151-163.

Purohit, V., Middaugh, C., and Balasubramanian, S. Influence of Aggregation on Immunogenicity of Recombinant Human Factor VIII in Hemophilia A Mice. 2006. *J Pharm Sci.* 95(2): 358–371.

Rackis, J., Sasame, H., Mann, R., Anderson, R., and Smith, A. Soybean Trypsin Inhibitors: Isolation, Purification and Physical Properties. 1962. *Archives of Biochemistry and Biophysics* 98, 471-478.

Rhodes, C., Holocomb, D., and Van Holde, K. Physical studies of lysozyme. 1962. *J Biol Chem.* 237:1107-12.

Rivas, G., Fernandez, J., and Minton, A. Direct Observation of the Self-Association of Dilute Proteins in the Presence of Inert Macromolecules at High Concentration via Tracer Sedimentation Equilibrium: Theory, Experiment, and Biological Significance. 1999. *Biochemistry* 38(29): 9379–9388.

Rong, Y. Probing the Structure of Dextran Systems and Their Organization. Masters thesis, Rutgers, Food Science. Advisor: Jozef L. Kokini.

Rosenberg, A. Effects of Protein Aggregates: An Immunologic Perspective. *AAPS Journal.* 2006. 8(3): E501-E507

Sauer, U., Heinemann, M., and Zamboni, N. Getting Closer to the Whole Picture. 2007. *Science* 316(5824): 550-551.

Shindo, H., Cohen, J., and Rupley, J. Self-association of hen egg-white lysozyme as studied by nuclear magnetic resonance. 1977. *Biochemistry* 16 (17):3879–3882.

Shire, S., Shahrokh, Z., and Liu, J. Challenges in the Development of High Protein Concentration Formulations. 2004. *Journal of Pharmaceutical Sciences* 93(6):1390-1401.



Soda, A., Fujimoto, T., and Nagasawa, M. Johnston-Ogston effect in sedimentation. 1967. *J. Phys. Chem.* 71(13):4274–4281.

Songa, H., and Suh, S. Kunitz-type soybean trypsin inhibitor revisited: refined structure of its complex with porcine trypsin reveals an insight into the interaction between a homologous inhibitor from *Erythrina caffra* and tissue-type plasminogen activator. 1998. *Journal of Molecular Biology* 275(2):347–363.

Special Issue: EMBO Workshop on Biological Implications of Macromolecular Crowding, *Jour. Mol. Rec.* (2003), 17(5) 351-511.

Tanford, Charles. Physical chemistry of macromolecules. New York, New York: Wiley, 1961.

Usha, R., and Ramasami, T. Effect of hydrogen-bond-breaking reagent (urea) on the dimensional stability of rat tail tendon (RTT) collagen fiber. 2002. *Journal of Applied Polymer Science* 84(5):975–982.

Van Beekvelt, M., Colier, W., Wevers, R., and Van Engelen, B. Performance of near-infrared spectroscopy in measuring local O<sub>2</sub> consumption and blood flow in skeletal muscle. 2001. *J Appl Physiol* 90 (2): 511–519.

Van der Berg, B., Ellis, R., and Dobson, C. Effects of macromolecular crowding on protein folding and aggregation. 1999. *Eur. Mol. Bio. Org. Journ.* 18(24): 6927-6933.

Vázquez-Rey, M., and Lang, D. Aggregates in monoclonal antibody manufacturing processes. 2011. *Biotechnology and Bioengineering* 108(7):1494-1508.

Wills, P., and Winzor, D. Studies of solute self-association by sedimentation equilibrium: allowance for effects of thermodynamic non-ideality beyond the consequences of nearest-neighbor interactions. 2001. *Biophys Chem.* 91(3):253-62.

Wolfbeis, O., and Leiner, M. Mapping of the total fluorescence of human blood serum as a new method for its characterization. 1985. *Analytica Chimica Acta* 167: 203–215.

Zangi, R., Zhou, R., and Berne, J. Urea's Action on Hydrophobic Interactions. 2009. *J. AM. CHEM. SOC.* 131:1535–1541.

## APPENDIX A

### DERIVATION OF $M/M_{APP}$

If a plane is imagined inside an analytical ultracentrifugation cell, perpendicular to the radius, the net amount of material  $i$  entering or exiting the plane is equal to the flux,  $J_i$ .

Flux equations take the following form.

$$(1) \quad J_i = \sum_k L_{ik} X_k$$

$X_k$  are forces acting in the direction of  $r$ , and  $L_{ik}$  is a proportionality constant called the phenomenological coefficient. Because  $i$  will diffuse in the opposite direction of the chemical potential gradient in  $i$ ,  $\frac{\partial \mu}{\partial r}$ , the flux due to diffusion is equal to the following, where  $L$  is a phenomenological coefficient to be defined later.

$$(2) \quad J_i = -L \frac{\partial \mu}{\partial r}$$

During an analytical ultracentrifugation experiment there also will be a sedimenting force per mole on  $i$  equal to  $M\omega^2 r$ . This quantity can be added to (1) to arrive at the following equation describing the overall flux.

$$(3) \quad J_i = L'M\omega^2 r - L \frac{\partial \mu}{\partial r}$$

In a purely mechanical system, the only contribution to  $L$  will be friction. If  $F = Ma$  and  $a = \frac{\partial u}{\partial t}$ , where  $u$  is velocity of  $i$ , for sufficiently small magnitudes of  $u$  the frictional force

is proportional to  $u$  via a proportionality constant  $f$  called the frictional coefficient.

Therefore the following is true.

$$(4) \quad M \frac{\partial u}{\partial t} = F - fu$$

The implication of (4) is that as the velocity  $u$  increases so will the friction  $fu$ . This will result in a reduction of  $\frac{\partial u}{\partial t}$  until eventually  $\frac{\partial u}{\partial t}$  will be zero. At such a time (4) reduces to the following.

$$(5) \quad u = F/f$$

If the force in (5) is considered to be the force per particle,  $J_i$  can be expressed in terms of particles/cm<sup>2</sup>s and the flux over time interval  $dt$  is considered to be  $uN$ , where  $N$  is the number of  $i$  per cm<sup>2</sup>, by substituting (5) for  $u$  the following is true.

$$(6) \quad J_i = N_i F / f$$

If the right side of (6) is substituted for  $J$  in (1), it can be seen that  $L$  must be equal to  $N/f$ . If  $J$  is converted to moles/cm<sup>2</sup> and  $F$  to force per mole, this becomes the following, where  $C$  is concentration of  $i$  in moles/cm<sup>3</sup> and  $N$  is Avogadro's number.

$$(7) \quad L = C/Nf$$

If  $L$  is considered to be equal to  $L'$  and the right of (7) is used in place of  $L$  in (3), this results in the following.

$$(8) \quad J = \frac{M\omega^2 r C}{Nf} - \frac{C}{Nf} \frac{\partial \mu}{\partial r}$$

However, it must be taken into account that  $\mu$  is a function of  $r$  due to changes in pressure and concentration over  $r$ . Mathematically, this is expressed by the following.

$$(9) \quad \partial \mu = \left( \frac{\partial \mu}{\partial P} \right)_{T,C} \partial P + \left( \frac{\partial \mu}{\partial C} \right)_{T,P} \partial C$$

$$(10) \quad \frac{\partial \mu}{\partial r} = \left( \frac{\partial \mu}{\partial P} \right)_{T,C} \frac{\partial P}{\partial r} + \left( \frac{\partial \mu}{\partial C} \right)_{T,P} \frac{\partial C}{\partial r}$$

A definition of  $\frac{\partial \mu}{\partial P}$  is easily obtained, where  $\bar{v}$  is the partial specific volume of i.

$$(11) \quad \frac{\partial \mu}{\partial P} = M\bar{v}$$

For ideal solutions  $\partial \mu$  is defined as  $RT \partial \ln X$ , which integrates to  $\mu = \mu^\circ + RT \ln X$ , where

$X$  is the mole fraction of i. For nonideal solutions it is customary to express this as

$\mu = \mu^\circ + RT \ln a$ , where  $a$  is a function of  $X$  such that  $a = \gamma X$ , where  $\gamma$  is called the

activity coefficient. Expressed in moles/L this becomes the following

$$(12) \quad \frac{\partial \mu}{\partial C} = \frac{RT}{C} + RT \frac{\partial \ln \gamma}{\partial C}$$

The change in pressure of the solution when centripetal force  $\omega^2 r$  is applied will be the following, where  $\rho_0$  is the density of the solution.

$$(13) \quad \frac{\partial P}{\partial r} = \rho_0 \omega^2 r$$

By using the right side of (13) for  $\frac{\partial P}{\partial r}$ , (12) for  $\frac{\partial \mu}{\partial C}$ , and (11) for  $\frac{\partial \mu}{\partial P}$ , (10) becomes the

following.

$$(14) \quad \frac{\partial \mu}{\partial r} = M\bar{v}\rho_0\omega^2 r + \frac{RT}{C} \left( 1 + C \frac{\partial \ln \gamma}{\partial C} \right) \left( \frac{\partial C}{\partial r} \right)$$

Substituting (14) for  $\frac{\partial \mu}{\partial r}$  in (8) yields the following.

$$(15) \quad J = \frac{M\omega^2 r C}{N_f} (1 - \bar{v}\rho_0) - \frac{RT}{N_f} \left( 1 + C \frac{\partial \ln \gamma}{\partial C} \right) \left( \frac{\partial C}{\partial r} \right)$$

At equilibrium  $J$  must be zero, therefore  $\frac{M\omega^2 r C}{N_f} (1 - \bar{v}\rho_0) = \frac{RT}{N_f} \left( 1 + C \frac{\partial \ln \gamma}{\partial C} \right) \left( \frac{\partial C}{\partial r} \right)$  which

after algebraic manipulation yields the following

$$(16) \quad \frac{RT}{C} \frac{\partial C}{\partial r} = \frac{M\omega^2 r (1 - \bar{v}\rho_0)}{1 + C(\partial \ln \gamma / \partial C)}$$

The true molar mass must be obtained at infinite dilution, where  $C$  is equal to zero. At such time (16) reduces to the following.

$$(17) \quad M = \frac{RT}{\omega^2 r C (1 - \bar{v} \rho_0)} \frac{\partial C}{\partial r}$$

$M_{app}$  is defined to take into account the deviation from ideality when  $c$  doesn't equal zero, therefore  $M_{app}$  is related to  $M$  in such a way that when (17) is substituted for  $M$  in (16), the result is the following.

$$(18) \quad M_{app} = M / \left( 1 + C \frac{\partial \ln \gamma}{\partial C} \right)$$

APPENDIX B

SEDIMENTATION VELOCITY OF GFP IN HIGH CONCENTRATIONS OF BACKGROUND MOLECULES

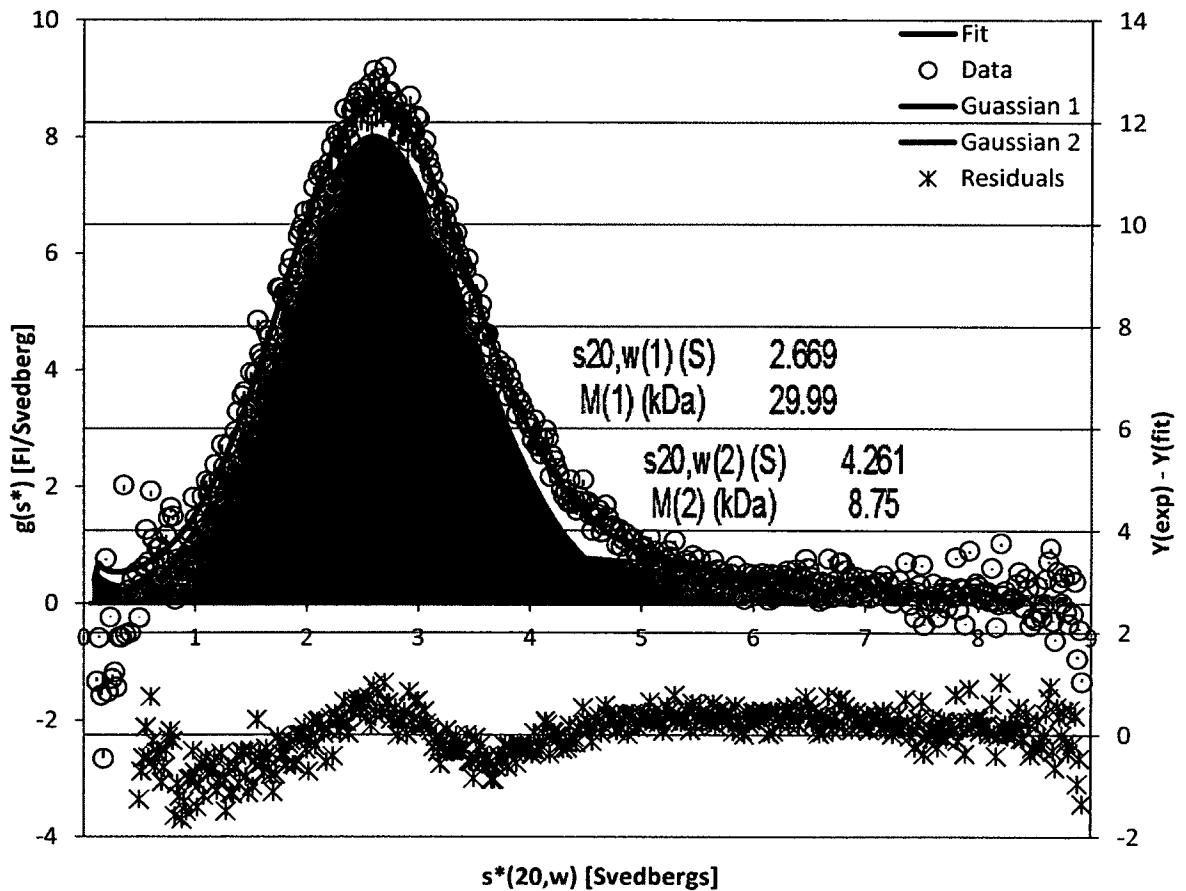


Figure 80. 40 nM GFP in 0.1 g/L dextran. A  $g(s)$  plot from a sedimentation velocity experiment. On the primary axis is plotted the experimental data (Data), and putative plots for all Gaussians, with the area under the curve colored to indicate which portions of the total signal they can account for. Also on the primary axis is the proposed fit to the data. Residuals are plotted on the secondary axis. Data was acquired with the fluorescence detection system.

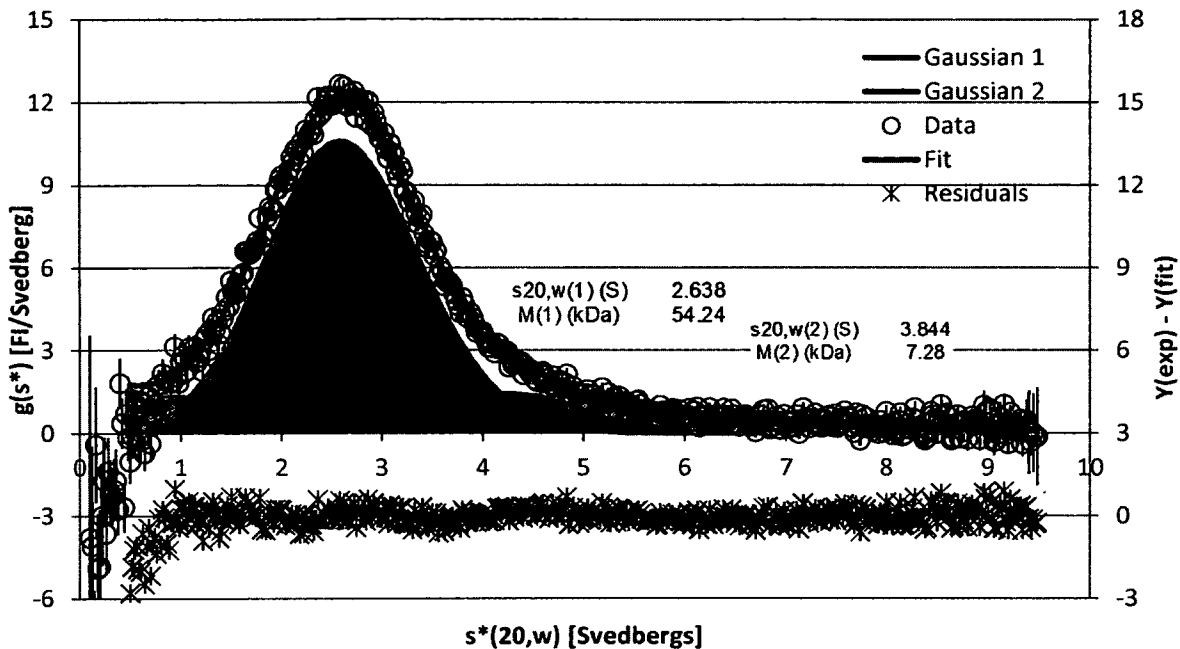


Figure 81. 40 nM GFP in 1 g/L dextran. A  $g(s)$  plot from a sedimentation velocity experiment. On the primary axis is plotted the experimental data (Data), and putative plots for all Gaussians, with the area under the curve colored to indicate which portions of the total signal they can account for. Also on the primary axis is the proposed fit to the data. Residuals are plotted on the secondary axis. Data was acquired with the fluorescence detection system.

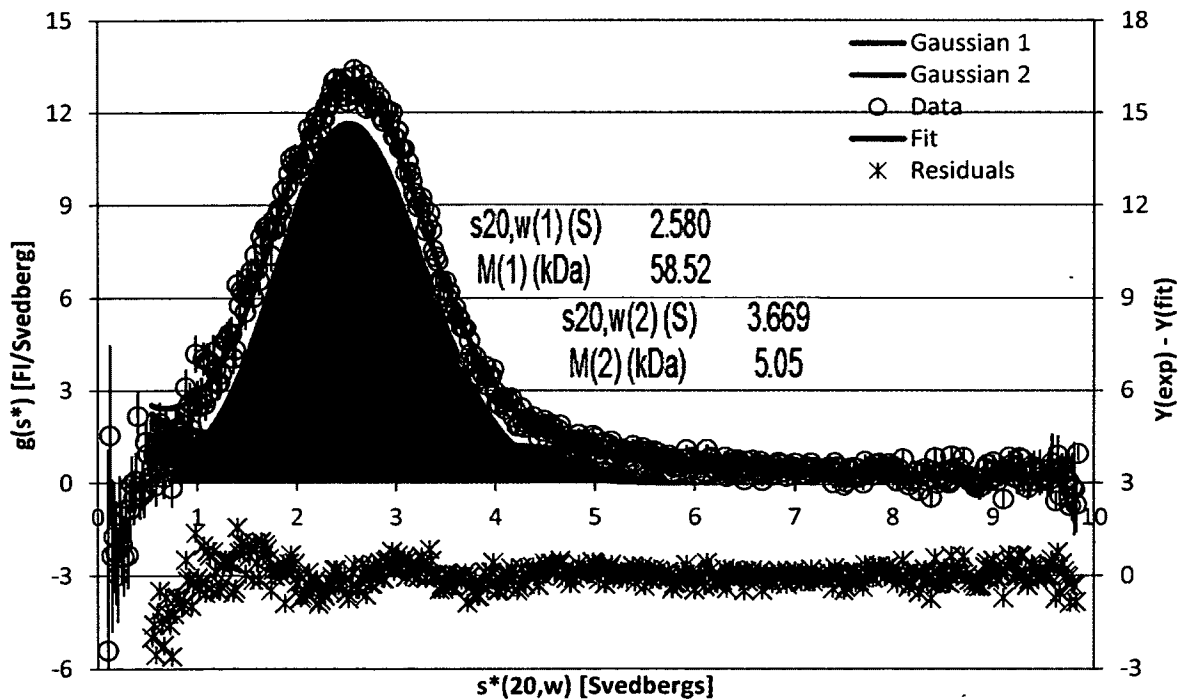


Figure 82. 40 nM GFP in 5 g/L dextran. A  $g(s)$  plot from a sedimentation velocity experiment. On the primary axis is plotted the experimental data (Data), and putative plots for all Gaussians, with the area under the curve colored to indicate which portions of the total signal they can account for. Also on the primary axis is the proposed fit to the data. Residuals are plotted on the secondary axis. Data was acquired with the fluorescence detection system.



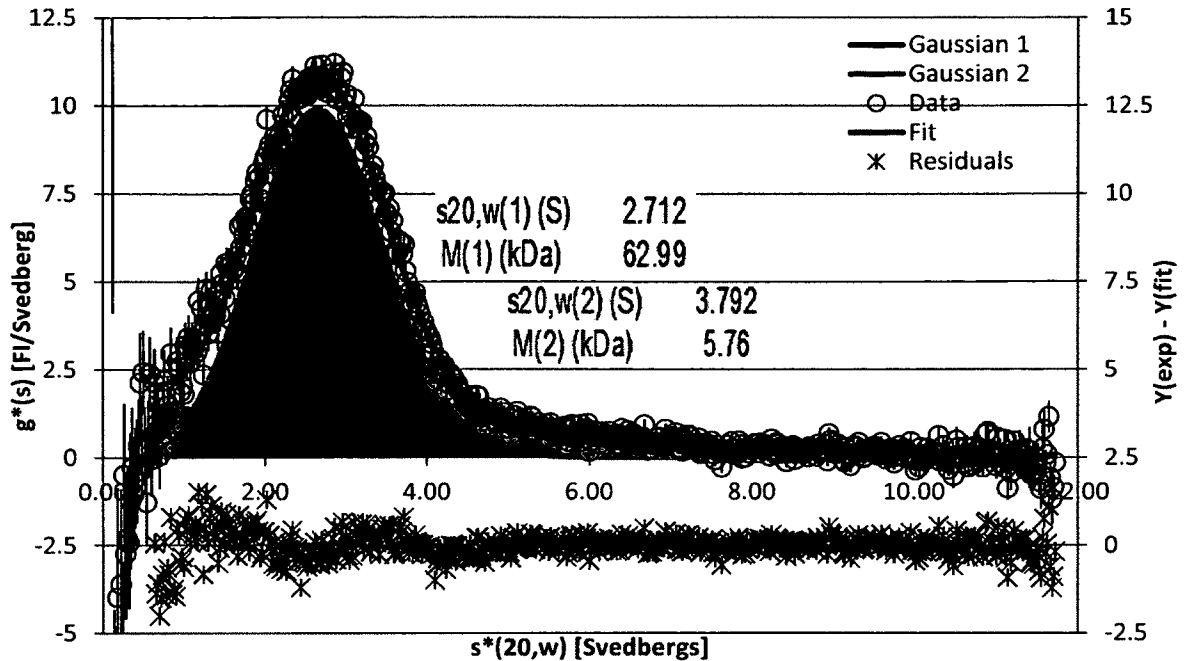


Figure 83. 40 nM GFP in 20 g/L dextran. A  $g(s)$  plot from a sedimentation velocity experiment. On the primary axis is plotted the experimental data (Data), and putative plots for all Gaussians, with the area under the curve colored to indicate which portions of the total signal they can account for. Also on the primary axis is the proposed fit to the data. Residuals are plotted on the secondary axis. Data was acquired with the fluorescence detection system.

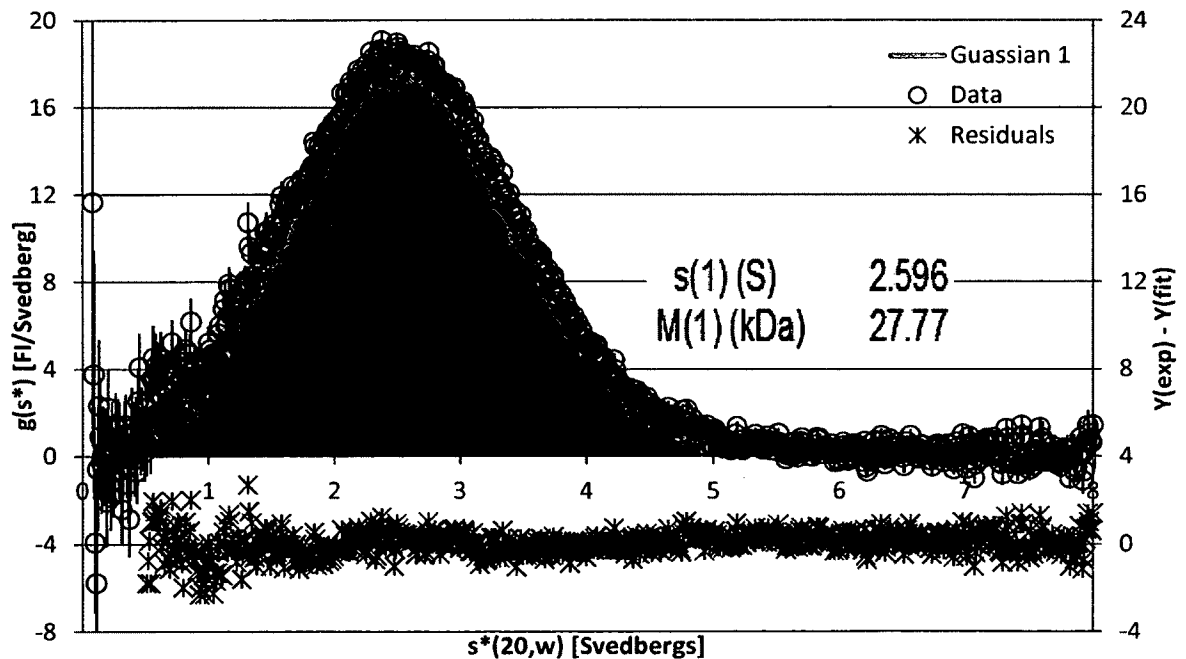


Figure 84. 40 nM GFP in 0.1 g/L HEL. A  $g(s)$  plot from a sedimentation velocity experiment. On the primary axis is plotted the experimental data (Data), and a putative plot for the Gaussian that represents the proposed fit to the data, with the area under the curve colored to indicate which portions of the total signal they can account for. Residuals are plotted on the secondary axis. Data was acquired with the fluorescence detection system.

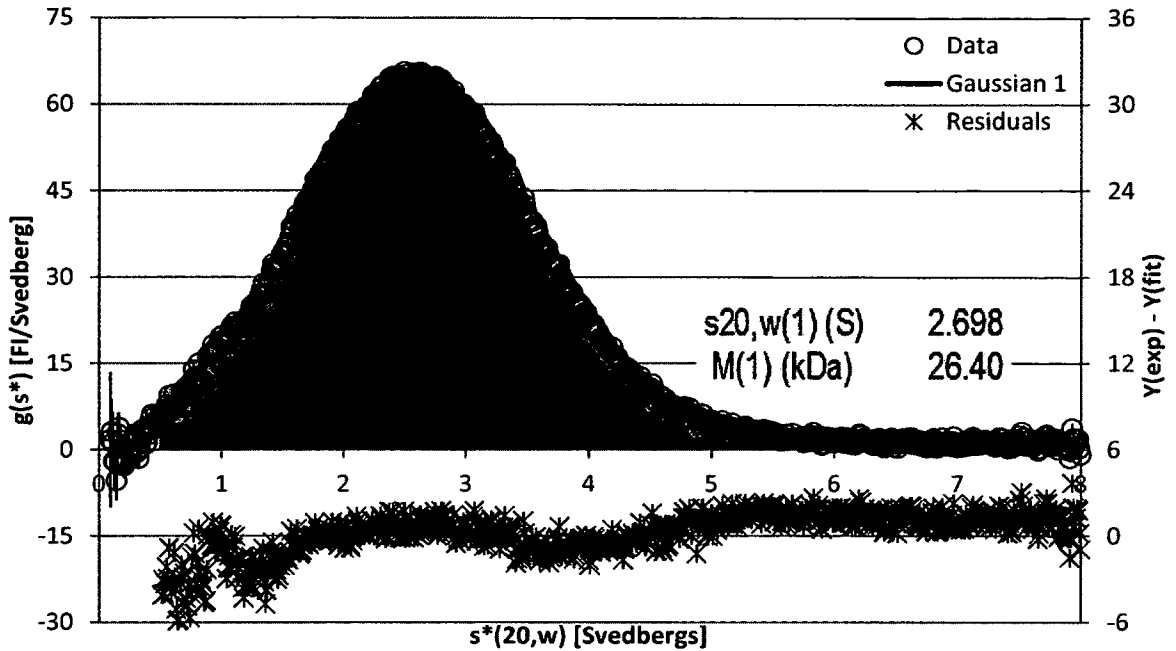


Figure 85. 40 nM GFP in 1 g/L HEL. A  $g(s)$  plot from a sedimentation velocity experiment. On the primary axis is plotted the experimental data (Data), and a putative plot for the Gaussian that represents the proposed fit to the data, with the area under the curve colored to indicate which portions of the total signal they can account for. Residuals are plotted on the secondary axis. Data was acquired with the fluorescence detection system.

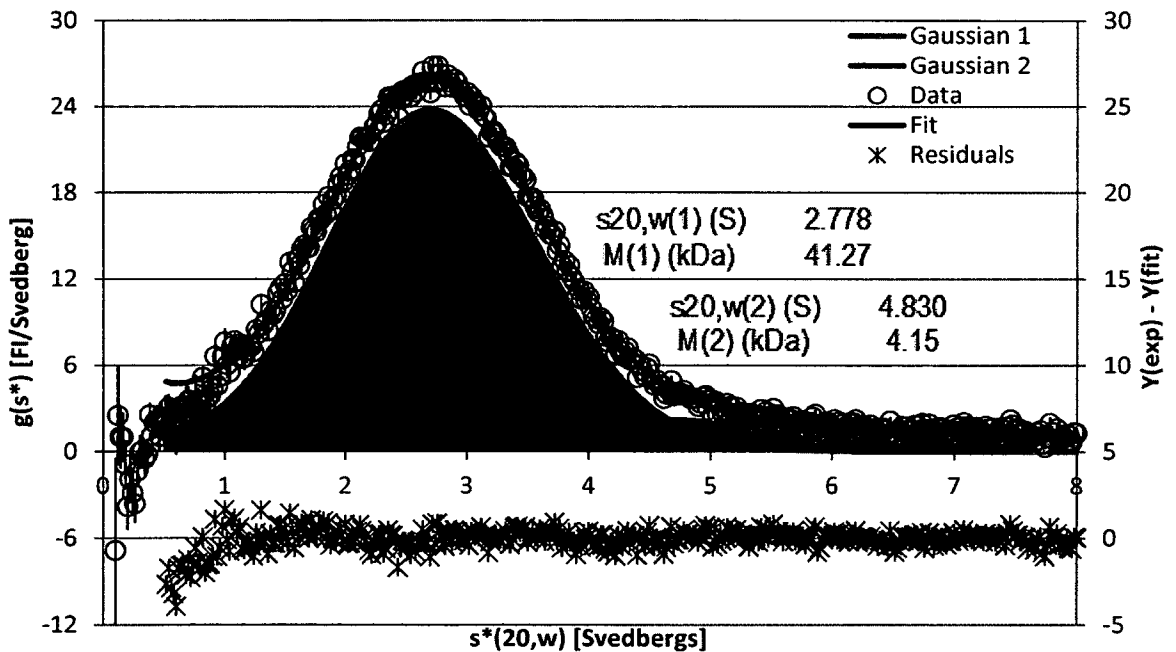


Figure 86. 40 nM GFP in 5 g/L HEL. A  $g(s)$  plot from a sedimentation velocity experiment. On the primary axis is plotted the experimental data (Data), and putative plots for all Gaussians, with the area under the curve colored to indicate which portions of the total signal they can account for. Also on the primary axis is the proposed fit to the data. Residuals are plotted on the secondary axis. Data was acquired with the fluorescence detection system.

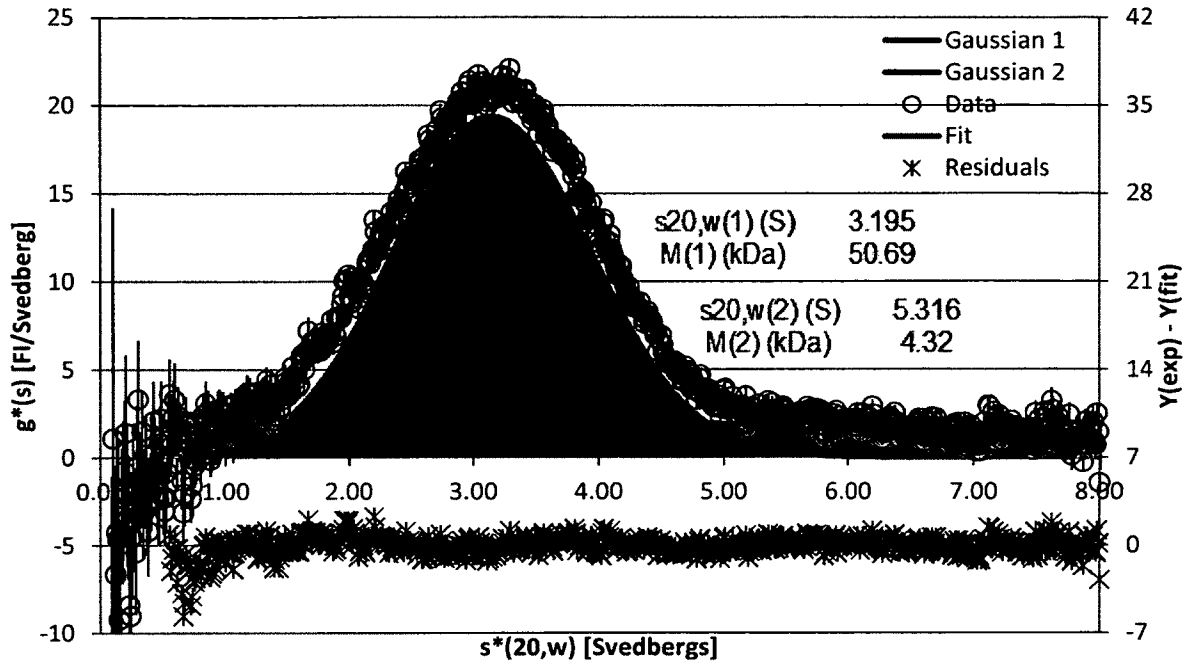


Figure 87. 40 nM GFP in 20 g/L HEL. A  $g(s)$  plot from a sedimentation velocity experiment. On the primary axis is plotted the experimental data (Data), and putative plots for all Gaussians, with the area under the curve colored to indicate which portions of the total signal they can account for. Also on the primary axis is the proposed fit to the data. Residuals are plotted on the secondary axis. Data was acquired with the fluorescence detection system.

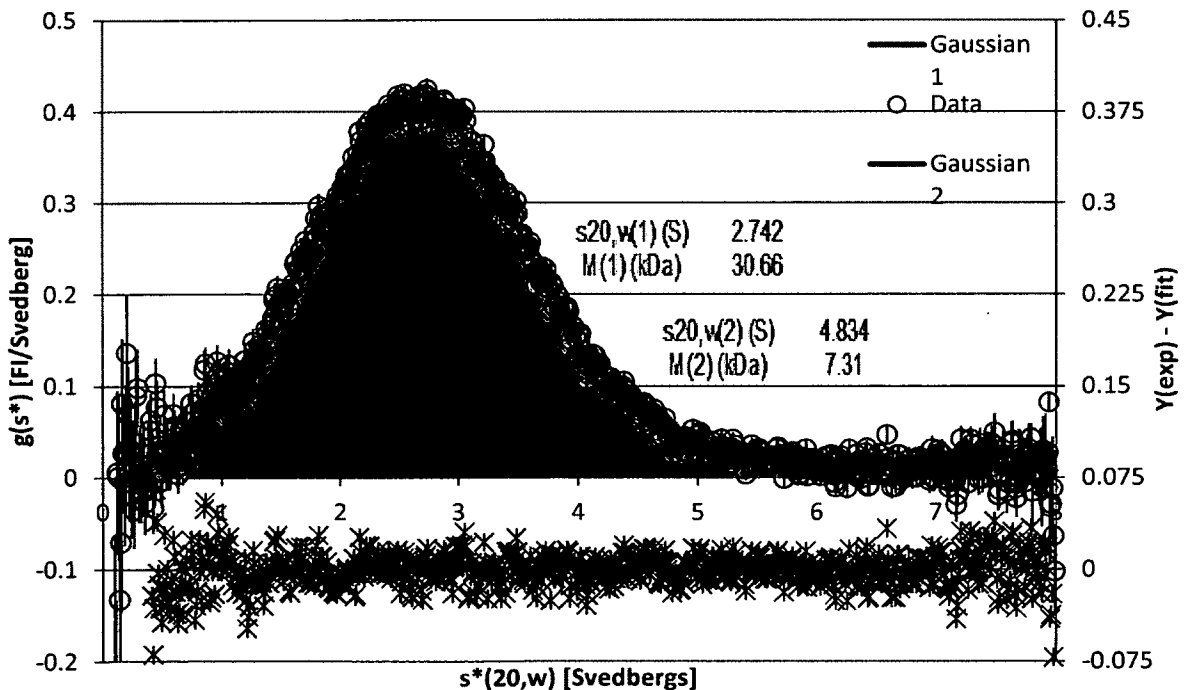


Figure 88. 40 nM GFP in 0.1 g/L STI. A  $g(s)$  plot from a sedimentation velocity experiment. On the primary axis is plotted the experimental data (Data), and putative plots for all Gaussians, with the area under the curve colored to indicate which portions of the total signal they can account for. Also on the primary axis is the proposed fit to the data. Residuals are plotted on the secondary axis. Data was acquired with the fluorescence detection system.

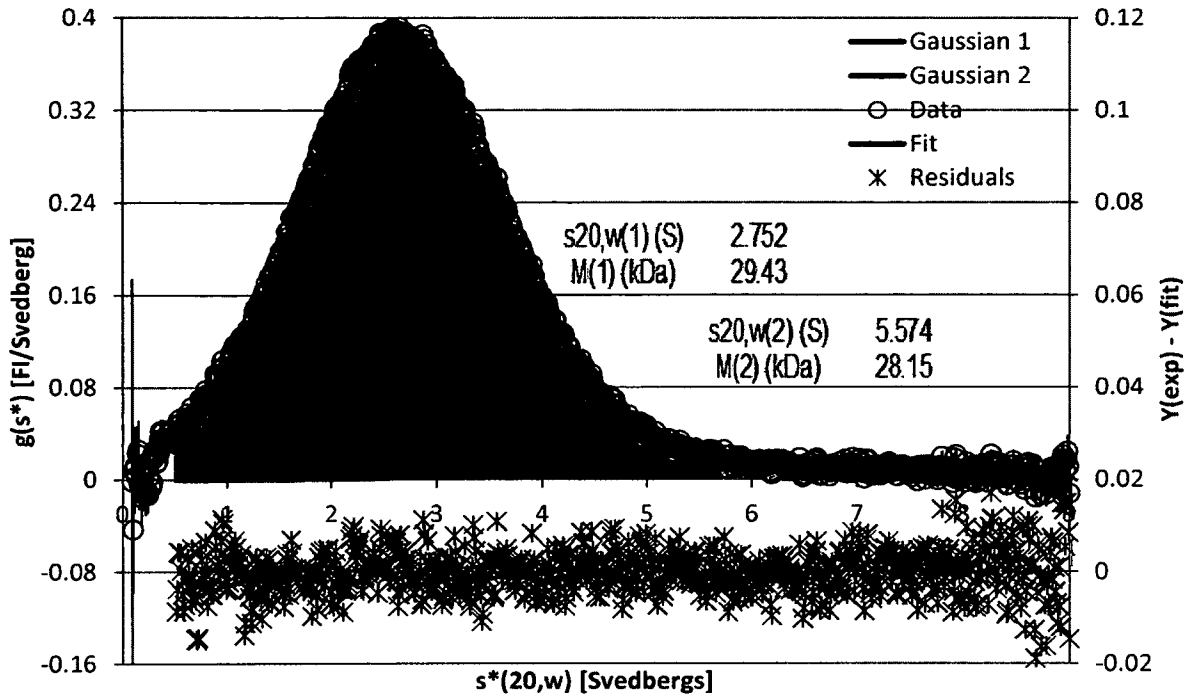


Figure 89. 40 nM GFP in 1 g/L STI. A  $g(s)$  plot from a sedimentation velocity experiment. On the primary axis is plotted the experimental data (Data), and putative plots for all Gaussians, with the area under the curve colored to indicate which portions of the total signal they can account for. Also on the primary axis is the proposed fit to the data. Residuals are plotted on the secondary axis. Data was acquired with the fluorescence detection system.

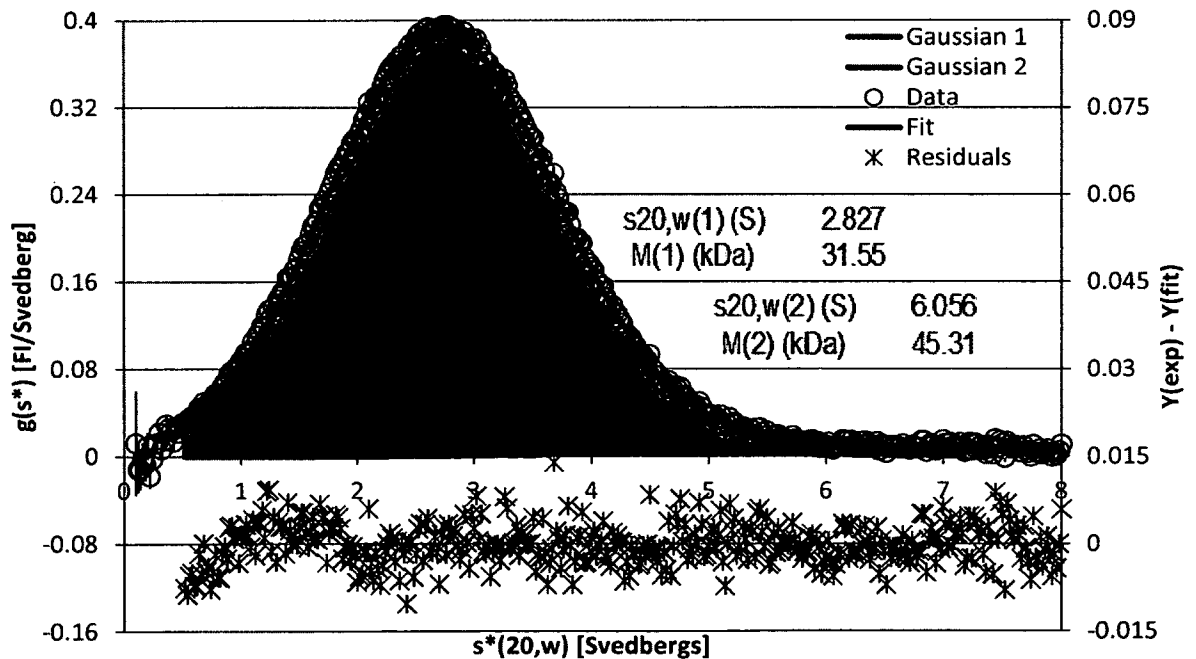


Figure 90. 40 nM GFP in 5 g/L STI. A  $g(s)$  plot from a sedimentation velocity experiment. On the primary axis is plotted the experimental data (Data), and putative plots for all Gaussians, with the area under the curve colored to indicate which portions of the total signal they can account for. Also on the primary axis is the proposed fit to the data. Residuals are plotted on the secondary axis. Data was acquired with the fluorescence detection system.

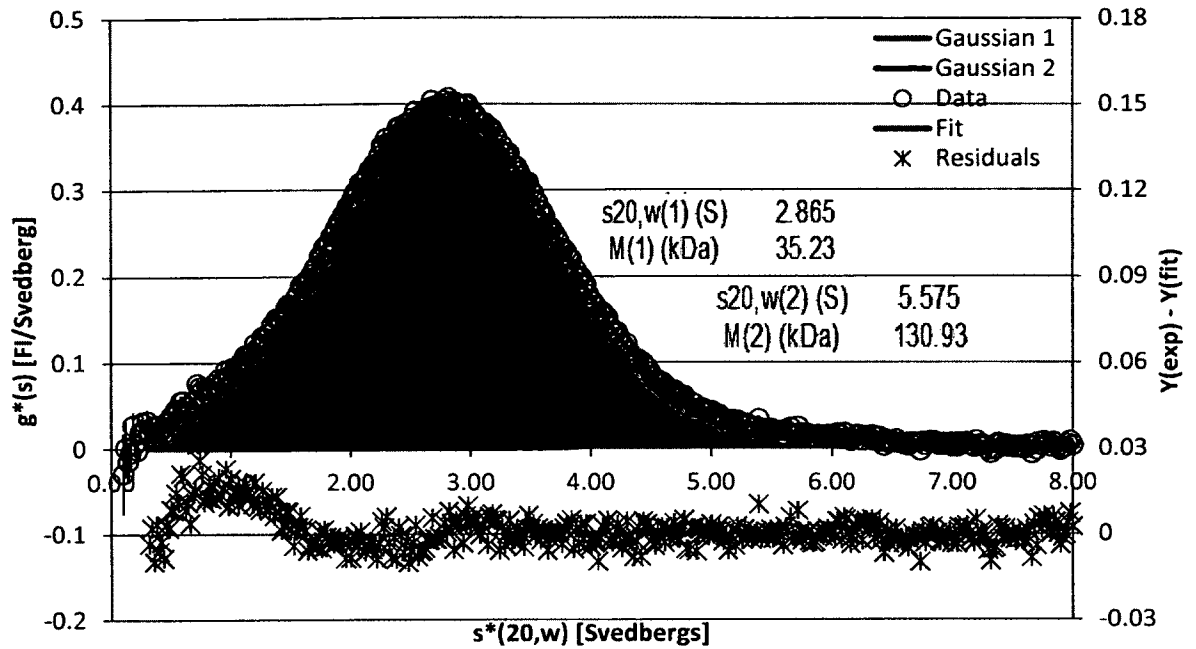


Figure 91. 40 nM GFP in 5 g/L STI. A  $g(s)$  plot from a sedimentation velocity experiment. On the primary axis is plotted the experimental data (Data), and putative plots for all Gaussians, with the area under the curve colored to indicate which portions of the total signal they can account for. Also on the primary axis is the proposed fit to the data. Residuals are plotted on the secondary axis. Data was acquired with the fluorescence detection system.

APPENDIX C

SEDIMENTATION VELOCITY OF GFP AND ANTI-GFP IN HIGH CONCENTRATIONS OF BACKGROUND MOLECULES

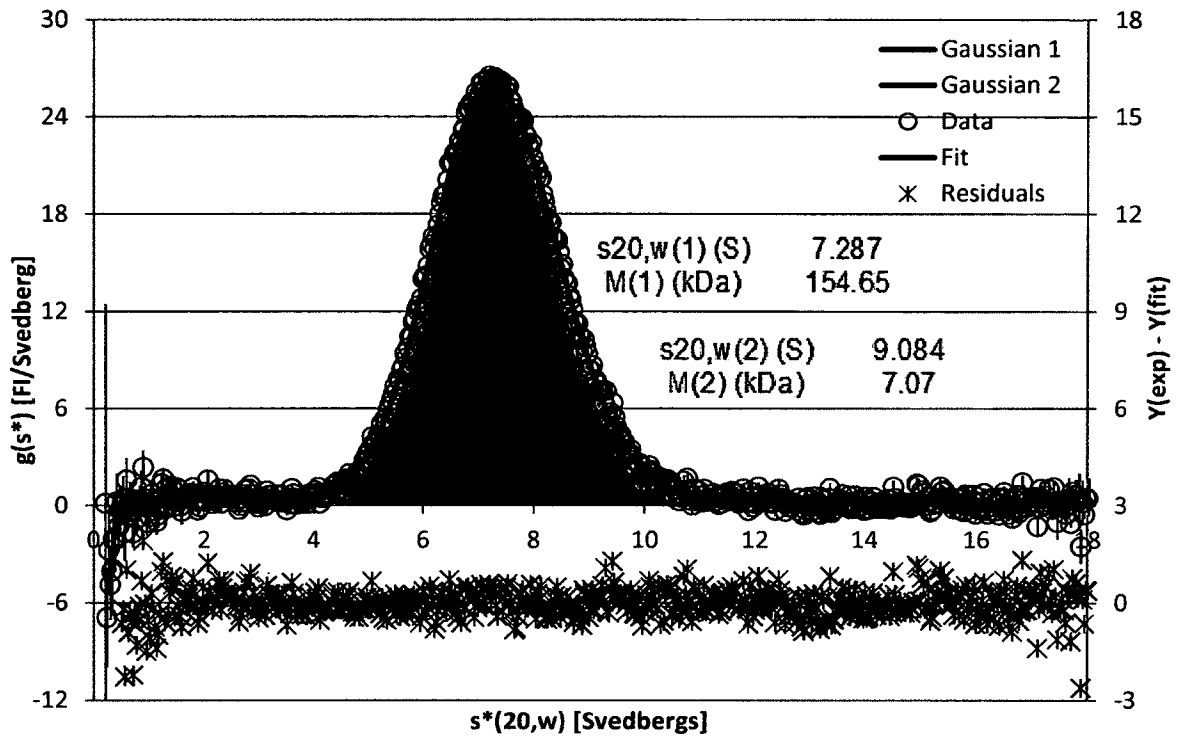


Figure 92. 40 nM GFP, 40 nM anti-GFP in 0.1 g/L HEL. A  $g(s)$  plot from a sedimentation velocity experiment. On the primary axis is plotted the experimental data (Data), and putative plots for all Gaussians, with the area under the curve colored to indicate which portions of the total signal they can account for. Also on the primary axis is the proposed fit to the data. Residuals are plotted on the secondary axis. Data was acquired with the fluorescence detection system.

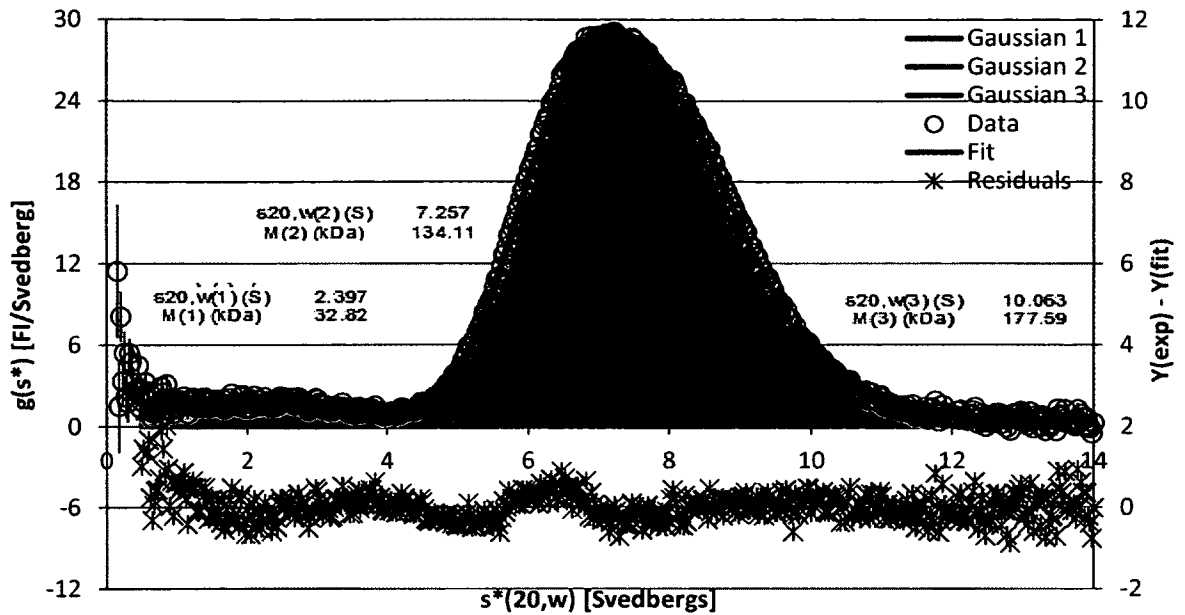


Figure 93. 40 nM GFP, 40 nM anti-GFP in 1 g/L HEL. A  $g(s)$  plot from a sedimentation velocity experiment. On the primary axis is plotted the experimental data (Data), and putative plots for all Gaussians, with the area under the curve colored to indicate which portions of the total signal they can account for. Also on the primary axis is the proposed fit to the data. Residuals are plotted on the secondary axis. Data was acquired with the fluorescence detection system.

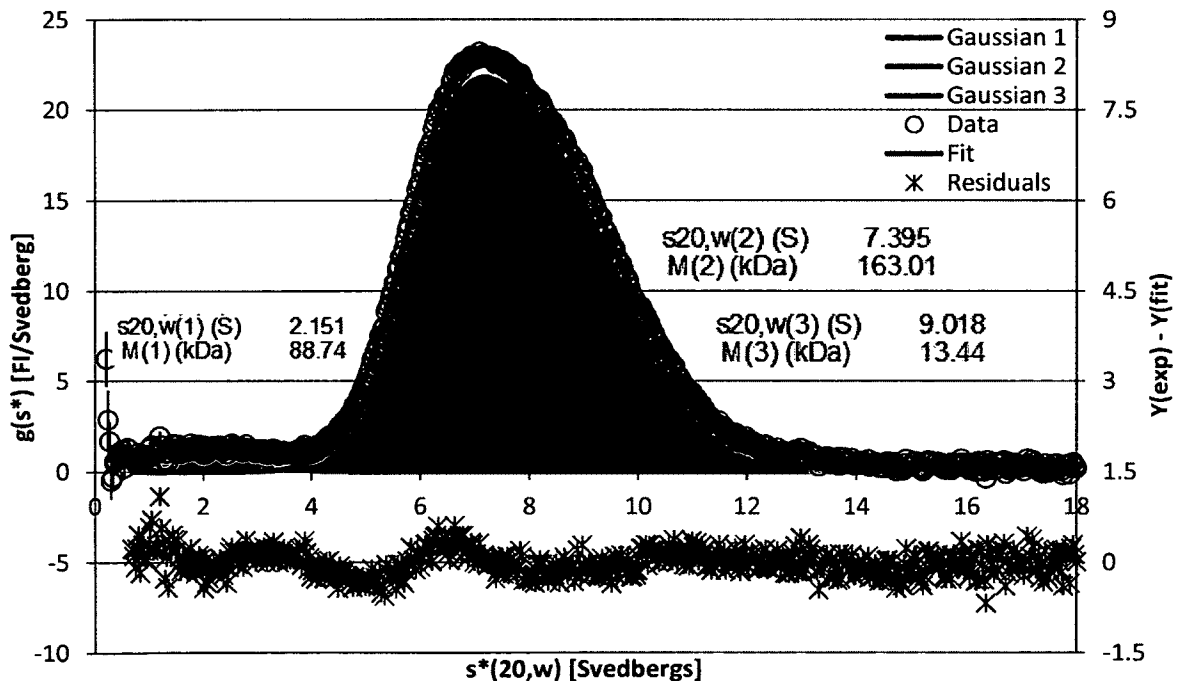


Figure 94. 40 nM GFP, 40 nM anti-GFP in 5 g/L HEL. A  $g(s)$  plot from a sedimentation velocity experiment. On the primary axis is plotted the experimental data (Data), and putative plots for all Gaussians, with the area under the curve colored to indicate which portions of the total signal they can account for. Also on the primary axis is the proposed fit to the data. Residuals are plotted on the secondary axis. Data was acquired with the fluorescence detection system.

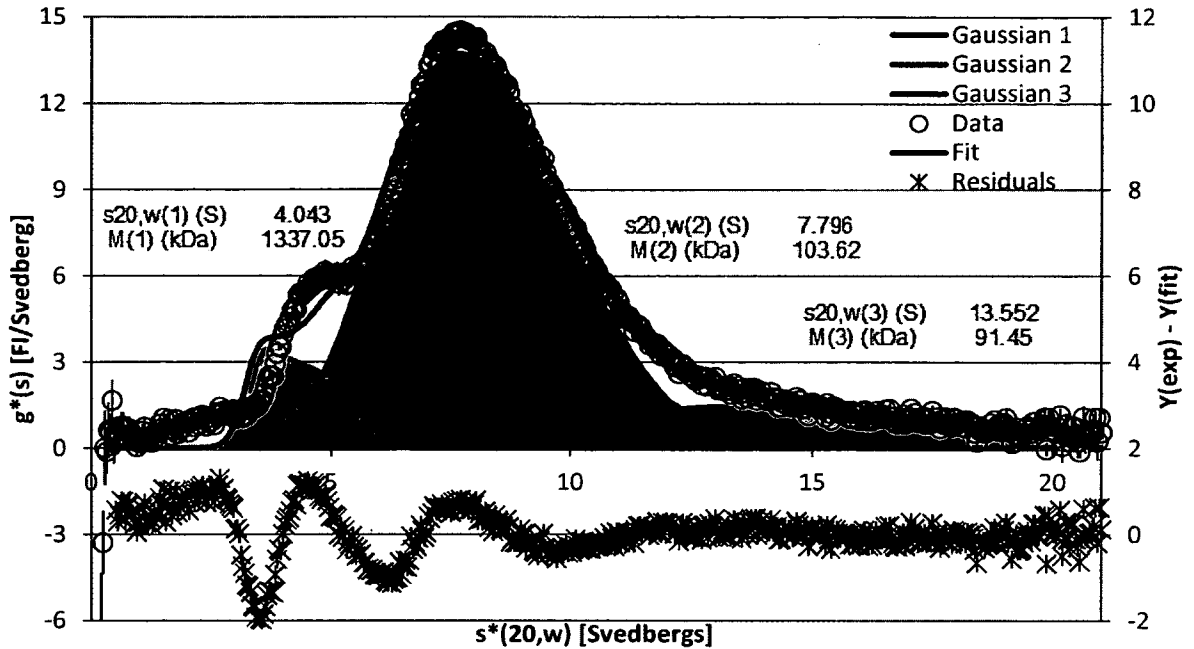


Figure 95. 40 nM GFP, 40 nM anti-GFP in 20 g/L HEL. A  $g(s)$  plot from a sedimentation velocity experiment. On the primary axis is plotted the experimental data (Data), and putative plots for all Gaussians, with the area under the curve colored to indicate which portions of the total signal they can account for. Also on the primary axis is the proposed fit to the data. Residuals are plotted on the secondary axis. Data was acquired with the fluorescence detection system.

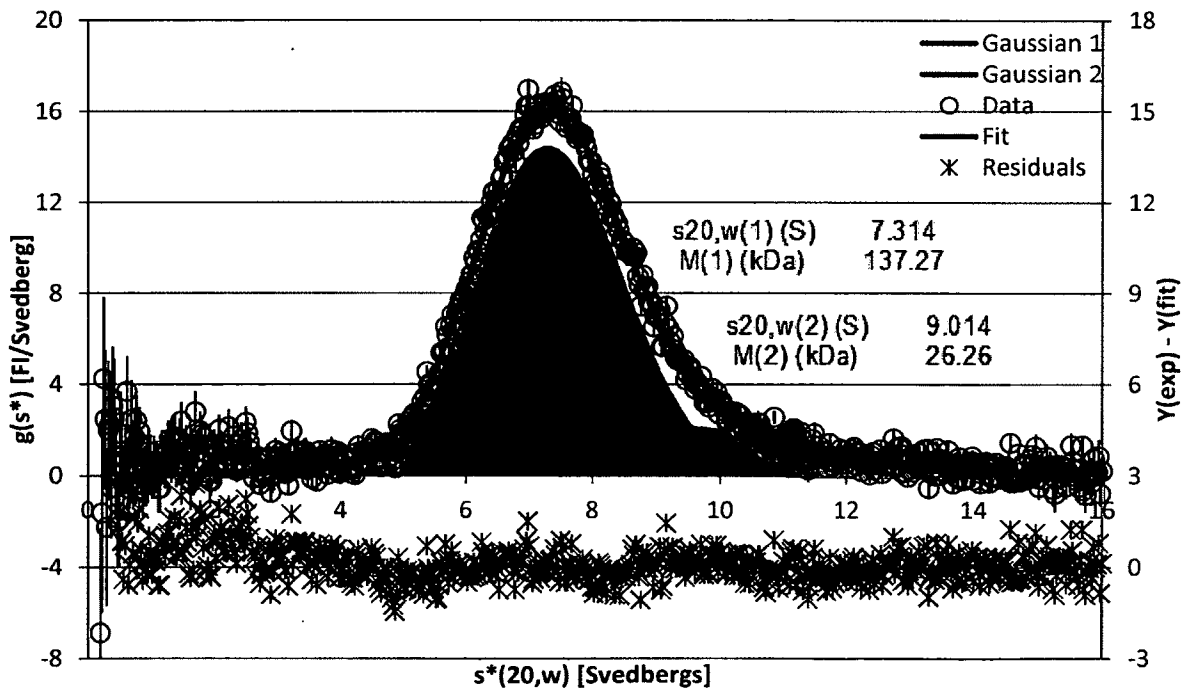


Figure 96. 40 nM GFP, 40 nM anti-GFP in 0.1 g/L dextran. A  $g(s)$  plot from a sedimentation velocity experiment. On the primary axis is plotted the experimental data (Data), and putative plots for all Gaussians, with the area under the curve colored to indicate which portions of the total signal they can account for. Also on the primary axis is the proposed fit to the data. Residuals are plotted on the secondary axis. Data was acquired with the fluorescence detection system.



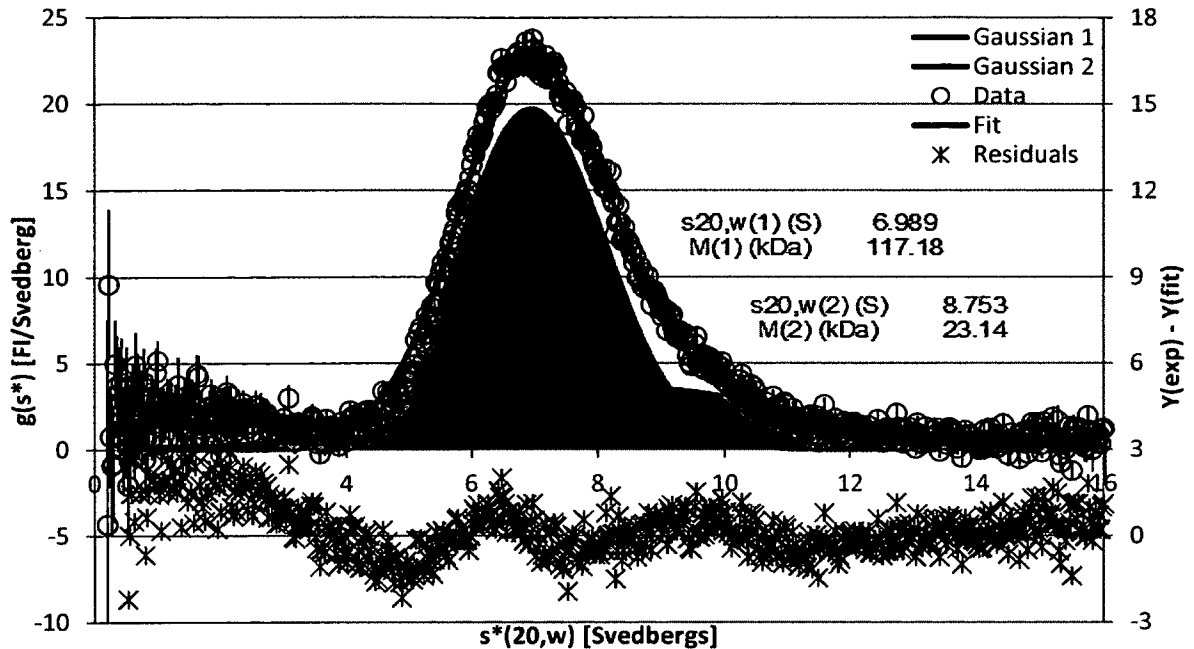


Figure 97. 40 nM GFP, 40 nM anti-GFP in 1 g/L dextran. A  $g(s)$  plot from a sedimentation velocity experiment. On the primary axis is plotted the experimental data (Data), and putative plots for all Gaussians, with the area under the curve colored to indicate which portions of the total signal they can account for. Also on the primary axis is the proposed fit to the data. Residuals are plotted on the secondary axis. Data was acquired with the fluorescence detection system.

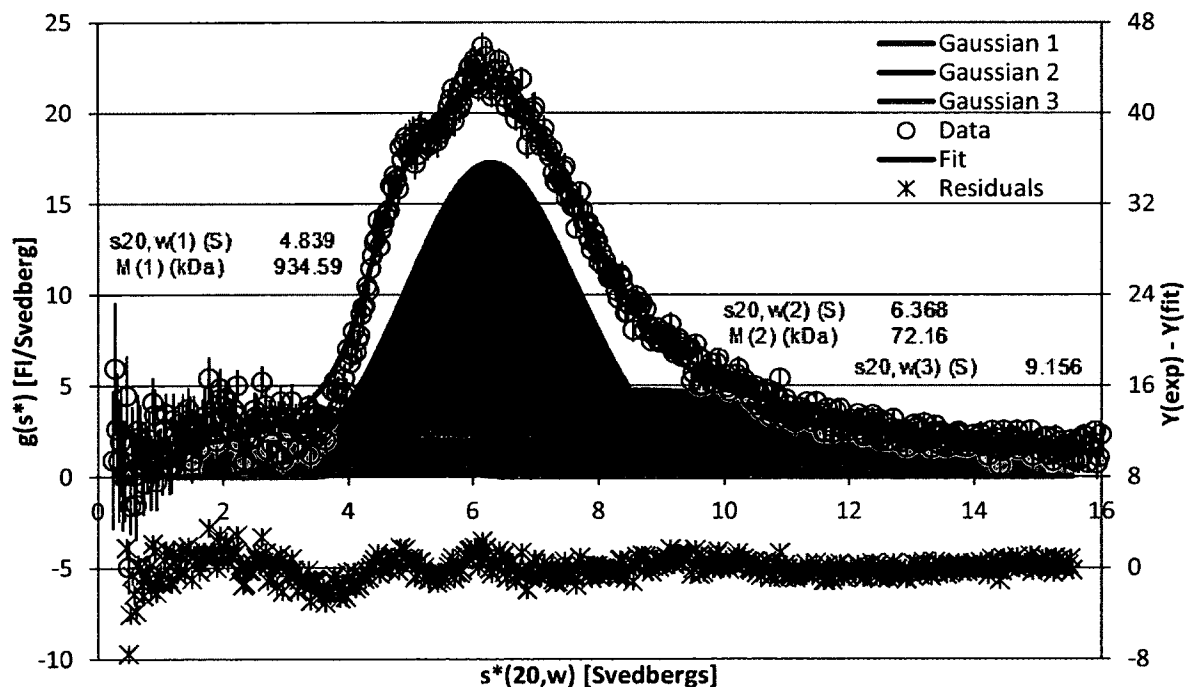


Figure 98. 40 nM GFP, 40 nM anti-GFP in 5 g/L dextran. A  $g(s)$  plot from a sedimentation velocity experiment. On the primary axis is plotted the experimental data (Data), and putative plots for all Gaussians, with the area under the curve colored to indicate which portions of the total signal they can account for. Also on the primary axis is the proposed fit to the data. Residuals are plotted on the secondary axis. Data was acquired with the fluorescence detection system.

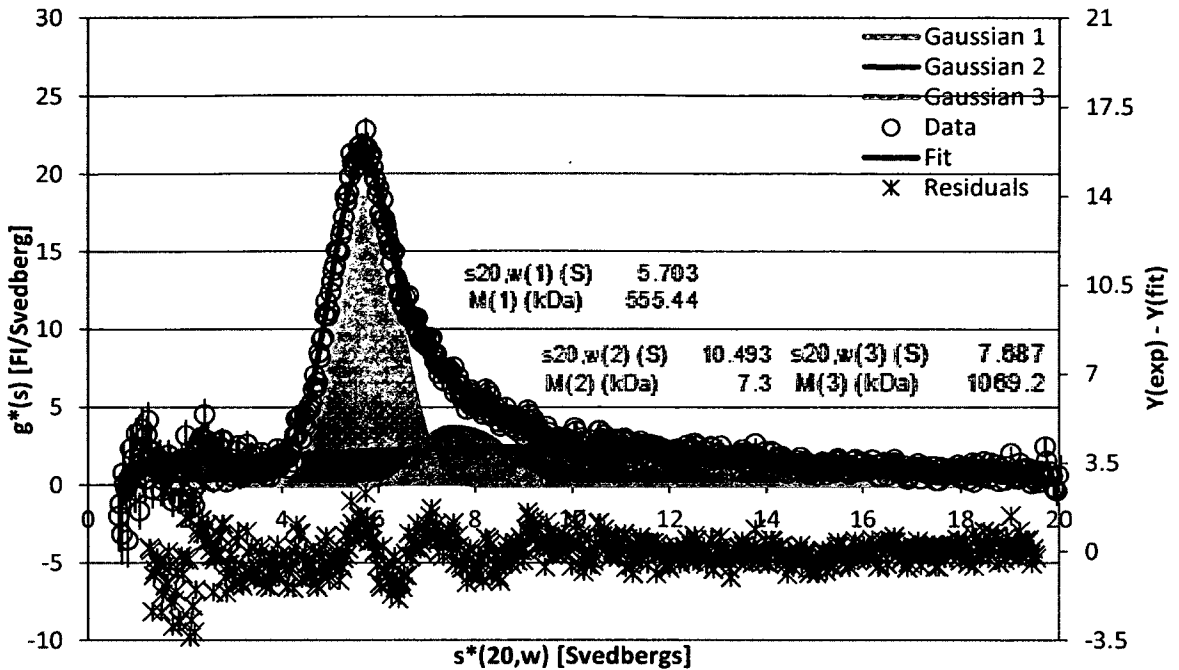


Figure 99. 40 nM GFP, 40 nM anti-GFP in 20 g/L dextran. A  $g(s)$  plot from a sedimentation velocity experiment. On the primary axis is plotted the experimental data (Data), and putative plots for all Gaussians, with the area under the curve colored to indicate which portions of the total signal they can account for. Also on the primary axis is the proposed fit to the data. Residuals are plotted on the secondary axis. Data was acquired with the fluorescence detection system.

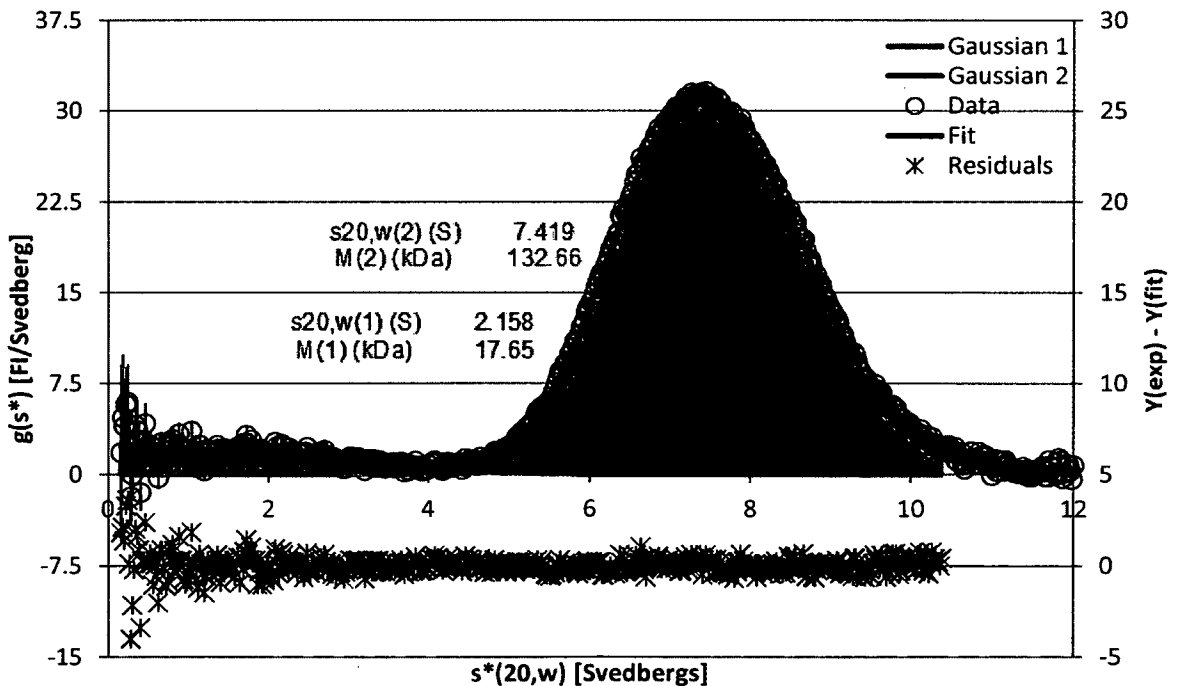


Figure 100. 40 nM GFP, 40 nM anti-GFP in 0.1 g/L STI. A  $g(s)$  plot from a sedimentation velocity experiment. On the primary axis is plotted the experimental data (Data), and putative plots for all Gaussians, with the area under the curve colored to indicate which portions of the total signal they can account for. Also on the primary axis is the proposed fit to the data. Residuals are plotted on the secondary axis. Data was acquired with the fluorescence detection system.

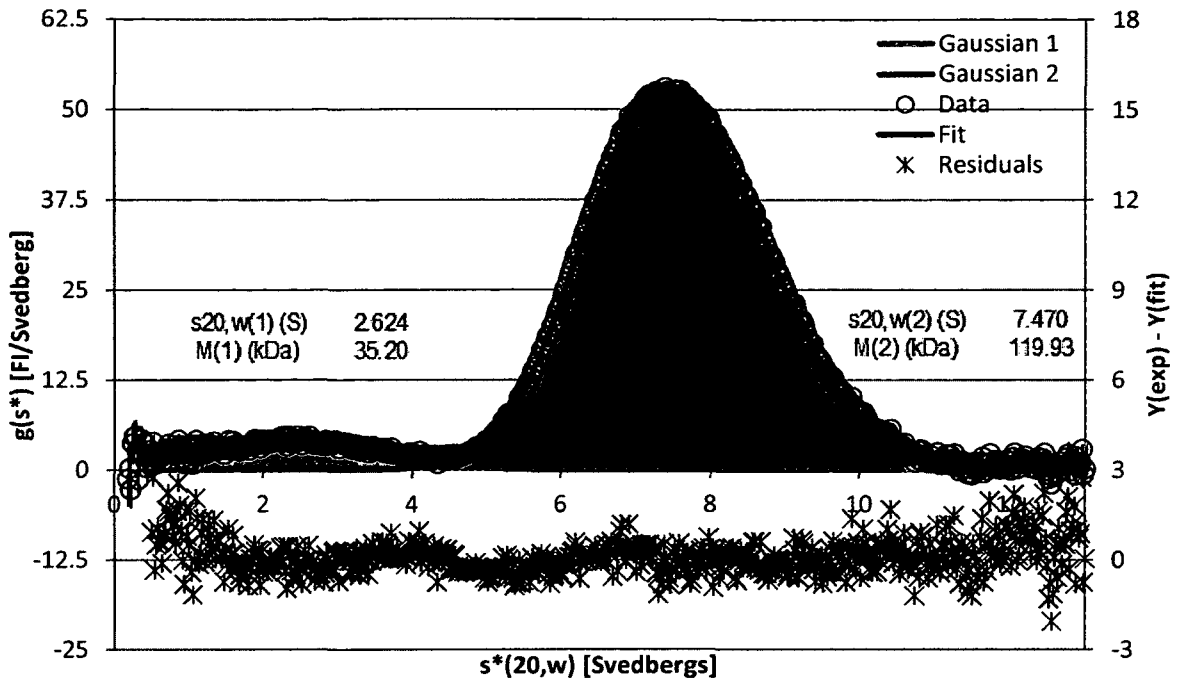


Figure 101. 40 nM GFP, 40 nM anti-GFP in 1 g/L STI. A  $g(s)$  plot from a sedimentation velocity experiment. On the primary axis is plotted the experimental data (Data), and putative plots for all Gaussians, with the area under the curve colored to indicate which portions of the total signal they can account for. Also on the primary axis is the proposed fit to the data. Residuals are plotted on the secondary axis. Data was acquired with the fluorescence detection system.

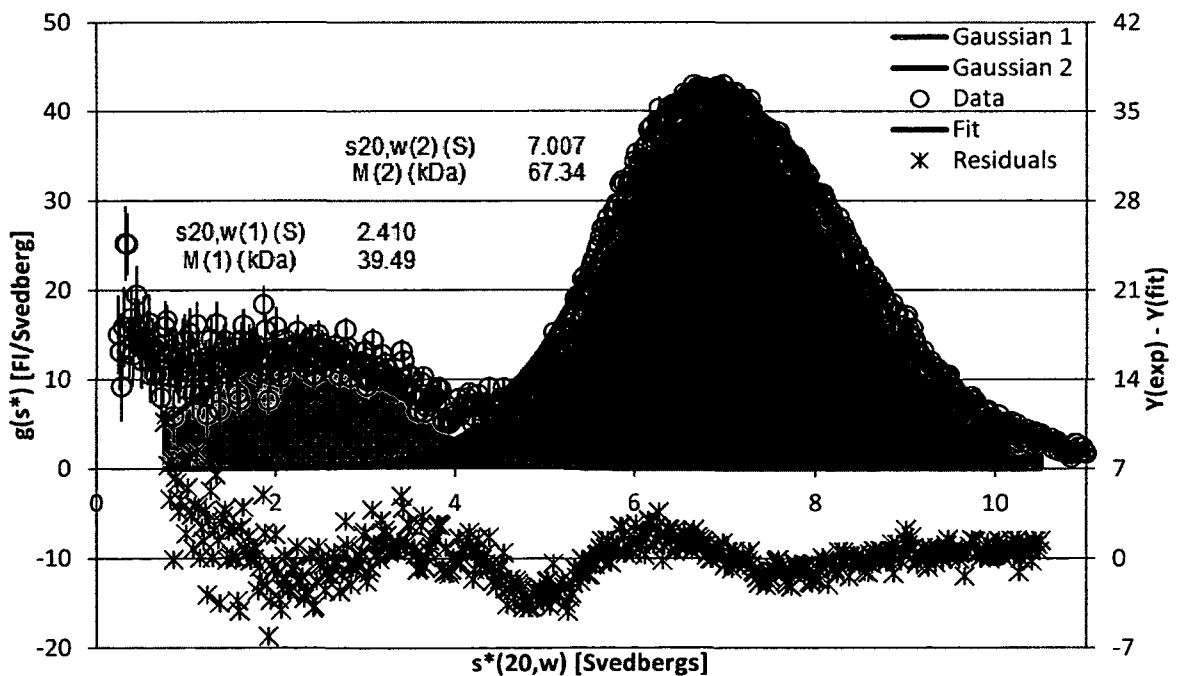


Figure 102. 40 nM GFP, 40 nM anti-GFP in 5 g/L STI. A  $g(s)$  plot from a sedimentation velocity experiment. On the primary axis is plotted the experimental data (Data), and putative plots for all Gaussians, with the area under the curve colored to indicate which portions of the total signal they can account for. Also on the primary axis is the proposed fit to the data. Residuals are plotted on the secondary axis. Data was acquired with the fluorescence detection system.

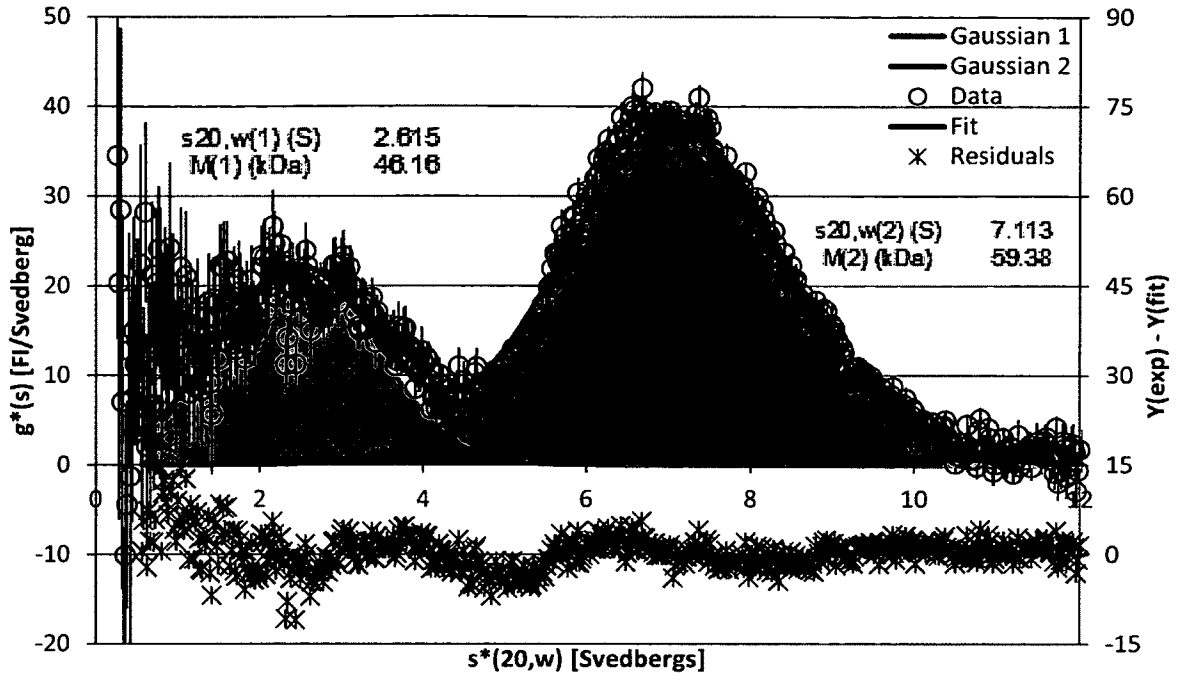


Figure 103. 40 nM GFP, 40 nM anti-GFP in 20 g/L STI. A  $g(s)$  plot from a sedimentation velocity experiment. On the primary axis is plotted the experimental data (Data), and putative plots for all Gaussians, with the area under the curve colored to indicate which portions of the total signal they can account for. Also on the primary axis is the proposed fit to the data. Residuals are plotted on the secondary axis. Data was acquired with the fluorescence detection system.

APPENDIX D

SEDIMENTATION VELOCITY OF FIFTY PERCENT SERUM

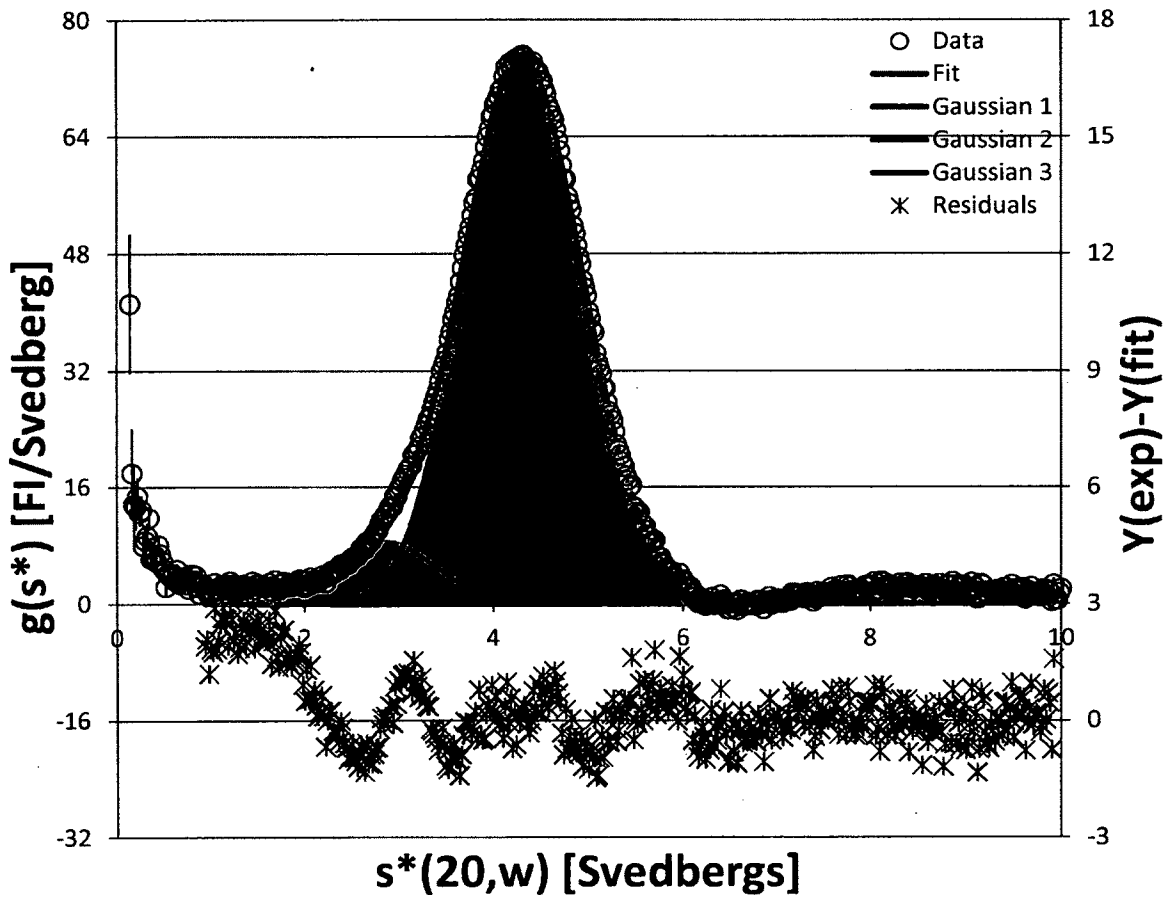


Figure 104. **Autofluorescence of 50% serum.** A  $g(s)$  plot from a sedimentation velocity experiment. On the primary axis is plotted the experimental data (Data), and putative plots for all Gaussians, with the area under the curve colored to indicate which portions of the total signal they can account for. Also on the primary axis is the proposed fit to the data. Residuals are plotted on the secondary axis. Data was acquired with the fluorescence detection system.